UCLA
UCLA Electronic Theses and Dissertations

Title

Novel Approaches for the Application of Mitochondrial Respirometry in Human Studies

Permalink

https://escholarship.org/uc/item/3x00m0xd

Author

Osto, Corey Afsheen

Publication Date

2024

Supplemental Material

https://escholarship.org/uc/item/3x00m0xd#supplemental

Peer reviewed|Thesis/dissertation

eScholarship.org Powered by the California Digital Library
University of California

UNIVERSITY OF CALIFORNIA

Los Angeles

Novel Approaches for the Application of Mitochondrial Respirometry in Human Studies

A dissertation submitted in partial satisfaction of the requirements for the degree Doctor of Philosophy in Molecular and Medical Pharmacology

by

Corey Afsheen Osto

2024

© Copyright by

Corey Afsheen Osto

2024

ABSTRACT OF THE DISSERTATION

Novel Approaches for the Application of Mitochondrial Respirometry in Human Studies

by

Corey Afsheen Osto

Doctor of Philosophy in Molecular and Medical Pharmacology

University of California, Los Angeles, 2024

Professor Orian Shirihai, Co-Chair

Professor Linsey Stiles, Co-Chair

Though mitochondrial research has become more prominent in the last forty years, most methodologies to study mitochondria have been focused on cell and animal models. Respirometry, the assessment of mitochondrial function measured as oxygen consumption by Complex IV of the electron transport chain, is the “gold standard” for mitochondrial assessment, yet it is rarely utilized in human samples. This is due to two fundamental methodological challenges: (1) samples for respirometry must be processed and ran within hours of acquisition on specialized and complex equipment, and (2) human sampling for respirometry must be acquired using invasive tissue biopsies. While we as a field realize the importance of oxygen consumption as a measurement of mitochondrial function, the current methodologies are now limiting the types of biological and clinical questions we can ask and answer. Addressing the first challenge preventing widespread adoption of respirometry, the recently developed RIFS (Respirometry In previously-Frozen Specimen) assay allows for the measurement of maximal

respiratory capacity from cells or tissues which have been previously frozen. This allows samples to be processed and then stored or biobanked for later respirometry assessment, ultimately making respirometry methodologies significantly easier, cheaper, and more accessible. To the second challenge though, there has been minimal breakthrough.

In this thesis we will cover novel methodologies overcoming challenges which are paramount to the expansion of respirometry methodologies for clinical applications. We will discuss the RIFS protocol in detail, describe the methodologies developed to perform a first-of-its-kind high-throughput and high-resolution respirometry study of the human brain, and will detail the development of a technique to measure mitochondrial respiration in cells human salivary leukocytes. Together, these chapters present novel methodologies designed to overcome the primary limitations of performing respirometry in human studies.

The dissertation of Corey Afsheen Osto is approved.

Marc Liesa Roig

Ajit S. Divakaruni

Jennifer M. Murphy

Orian Shirihai, Committee Co-Chair

Linsey Stiles, Committee Co-Chair

University of California, Los Angeles

2024

DEDICATION

This dissertation is dedicated to the many family members who have gotten me to this day and have been such a major part of who I am. Thank you to my father Michael for his support, love, and guidance to get me as far in life as he knew how. Thank you to my cousins Megan, Matthew, Chelsea, Brendan, and Emily for being the best siblings I could ever ask for. Thank you to my Amoos and Aunties Patti, Payman, Bobby, and Sara and my partner Pagé's parents Graham and Audrey for their love, support, generosity, and sometimes parenting, especially during graduate school. Thank you to my grandmother Moman for her endless love and for the enormous amount of Persian food which sustained me throughout the PhD process. Thank you to my grandfather Ali who passed during graduate school but would have been immensely proud of my accomplishments. Finally, thank you to my incredible partner Pagé for her endless love, understanding, and support as we went through the trials and tribulations of graduate school together; there is no one else I would have rather had at my side through this journey.

TABLE OF CONTENTS

ABSTRACT OF THE DISSERTATION ii

DEDICATION v

TABLE OF CONTENTS vi

ACKNOWLEDGEMENTS ix

CURRICULUM VITAE xi

INTRODUCTION 1

Assessing Mitochondrial Function in Humans 1

Respirometry is the Gold Standard for Measuring Mitochondrial Function 1

The Respirometry in Previously-Frozen Specimen (RIFS) Assay Overcomes the Necessity of Immediate Sample Processing for Respirometry 2

Assessing Respirometry Non-invasively for Human Samples 3

Overcoming the Hurdles to Respirometry in Human Samples 4

Chapter 1: Measuring Mitochondrial Respiration in Previously Frozen Biological Samples 6

Introduction 6

BASIC PROTOCOL 1: Sample Collection, Storage, And Homogenization For Previously Frozen Tissue Respirometry 8

BASIC PROTOCOL 2: Running A Seahorse Respirometry Assay Using Previously Frozen Tissue Samples 11

BASIC PROTOCOL 3: Normalization To Mitochondrial Content For Previously Frozen Tissue Respirometry (Optional) 14

Commentary 17

Troubleshooting....19

Statistical Analysis 19

Understanding Results....20

Time Considerations....21

Figures 22

Tables....29

Chapter 2: A Human Brain Map of Mitochondrial Respiratory Capacity and Diversity....33

Introduction 33

Main....34

Discussion 46

Methods 48

Figures 63

Tables....87

Chapter 3: Performing and Analyzing Large-scale Studies of Seahorse Respirometry Data 88

Introduction 88

Main....89

Technical Considerations: 93

Analytical Considerations: 97

Discussion:....103

Figures 105

Sample Data and Automated Spreadsheets and Calculation Sheets 110

Chapter 4: Salivary Cells as a Non-invasive Biomarker to Assess Mitochondrial Respirometry in Human Subjects 111

Introduction 111

Main 113

Discussion 122

Figures 125

Methods 138

CONCLUSION 144

BIBLIOGRAPHY 147

ACKNOWLEDGEMENTS

I would like to thank my mentors Orian Shirihai and Linsey Stiles for their guidance, support, and the immense amount of time and effort they have put into my development as a scientist. As a dynamic duo they have guided me through the many difficulties of science and life with such kindness and belief in me and my abilities. I am so thankful to have worked so closely with both of them and I know that my growth during graduate school could not have been done without their support.

I would like to thank the rest of my graduate thesis committee. Thank you to Marc Liesa for his immense knowledge and his dedication and care for me and my work even after moving to Spain. Thank you to Jennifer Murphy, it has been such a pleasure having you on my committee and I have appreciated your input as someone outside of the mitochondrial space. Finally, thank you to Ajit Divakaruni for your valuable insights into the world of mitochondrial bioenergetics, I have really appreciated your detailed and inquisitive critiques and questions and have grown significantly as a scientist as a result.

I would like to thank all of the members of the Shirihai/Stiles Lab for their support, feedback, collaborations, friendships, and sometimes saliva provided during my time in graduate school. I would especially like to thank Jenny Ngo and Anton Petcherski for their amazing mentorship and friendship throughout grad school. I am so appreciative of everyone in the lab and I know that I could not have made it through this process without them.

Works which are Published or In Preparation for Publication which have Been Included in this Thesis:

Chapter 1 of this thesis is a version of: Osto, C., Benador, I. Y., Ngo, J., Liesa, M., Stiles, L., Acin-Perez, R., & Shirihai, O. (2020). Measuring mitochondrial respiration in previously frozen biological samples. *Current Protocols in Cell Biology*, 89, e116. doi: 10.1002/cpcb.116

Chapter 2 of this thesis is a version of: Mosharov, Eugene V., Ayelet M. Rosenberg, Anna S. Monzel, Corey A. Osto, Linsey Stiles, Gorazd B. Rosoklija, Andrew J. Dwork, Snehal Bindra, Ya Zhang, Masashi Fujita, Madeline B. Mariani, Mihran Bakalian, David Sulzer, Philip L. De Jager, Vilas Menon, Orian S. Shirihai, J. John Mann, Mark Underwood, Maura Boldrini, Michel Thiebaut de Schotten, Martin Picard (2024). "A Human Brain Map of Mitochondrial Respiratory Capacity and Diversity." bioRxiv. https://doi.org/10.1101/2024.03.05.583623. This work is currently in preprint, preparing for publication.

Chapter 3 of this thesis is a version of: Osto, Corey A., Mosharov, Eugene V., Picard, Martin, Stiles, Linsey, Orian S. Shirihai (2024). "Performing and Analyzing Large-Scale Studies of Seahorse Respirometry Data." This work is in preparation for publication.

Chapter 4 of this thesis is a version of: Osto, Corey A., Acin-Perez, Rebeca, Ngo, Jennifer, Petcherski, Anton, Dham, Surya, Eastes, Andrea, Hablewitz, Jeffrey, Stiles, Linsey, Shirihai, Orian (2024). Saliva as a Non-invasive Biomarker to Assess Mitochondrial Respirometry in Human Subjects. This work is in preparation for publication.

CURRICULUM VITAE

Education and Training

B.S. in Biochemistry – University of California- Los Angeles- (June 2015).

Publications:

In progress: Osto, Corey A., Acin-Perez, Rebeca, Ngo, Jennifer, Petcherski, Anton, Dham, Surya, Eastes, Andrea, Hablewitz, Jeffrey, Stiles, Linsey, Shirihai, Orian (2024). Saliva as a Non-invasive Biomarker to Assess Mitochondrial Respirometry in Human Subjects.

In progress: Osto, Corey A., Dham, Surya, Acin-Perez, Rebeca, Petcherski, Anton, Ngo, Jennifer, Stiles, Shirihai, Orian (2024). Protocol for the Isolation of Human Salivary Leukocytes for Downstream Respirometry Applications.

In progress: Osto, Corey A., Mosharov, Eugene V., Picard, Martin, Stiles, Linsey, Orian S. Shirihai (2024). "Performing and Analyzing Large-Scale Studies of Seahorse Respirometry Data."

Mosharov, Eugene V., Ayelet M. Rosenberg, Anna S. Monzel, **Corey A. Osto**, Linsey Stiles, Gorazd B. Rosoklija, Andrew J. Dwork, et al. (2024). "A Human Brain Map of Mitochondrial Respiratory Capacity and Diversity." bioRxiv. https://doi.org/10.1101/2024.03.05.583623.

Osto, C., Benador, I. Y., Ngo, J., Liesa, M., Stiles, L., Acin-Perez, R., & Shirihai, O. (2020). Measuring mitochondrial respiration in previously frozen biological samples. Current Protocols in Cell Biology, 89, e116. doi: 10.1002/cpcb.116

Ngo, J., **Osto, C**., Villalobos, F., & Shirihai, O. S. (2021). "Mitochondrial Heterogeneity in Metabolic Diseases." Biology, 10(9), 927. https://doi.org/10.3390/biology10090927.

Employment:

UCLA Department of Molecular and Medical Pharmacology- Graduate Student- (Sept. 2018- Present)

MDxHealth Inc. – Product Development Associate (Product Development)- (Aug. 2016- Aug. 2018)

MDxHealth Inc. – Laboratory Technician (Laboratory Operations)- (Sept. 2015- Aug. 2016)

Geng Zeng Laboratory (UCLA Urology)- Laboratory Research Assistant- (May 2013- Sept. 2015)

Nanosmart Pharmaceuticals- Laboratory Research Assistant- (Jun. 2012- Jan. 2013)

Presentations:

UCLA Mitochondrial Symposium 2023- Poster Presentation (2023)

ISF Workshop on: Mitochondria: Past and Present- Poster Presentation (2022)

UCLA Mitochondrial Symposium 2021- Poster Presentation (2021)

Certification:

CERSI UCSF-Stanford: CERSI Immersion Course in Drug Discovery, Drug Development, and Regulation- Course Completion (2023)

Other:

UCLA IRB Accepted for “Respirometry in Human Salivary Leukocytes” (2024)

Los Angeles Public Library STEM Outreach Program Volunteer

SPARK101 Volunteer- STEM Outreach Program

INTRODUCTION

Assessing Mitochondrial Function in Humans

Since around the 1960s mitochondria have been simplistically characterized by the analogy that they are the “powerhouse of the cell”, a reference to their primary function to synthesize ATP through the membrane potential generated by the electron transport chain. While this function remains foundational to our understanding of mitochondria, this simplified uni-functional view of this organelle is now hugely outdated. Research of the last 40 years has revealed that mitochondria are complex and multifaceted organelles implicated in a wide range of metabolic and signal transduction pathways including the sensing, integration, and signaling of cell and tissue status (Picard and Shirihai 2022). This renewed vigor to more thoroughly understand the role of mitochondria has also revealed that mitochondrial dysfunction can play a major role in a wide variety of diseases including cancer, diabetes/obesity, and aging (Lopes et al. 2022; Billingham et al. 2022; Poznyak et al. 2020). Yet despite flourishing in the research space, in the clinical space the role of mitochondria in disease progression has been largely ignored. This is primarily a byproduct of the fact that our current diagnostic techniques (primarily mtDNA sequencing or tissue biopsies) fail to make mitochondrial function an easy diagnostic parameter to measure (B. G. Hill et al. 2019). This has created an unmet need in the mitochondrial field for an assay which can facilitate the measurement of mitochondrial function in humans so that we may better understand the impact of this organelle in human disease.

Respirometry is the Gold Standard for Measuring Mitochondrial Function

While mitochondrial status can be assessed in many ways including Western Blots, sequencing, and imaging, at the basis of mitochondrial assays is the measurement of mitochondrial function, more specifically respirometry. Respirometry is the measurement of

oxygen consumption through Complex IV of the electron transport chain (ETC), and it is the current gold standard to assess mitochondrial function. The reason for this is two-fold:

1. Scientists have developed increasingly precise ways to measure minute changes in the partial pressure of oxygen (and therefore by extension, oxygen consumption). Beginning with the days of the Clark electrode and progressing to more advanced and streamlined techniques like the Seahorse, the field has placed an emphasis on the ability to measure this metric very precisely.
2. Respirometry represents an integrated measurement which accounts for the rates of both anabolism and catabolism within a system. With a tight coupling between oxygen consumption by Complex IV and ATP production, respirometry is simultaneously altered by not only the ATP-consuming processes occurring downstream of Complex IV, but also the many catabolic processes which feed metabolites into the TCA cycle and ETC prior to oxygen consumption occurring at Complex IV.

With these factors in mind, respirometry has become a widely utilized tool for cell and animal models. Despite this excitement for this burgeoning technique in the research space, adapting respirometry practices for use in human samples has been limited. There have been two primary limitations to widescale adoption of respirometry as a technique: respirometry requires immediate processing of samples (within a few hours of acquisition), and respirometry requires the use of invasive tissue collections methods to obtain specimen for assessment.

The Respirometry in Previously-Frozen Specimen (RIFS) Assay Overcomes the Necessity of Immediate Sample Processing for Respirometry

With respect to the first hurdle for respirometry in humans, the requirement for immediate processing of samples, we have developed a novel processing solution. The Respirometry in Previously-Frozen Specimen (RIFS) assay allows for the measurement of maximal ETC activity from samples which have been previously frozen for storage. Traditional

respirometry techniques require fresh tissue due to the loss of cytochrome c and essential ETC substrates like NADH and succinate which are lost from the mitochondrial matrix during the freeze-thaw process. In the RIFS assay, exogenous cytochrome c and the requisite ETC substrates are added to the sample, allowing the measurement of maximal OCR. The RIFS assay permits samples to be collected at various times and/or locations, then frozen and shipped to locations with the instrumentation and knowledge to perform respirometry. The RIFS methodology is a crucial technical advancement for the adoption of respirometry, overcoming one of the fundamental challenges for clinical utilization.

Though the RIFS assay facilitates clinical respirometry, most methods measure mitochondrial function in skeletal muscle samples. While these samples are advantageous for respirometry due to high mitochondrial content and low heteroplasmy compared to other tissue types, they require highly invasive tissue biopsies to obtain (Acin-Perez et al. 2021). The reliance on primary tissue for respirometry is the most significant barrier to human utilization, though recent research has revealed that primary tissue may not be required to assess mitochondrial dysfunction. Tyrell et al (2016) show that the respirometry profiles of systemic biomarkers, including maximal respiratory capacity, correlate with that of skeletal muscle (Tyrrell et al. 2016). This and subsequent research reveals that metabolic dysfunction is systemic and can therefore be assessed in circulating cells.

Assessing Respirometry Non-invasively for Human Samples

Recently, researchers have begun to search for alternative tissues for respirometry, most notably peripheral blood mononucleocytes (PBMCs) isolated from whole blood and cultured fibroblasts. While both tissue types have shown some promise, they are suboptimal for clinical implementation. Both tissues are difficult to sample, difficult to process, and have limited practical utility as respirometry samples; PBMCs isolated from whole blood are often contaminated with platelets, which distort OCR measurements, and cultured fibroblasts have

altered metabolic characteristics compared to fibroblasts *in vivo* (Acin-Perez et al. 2021). With these challenges in mind, we need a respirometry sample that is easy to collect and easy to process.

We have identified that the cellular content in saliva is a sample material which overcomes the challenges of clinical respirometry. Previous research has shown that buccal epithelial cells in the oral cavity conserve mtDNA mutations found in the muscle or blood, suggesting its potential utility as a systemic biomarker of mitochondrial ETC status (Frederiksen et al. 2006). In this paper, we detail the development and troubleshooting of a novel respirometry assay which integrates the RIFS respirometry platform with novel salivary cell sample preparation. We found that salivary leukocytes represent a viable cell type for mitochondrial respiration which is not only easy to sample, but lacks the platelet contamination observed in similar blood-based energetics methods. This assay allows for the measurement of mitochondrial function in humans in a sample type which is easy to obtain and can be obtained repeatedly for time-course based studies, making respirometry in humans more feasible than ever before.

Overcoming the Hurdles to Respirometry in Human Samples

In this thesis we will discuss our solutions to the two primary hurdles preventing the adaptation of respirometry for human samples: the scalability of respirometry techniques, and the lack of accessible human tissues for respirometry. In Chapter 1 we will discuss the RIFS assay and how it overcomes the necessity for fresh sample for respirometry. In Chapters 2 and 3 we will discuss the utilization of the RIFS assay to measure respirometry of the human brain in high-resolution, a study which required new methodologies to scale respirometry techniques to a sample set larger than ever before seen. In Chapter 4 we will discuss the development of a methodology to measure respirometry in salivary leukocytes, a tissue type which is entirely non-invasive to sample and does not have many of the artifacts prevalent in other systemic

biomarkers for respirometry. Together these chapters unveil new techniques which make respirometry more feasible for adoption in human studies.

Chapter 1: Measuring Mitochondrial Respiration in Previously Frozen Biological Samples

Introduction

Impaired mitochondrial respiration plays a key role in metabolic, aging-related, and cardiovascular disease (Liesa, Palacín, and Zorzano 2009; Wallace 2011). Mitochondrial respiration results from the transfer of electrons between complexes I, II, III, and IV, with complex IV reducing oxygen to water; thus, oxygen consumption integrates electron transport activity from complexes I/II through IV. However, mitochondrial respirometry analysis currently requires processing and measurement of the living tissue sample within an hour of being taken from the patient. This requirement is set by the need to preserve the integrity of the inner mitochondrial membrane, needed both for integrated electron transfer between the complexes as well as to preserve the coupling of electron transfer to ATP synthesis. Consequently, the need to use fresh tissue to assess integrated electron transport activity makes respirometry analysis largely unfeasible for standard clinical practice and clinical studies. This limitation has significantly stalled scientific progress and virtually excluded the possibility of translating some discoveries in mitochondrial physiology into improved patient care. Here we describe a methodology to assess mitochondrial respirometry capacity in previously frozen biological specimens. This procedure (see flowchart in Fig. 1) overcomes the fundamental limitation of conventional respirometry approaches that require freshly isolated tissue, and also allows for the use of less biological material. Furthermore, our approach also allows for the use of a combination of substrates that permits selective measurements of respiratory capacity driven by complex I, II, or IV alone, resembling previous methods for determining isolated electron transport chain complex activity.

Detailed in Acin-Perez et al. (2020), the maximal respiratory capacity measured from frozen tissues using this assay is comparable to that measured in fresh tissue (Figure 2A) (Acin-Perez et al. 2020). Freeze-thawing impairs mitochondrial respiration by disrupting and

permeabilizing the mitochondrial inner membrane, which releases electron carriers that support the electron transport chain (Figure 2C). However, the interaction of electron transport complexes (supercomplexes) remains intact under freeze-thawing conditions, allowing for integrated electron transport as seen in fresh tissues. This article, therefore, provides instructions to rescue the defects induced by freeze-thawing, as well as to control the entry of electrons into the electron transport system by providing different electron carriers. As our procedure allows for the specific measurement of oxygen consumed by complex IV, mitochondrial isolation is no longer necessary, allowing for the use of homogenates to measure mitochondrial function, significantly simplifying tissue preparation (described in Basic Protocol 1).

The methodology described in this chapter is broken up into three subsections: Basic Protocol 1 for sample collection, storage, and homogenization for respirometry on previously frozen tissue; Basic Protocol 2 for running a Seahorse respirometry assay using previously frozen tissue samples; and Basic Protocol 3 for normalization to mitochondrial content for respirometry on previously frozen tissue (optional). Figure 1 provides a graphical representation of this method from start to finish. Basic Protocol 1 describes the process of dissecting a sample, freezing a sample for storage, and homogenizing a sample for a more simplified sample preparation. Basic Protocol 2 details the loading of the XF96 Seahorse sample plate, describes the compounds to be loaded into the Seahorse cartridge injection ports, and lays out the Seahorse protocol steps to measure respirometry in previously frozen tissues. Basic Protocol 3 describes how to use MitoTracker Deep Red staining to normalize samples to mitochondrial content rather than whole protein content. Completion of this series of protocols will allow users to progress from removing a tissue of interest from a specimen, freeze the tissue for later study, and set up a Seahorse assay to obtain complex I, II, and IV functional readings from the previously frozen tissue sample.

BASIC PROTOCOL 1: Sample Collection, Storage, And Homogenization For Previously Frozen Tissue Respirometry

The following protocol details how tissue samples should be collected and stored prior to being analyzed using the previously frozen tissue respirometry assay. In this protocol, the tissue of interest will be isolated from the organism and frozen for long-term storage. Samples will then be manually homogenized and isolated via centrifugation, or, optionally mitochondria may be isolated from the homogenate. Finally, a BCA protein assay will be performed to normalize the samples either for immediate loading or for normalization to mitochondrial mass (described in Basic Protocol 3). If the protocol is followed accurately, the samples should progress from whole tissue to a homogenate or mitochondrial isolate that is ready for normalized loading on a Seahorse sample plate in Basic Protocol 2.

This sample preparation protocol is optimized for mouse liver isolation. See Troubleshooting (Table 3) for alterations to be made for the collection, preparation, and measurement of other tissue types using the frozen tissue respirometry method.

Materials

Mice

Phosphate-buffered saline (PBS; Sigma, P3813)

Liquid nitrogen (optional)

1× MAS buffer (see recipe)

Collagenase Type II (Worthington Biochemical, 4174; optional)

BCA Protein Assay Kit (ThermoFisher, 23225, or equivalent)

Scissors and other dissection tools

Glass-glass or glass-Teflon Dounce homogenizer

Refrigerated centrifuge

Additional reagents and equipment for euthanasia of mice ((see Current Protocols article: Donovan and Brown 2006)

Tissue Collection

1. Euthanize mice using isoflurane anesthesia followed by cervical dislocation (see Current Protocols article: Donovan and Brown 2006)) as approved by Institutional Guidelines for Animal Care in compliance with U.S. Public Health Service Regulations.

2. Dissect the tissue of interest, wash with PBS, and optionally mince with scissors.

When possible, dissections should be done on ice to keep the tissue as cold as possible.

3. Snap freeze in liquid nitrogen. For long-term storage, store the frozen tissue at −80°C.

Liver samples have been shown to have little loss in respirometry results if stored at room temperature or 4°C for up to 3 hr prior to being snap frozen (Fig. 3A).

Though snap freezing is the most ideal method of tissue preparation, the tissue may be immediately stored at −80°C or at −20°C for up to 4 hr prior to being stored at −80°C without affecting the respirometry results (Fig. 3B).

Tissue homogenization

4. Thaw samples in ice-cold PBS and mince with pre-chilled scissors or razor blades.

5. Homogenize using 250 µl to 500 µl per 10 mg of tissue of ice-cold MAS buffer using the appropriate homogenizer (Fig. 3C illustrates this process). For liver, brown adipose tissue, brain, kidney, lung, and skeletal muscle, use ten to twenty strokes in a glass-Teflon Dounce homogenizer. For heart and white adipose tissue, use twenty strokes in a glass-glass Dounce homogenizer.

CRITICAL: For muscle tissue, incubate homogenized tissue in collagenase Type II (0.25 mg/ml final concentration) in MAS at 37°C for 30 min prior to centrifugation.

Our studies have shown that using smaller-volume homogenizers (e.g., using a 7-ml homogenizer rather than a 15-ml homogenizer when working with <5 ml of sample material) results in less sample retention in the homogenizer and produces better homogenization.

6. Centrifuge homogenates 5 min at 1000 × *g*, 4°C.

CRITICAL: If using swinging-bucket centrifuge, measure the precise distance between rotor center and the center of mass of the liquid homogenate in the tube in the horizontal swinging position in order to correctly calculate the *g* to rpm conversion:

$$\text{rcf (g)} = 1.12 * \text{radius (mm)} * \left(\frac{\text{rpm}}{1{,}000}\right)^2$$

7. Collect the resulting supernatant as the homogenate sample. Discard the pellet (Fig. 4). The supernatant (tissue homogenate) may be stored at −80°C for long-term storage.

This sample may also be used for other assays like enzymatic assays, western blots, or Blue Native gel electrophoresis.

8. If you are running the sample as a tissue homogenate, perform a BCA protein assay to normalize your samples according to protein content prior to loading on the Seahorse XF96 sample plate (Fig. 5B, Method 1). If you are normalizing according to mitochondrial content, perform a BCA protein assay and continue with the steps detailed in the optional Basic Protocol 3 (Fig. 5B, Method 2). If you are isolating mitochondria from the tissue homogenate, proceed with the following steps for mitochondrial isolation protocol.

Mitochondrial Isolation From Homogenate (Optional)

9. If mitochondrial isolation is desired, centrifuge the rest of the homogenate preparation (the supernatant from the above centrifugation) 10 min at 10,000 × *g*, 4°C.

10. Optionally, wash mitochondrial pellets twice in 1× volume of MAS buffer, each time centrifuging as in step 9.

11. Re-suspend final mitochondrial pellet in ice-cold MAS buffer.

12. Perform a BCA protein assay using the mitochondrial homogenates. This may be used to normalize the sample according to protein content for loading, or optionally to prepare for mitochondrial mass normalization using MitoTracker Deep Red dye as described in Basic Protocol 2.

Sample Data

Figures 3C and 4 depict the results one should obtain after sample collection. Figure 3C shows a mouse liver sample that has been homogenized using a glass-Teflon homogenizer. Figure 4 shows the same sample after centrifugation, highlighting the pellet formed (which should be discarded) and the supernatant (which should be saved). If this sample separation does not occur after centrifugation, you should repeat the centrifugation step a second time.

BASIC PROTOCOL 2: Running A Seahorse Respirometry Assay Using Previously Frozen Tissue Samples

This protocol will detail the process of loading normalized samples onto an XF96 Seahorse plate, loading the Seahorse cartridge with compound injections, and running samples on the Seahorse platform. Samples will be loaded onto a XF96 sample plate, then centrifuged and diluted before loading the plate onto the Seahorse. Additionally, this protocol describes the loading of the Seahorse cartridge with compound injections. If this protocol is followed accurately, an operator will be capable of loading samples onto an XF96 sample plate, loading compound injections into a Seahorse cartridge, and running the plates on a Seahorse XF96 system. While this protocol is optimized for use with the Seahorse platform, with optimization, it could be adjusted to work with other respirometry platforms like the Oroboros.

Materials

Tissue homogenates or mitochondrial isolates (Basic Protocol 1)

1× MAS buffer (see recipe)

Cytochrome c (Sigma, C2506)

Alamethicin (Sigma, A4665; optional)

NADH (Sigma, N8129)

Succinate (Sigma, S9512)

Rotenone (Sigma, R8875)

Antimycin A (ENZO, ALX380075M010)

TMPD (Sigma, 87890)

Ascorbic acid (Fisher, A61-100)

Sodium azide (Sigma, S8032)

Potassium hydroxide (KOH)

Hydrochloric acid (HCl)

Seahorse XF96 flux pack (Agilent 102416-100)

Swinging-bucket centrifuge with plate carrier adapter

Multichannel pipettes

Seahorse XF96 instrument

1. Load homogenates or mitochondrial isolates, based on your BCA normalization results, into a Seahorse XF96 microplate (from the Seahorse XF96 flux pack) in 20 µl of MAS buffer. Optimal loading concentration will vary depending on the sample material, but for most samples a concentration between 2.5 and 20 µg of sample per well will be sufficient. See Table 3 in the Troubleshooting section of this document for approximate loading concentrations for different tissue types.

    Coating the XF96 plate with substrates promoting cell adhesion like laminin, Cell-Tak, and poly-D-lysine has been shown to not improve performance.

2. Centrifuge the loaded plate 5 min at 2000 × *g*, 4°C, using a plate carrier.

CRITICAL: Turn OFF the centrifuge brake and let buckets slow down by themselves. Sudden deceleration due to braking will result in uneven distribution of materials on the bottom of the plate.

3. Carefully add 130 µl (or enough to achieve a final volume of 150 µl) per well of 1× MAS buffer containing cytochrome *c* (10 µg/ml, final concentration) for homogenates, or the same volume of MAS buffer alone for isolated mitochondria.

CRITICAL: For brain and lung homogenates, add alamethicin (10 µg/ml, final) to the MAS buffer containing cytochrome *c* to allow complete membrane permeabilization to substrates.

4. Load the cartridge to deliver 25 µl of the following injections (Fig. 6A):

   a. Port A: NADH (1 mM) for complex I assessment, or 5 mM succinate + 2 µM rotenone for complex II assessment.
   b. Port B: Antimycin A (4 µM)
   c. Port C: TMPD + ascorbic acid (0.5 mM TMPD + 1 mM ascorbic acid)
   d. Port D: Sodium azide (50 mM) at port D.

   All compound injections should be diluted in 1× MAS buffer. When making the TMPD + ascorbate solution, add 0.5 mM TMPD into 1 mM ascorbate and adjust the solution to pH 7.2 using potassium hydroxide (KOH) and hydrochloric acid (HCl). NADH and TMPD/ascorbate solutions must be made freshly on the day of the assay, but all other compound injections can be made ahead of time and stored at −20°C until time of use.

5. Mix and measure times for the Seahorse run protocol are 0.5 and 4 min, respectively. If a protocol includes an oligomycin injection, a 2-min wait time should be included between the injection of oligomycin and the 4-min measurement period (Fig. 6B).

Figure 6B describes a typical Seahorse program.

Sample Data

Figure 6C depicts a representative Seahorse trace for a standard assay which measures complex I, II, and IV in mouse liver homogenates. Figure 6C-I and C-II highlight the complex I NADH peak and complex II succinate + rotenone peak, respectively. Figure C-IV highlights the complex IV TMPD + ascorbate peaks from the complex I and complex II samples. This Seahorse trace not only has distinct peaks for all substrate injections, but also has strong and distinct responses to the inhibitors (antimycin A and azide) used in the assay, making it an optimal-looking trace.

BASIC PROTOCOL 3: Normalization To Mitochondrial Content For Previously Frozen Tissue Respirometry (Optional)

The following protocol describes normalization of the results from respirometry samples according to mitochondrial content. Homogenates or mitochondrial isolates (made in Basic Protocol 1) will undergo MitoTracker Deep Red (MTDR) staining and measurement. Using this data, samples can be normalized based on their mitochondrial content rather than using a whole protein measurement.

Materials

Tissue homogenates or mitochondrial isolates (Basic Protocol 1) or Seahorse sample plate from Basic Protocol 2

1× MAS buffer (see recipe)

MitoTracker Deep Red FM (MTDR; Thermo, M22426)

Clear, flat-bottom, black 96-well plate (Corning, 3904 or equivalent)

Seahorse XF96 flux pack (Agilent 102416-100) including sample plate

Multichannel pipette

Refrigerated centrifuge with plate adapter

Fluorescence plate reader or high-throughput microscope

Normalizing To Mitochondrial Content

For protein content−based normalization using homogenates or mitochondrial isolates, use the BCA protein data previously generated (in Basic Protocol 1) to load equivalent protein amounts in the XF96 Seahorse plate as described in Basic Protocol 2 (Fig. 5B, Method 1).Normalization for mitochondrial content using MitoTracker Deep Red (MTDR) may be performed before or after running the Seahorse sample plate.

While MTDR normalization can be performed at any step after BCA values have been generated, loading onto the Seahorse sample plate is exclusively done based on BCA values. Normalization to mitochondrial content should only be done after oxygen consumption rate (OCR) values are obtained.

Normalizing To Mitochondrial Content Before Running A Seahorse Experiment (Fig. 5B, Method 2a)

1a. Perform protein normalization via BCA assay as described above (Basic Protocol 1).

2a. On a clear, flat-bottom, black, 96-well plate, seed 2.5-80 µg of mitochondria or lysate sample (according to protein normalization values) in 100 µl of MAS buffer containing MTDR at 1 µM final concentration.

If your sample material is limited, MTDR normalization may be done in the XF96 sample plate afterwards, or using a sister plate loaded alongside the XF96 sample plate.

3a. Incubate the sample plus dye at 37°C for 10 min.

4a. Remove the dye by centrifuging the sample 5 min at 2000 × *g*, 4°C, with no brake for deceleration. Carefully remove the supernatant and resuspend in 100 µl of MAS buffer.

5a. Measure fluorescence in a plate reader or high-throughput microscope using a clear-bottom black 96-well plate (Corning 3904 or equivalent). MTDR is excited at 625 nm and emits at 670 nm.

6a. Calculate relative mitochondrial content after controlling for background fluorescence using a blank well.

Normalizing To Mitochondrial Content After Running A Seahorse Experiment (Fig. 5B, Method 2b)

1b. Remove the Seahorse sample plate from the Seahorse machine.

2b. Carefully, without agitation of the sample material at the bottom of the Seahorse sample plate, remove the MAS buffer from the plate until approximately 80 µl of liquid remains in each well.

3b. Add 20 µl of 5 µM MTDR in MAS buffer to each sample such that each sample now has 100 µl of liquid with a final MTDR concentration of 1 µM.

4b. Incubate the sample plus dye at 37°C for 10 min. Ensure that the incubation period is no more than 10 min; too long of an incubation period can result in high background MTDR fluorescence.

5b. Add 100 µl of MAS buffer without MTDR to each sample. Remove 100 µl of solution from each well. Perform this washing procedure up to three times.

6b. Measure fluorescence in a plate reader or high-throughput microscope.

MTDR is excited at 625 nm and emits at 670 nm.

7b. Calculate relative mitochondrial content after controlling for background fluorescence using a blank well. For absolute quantification, use an isolated mitochondria standard.

Sample Data

Table 1 showcases data from a MTDR plate reader assay to normalize mouse liver by mitochondrial content before loading a Seahorse sample plate. The columns titled “raw absorbance units” and “µg of protein loaded via BCA” will be filled in by the user based on the plate reader results and the amount of protein added to the plate for the MTDR reading (determined via BCA). Dividing the raw absorbance minus the background absorbance and the µg of protein loaded results in the data in the farthest right column entitled “(Raw AU - background)/(µg protein),” which is now a reading of mitochondrial content per µg of protein in

the sample. Normalization may then be performed such that the OCR values obtained are normalized to measurements of OCR per mitochondrial content.

Reagents And Solutions

MAS buffer, 1×

70 mM sucrose (Fisher, L-12686)

220 mM mannitol (Sigma, M9546)

5 mM KH_2PO_4 (Sigma, P5655)

5 mM $MgCl_2$ (Sigma, M0250)

1 mM EGTA (Sigma, E4378)

2 mM HEPES (Corning, 25-060-CI)

Adjust to pH 7.4 using potassium hydroxide (KOH) or hydrochloric acid (HCl). Store up to 1 year or longer at −20°C.

Commentary

Background Information

Mitochondrial respiration results in the transfer of electrons between electron transport chain complexes I, II, III, and IV, with complex IV reducing oxygen to water. With oxygen playing a primary and crucial role in the process, respirometry platforms like the Seahorse or Oroboros use the measurement of oxygen consumption rate as a surrogate marker for mitochondrial activity. Current mitochondrial respirometry techniques for in vivo samples require that the processing and measurement of the living tissue sample happen within an hour of isolation from the specimen. This requirement is set by the need to preserve the integrity of the inner mitochondrial membrane, needed both for integrated electron transfer between the complexes as well as to preserve the coupling of electron transfer to ATP synthesis. Although freeze-thawing disrupts and permeabilizes the mitochondrial inner membrane, our novel respirometry method overcomes this challenge to allow for previously frozen tissue samples to be measured.

Mitochondrial supercomplexes remain intact despite freeze-thawing; therefore, we have developed a set of substrates that are capable of measuring complex I, II, and IV through measurement of these supercomplexes. While this assay cannot measure coupled mitochondrial respiration, as can be done in fresh tissue respirometry, freezing tissues allows for long-term tissue storage and simplified sample processing through use of tissue homogenates, thereby enabling respirometry experiments that are less time-intensive, require less tissue processing, and are less expensive, facilitating large-scale respirometry research studies when compared to current respirometry methods.

Critical Parameters

Multiple parameters within this methodology are critical to obtaining good results from your respirometry run. In Basic Protocol 1, the most critical parameter to success is the homogenization step. If there is too little homogenization, mitochondria will not be released from the cell, resulting in low yield; too much homogenization might impact the mitochondrial supercomplexes. We have provided guidelines for the types of homogenizers and the number of strokes required for different tissues, but this could be a variable to optimize if you are getting suboptimal mitochondrial yield from your tissue samples.

Basic Protocol 2 is likely the part of the procedure that is most sensitive to certain experimental parameters. The most important parameter in this basic protocol is that centrifugation steps be done with the centrifuge brake turned OFF. Braking during deceleration of the centrifuge can result in an uneven distribution of the sample across the bottom of the Seahorse sample plate, adversely effecting OCR results and reproducibility. A centrifuge with the capability of having the brake turned off is necessary for best performance in this assay. An additional variable to consider for this part of the assay is how much sample is being loaded onto the sample plate. Too little sample and OCR values will be very low, but having too much sample can result in oxygen depletion and inconsistent responses to the compound injections (diagnosing these

issues is discussed in the Troubleshooting, below). We recommend titrating your sample material to find the optimal loading concentrations that provide the best Seahorse results. Basic Protocol 3 has few parameters that are critical to results, but it must be noted that while normalization to mitochondrial content is optional, it provides an additional analysis technique that may explain differences in respiration due to samples having differing numbers of mitochondria. An example of where this may be impactful is if two samples have the same OCR reading, but one sample has fewer mitochondria that have higher respiratory capabilities and the other has many mitochondria that have low respiratory capabilities. In this scenario, normalizing the data to mitochondrial content could elucidate these differences.

Troubleshooting

This troubleshooting section is designed to account for issues specific to frozen tissue respirometry, although traditional Seahorse troubleshooting techniques will likely also apply to this technique. Figure 6C displays a representative Seahorse trace for a standard assay measuring complexes I, II, and IV in liver homogenates. Table 2 describes factors that may cause poor respirometry results. Additionally, this table catalogs how to diagnose these errors and the potential solutions to improve respirometry sample performance. This protocol was initially optimized for frozen liver respirometry, but many other tissue types have been successfully tested using this procedure, with some modifications. Table 3 compiles some of the potential optimizations in tissue collection and respirometry when using alternative tissue types with this protocol. Further examples of respirometry results using alternative tissue types including Seahorse traces can be found in Acin-Perez et al. (2020); also see Table 3.

Statistical Analysis

When the Seahorse run is complete, export the oxygen consumption rates (OCRs) from the Agilent Wave software and (if applicable) normalize by mitochondrial mass (MTDR readings) in

Microsoft Excel. Calculate complex I-, II-, and IV-dependent respiration by the following formulas:

1. Maximal respiratory capacity through complex I:

$$OCR_{NADH} - OCR_{antimycin}$$

2. Maximal respiratory capacity through complex II:

$$OCR_{succinate+rotenone} - OCR_{antimycin}$$

3. Maximal respiratory capacity through complex IV:

$$OCR_{TMPD+Ascorbate} - OCR_{azide}$$

Calculating the complex I to complex IV or complex II to complex IV ratio may serve as an alternative measurement of complex respiratory capacity.

Understanding Results

Figure 6C exhibits a representative Seahorse trace. The trace in red corresponds to a complex I peak (Figure 6C-I) followed by a complex IV peak (Figure 6C-IV) induced by NADH and TMPD/ascorbate, respectively. The trace in blue corresponds to a complex II peak (Figure 6C-II) followed by an additional complex IV peak (Figure 6C-IV) induced by succinate/rotenone and TMPD/ascorbate, respectively. This sample responds to all substrate and inhibitor injections and has relatively low standard deviations for each measurement across the three replicates tested. When analyzing the data, the primary data points of importance will be Figure 6C,D, the complex I respiration induced by NADH addition, Figure 6C,C-II, the complex II respiration induced by succinate addition, and Figure 6C,C-IV, the complex IV respiration induced by TMPD + ascorbate addition. The measurements after antimycin A injection and azide injection are used primarily as background controls where the antimycin A measurement represents any respiratory activity not produced by the non-mitochondrial respiration of the electron-transport chain complexes, and the azide measurement represents any non-mitochondrial respiratory activity still in the sample. Figure 7 showcases Seahorse traces which are not ideal. The

Troubleshooting section, above, describes potential reasons for why certain traces may look like those in Figure 7.

Time Considerations

Basic Protocol 1 will take approximately 2 hr for 15 samples, not including dissection of the tissue of interest from the specimen (the time to do this will depend on the specimen and tissue being used). This time is largely based on manual homogenization of the samples; an automated system of tissue homogenization could dramatically decrease the sample processing time, although these methods would need to be optimized for the purpose of this assay. Basic Protocol 2 will take approximately 2 hr to set up for 15 samples, then the Seahorse run will take approximately 90 min, with no user input required. This process could be easily scaled up for more samples with multiple Seahorse instruments, where larger volumes of each compound injection could be made for multiple Seahorse cartridges. Basic Protocol 3 will take approximately 30-60 min for 15 samples. In total, 15 samples will take approximately 6 hr, although this time can be split between 1 day of sample processing and storage and 1 day of running the Seahorse assay.

Figures

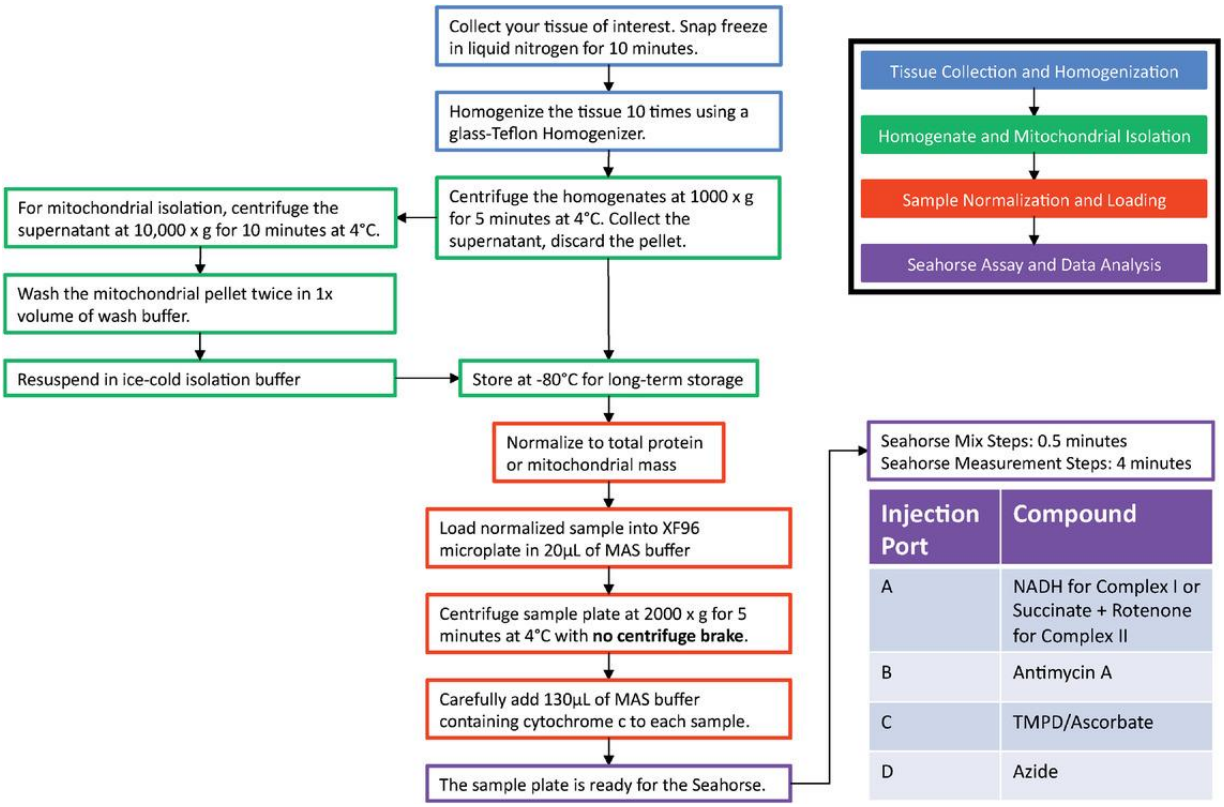

Figure 1: RIFS Protocol Flowchart

Flowchart of the frozen tissue respirometry protocol detailing the most important steps. The sections of the protocol are outlined in the top right box, which will be referred to in subsequent figures.

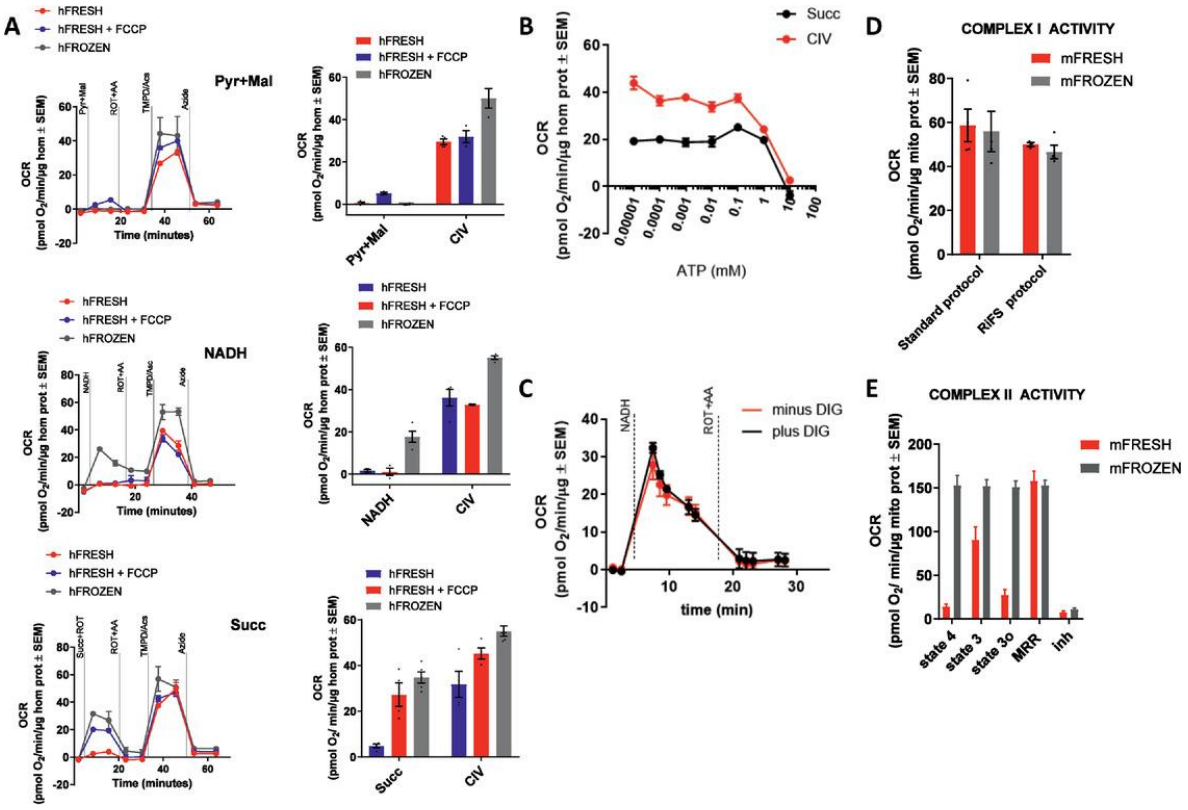

Figure 2: Respirometry Measurements of Complex I, II, and IV Comparing Fresh Versus Frozen Tissue Protocols.

Respirometry measurements of complex I, II, and IV comparing fresh versus frozen tissue protocols. **(A)** The Seahorse traces and associated OCR (oxygen consumption rate) quantifications of mouse liver homogenates. hFresh represents liver homogenate which was isolated and tested without being frozen. TMPD is added to a subset of the hFresh samples to uncouple the mitochondria to survey complex activity separately from ATP-linked respiration. hFrozen represents liver homogenates which underwent the frozen respirometry protocol. While complex IV was surveyed using TMPD/ascorbate for all three assays, the top graph was first stimulated with pyruvate + malate, the middle with NADH, and the bottom with succinate + rotenone. **(B)** Succinate + rotenone and TMPD + ascorbate−dependent oxygen consumption rate measured in the presence of a titration of ATP concentrations. **(C)** Oxygen consumption rate in response to NADH injection for frozen liver homogenate treated with or without digitonin

to control whether the mitochondria are fully broken and substrates can directly fuel the electron transport chain. **(D)** Complex I and complex II activity (measured as oxygen consumption rate). **(E)** Oxygen consumption rates of fresh and frozen mitochondria respiring under succinate+rotenone. Fresh mitochondria respond to ADP, oligo, FCCP, and AA, whereas frozen mitochondria, being uncoupled from the beginning, only respond to AA.

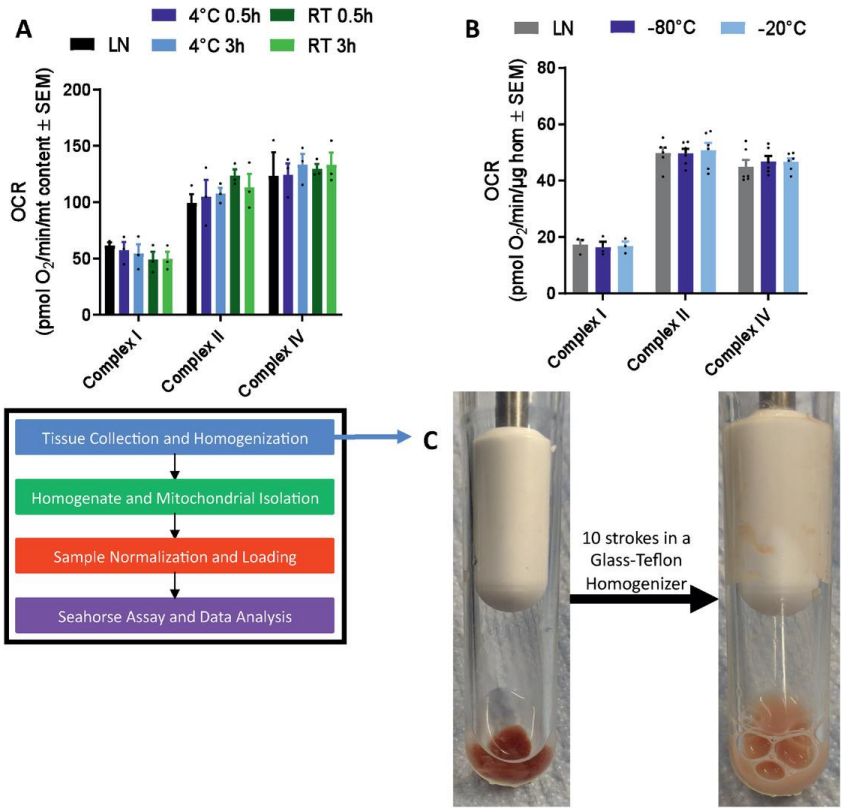

Figure 3: Tissue Collection and Homogenization

Tissue collection and homogenization. **(A)** Complex I, complex II, and complex IV oxygen consumption rates of mouse liver homogenates. Liquid nitrogen (LN) samples were immediately snap-frozen after isolation: 4°C 0.5 hr and 4°C 3 hr were kept at 4°C for 0.5 and 3 hr, respectively after isolation prior to being snap-frozen. RT 0.5 hr and RT 3 hr were kept at room temperature for 0.5 and 3 hr, respectively after isolation prior to being snap-frozen. **(B)** Complex I, complex II, and complex IV oxygen consumption rates of mouse liver homogenates. LN

homogenates were isolated then snap-frozen in liquid nitrogen prior to storage at −80°C. −80°C samples were isolated then stored at −80°C until homogenization. −20°C samples were isolated then stored at −20°C for 4 hr before being stored at −80°C until homogenization. **(C)** Mouse liver before and after 10 strokes of homogenization using a glass-Teflon homogenizer.

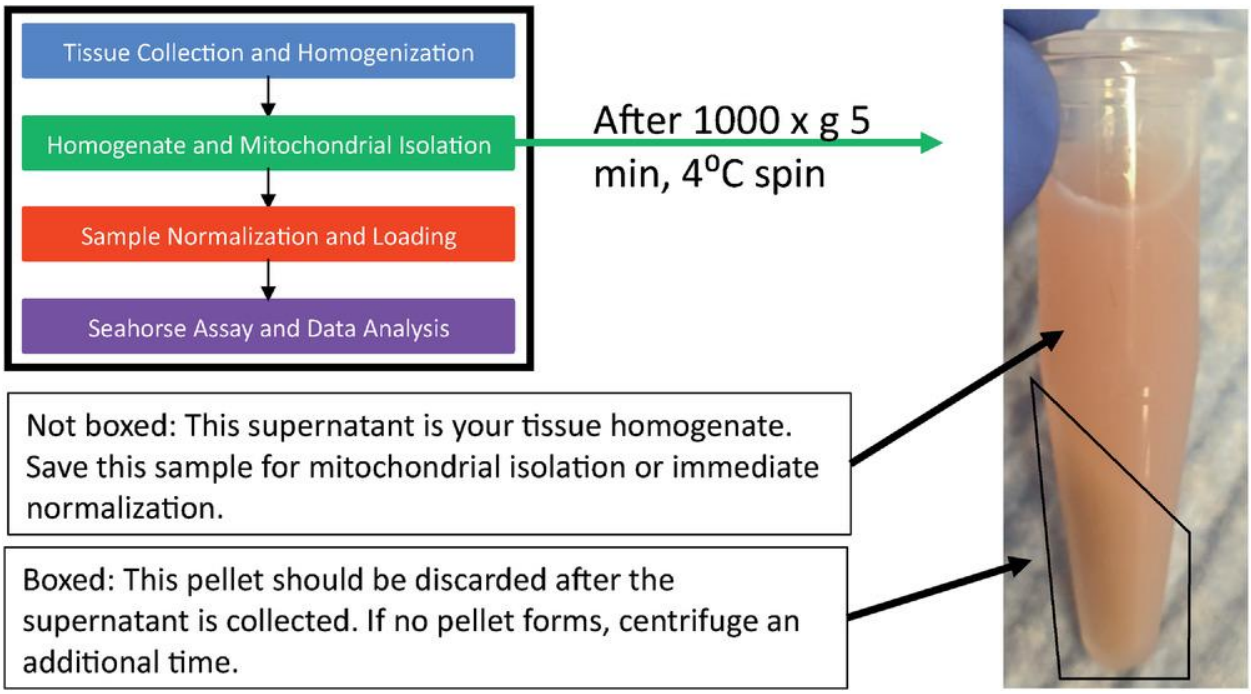

Figure 4: Homogenate Isolation from Frozen Tissues

Homogenate isolation from frozen tissues. After homogenization, the homogenate must be isolated from the cellular debris. This is performed using a 1000 × g centrifugation for 5 min at 4°C. Highlighted in this figure is the pellet resulting from this centrifugation (boxed) and the supernatant (not boxed). The supernatant is your tissue homogenate, which should be collected and may be used for normalization prior to respirometry, for mitochondrial isolation, or for non-respirometry assays like Blue Native Gel Electrophoresis. The pellet should be discarded.

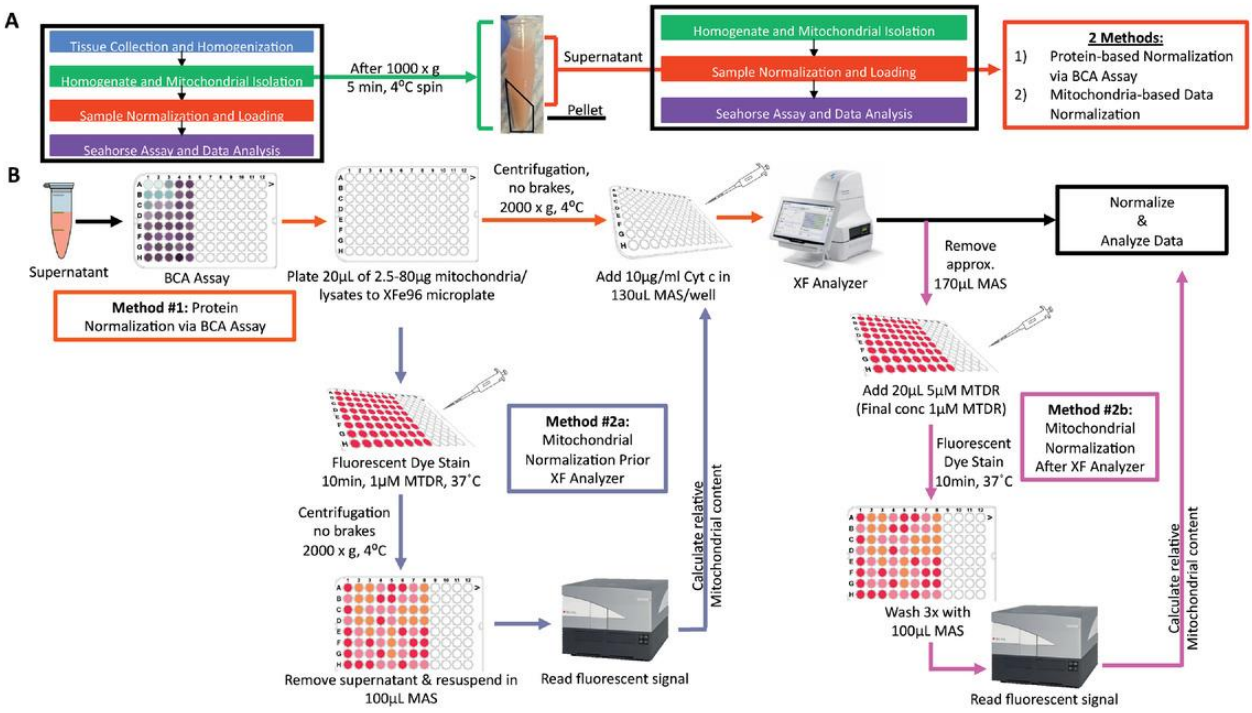

Figure 5: Normalization and Loading of Tissue Homogenates or Mitochondrial Isolates

Normalization and loading of tissue homogenates or mitochondrial isolates. Normalization may be performed in one of two ways: protein normalization using a BCA assay or mitochondrial mass normalization using MTDR dye. Method 1 describes the protein-based normalization using the BCA assay. Method 2a describes mitochondrial normalization performed prior to running the XF96 Seahorse plate. Method 2b describes mitochondrial normalization performed after running the XF96 Seahorse plate.

A

Injection Port	Compound
A	NADH for Complex I or Succinate + Rotenone for Complex II
B	Antimycin A
C	TMPD/Ascorbate
D	Azide

B

Action	Time in Minutes
Mix	2
Wait	2
Mix	2
Wait	2
Mix	0.5
Measure	4
Mix	0.5
Inject	
Mix	0.5
Measure	4
Mix	0.5
Measure	4

Repeat 4 times injecting port A, B, C, then D.

C

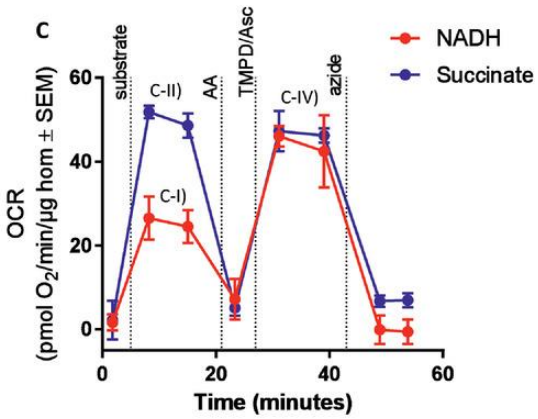

Figure 6: A Standard Frozen Tissue Respirometry Method, Compound Injections, and Seahorse Trace

A standard frozen tissue respirometry method, compound injections, and Seahorse trace. **(A)** An example frozen respirometry Seahorse protocol. **(B)** Sample compounds for injection ports for the measurement of complex I or complex II oxygen consumption in frozen tissues. **(C)** An optimal Seahorse trace measuring ETC complexes I, II, and IV. Red trace represents NADH and complex IV dependent and blue trace represents succinate and complex IV dependent respiration. (C-I) NADH-induced respiration, representative of complex I activity. (C-II) Succinate + rotenone-induced respiration, representative of complex II activity. (C-IV) TMPD + ascorbate-induced respiration, representative of complex IV activity.

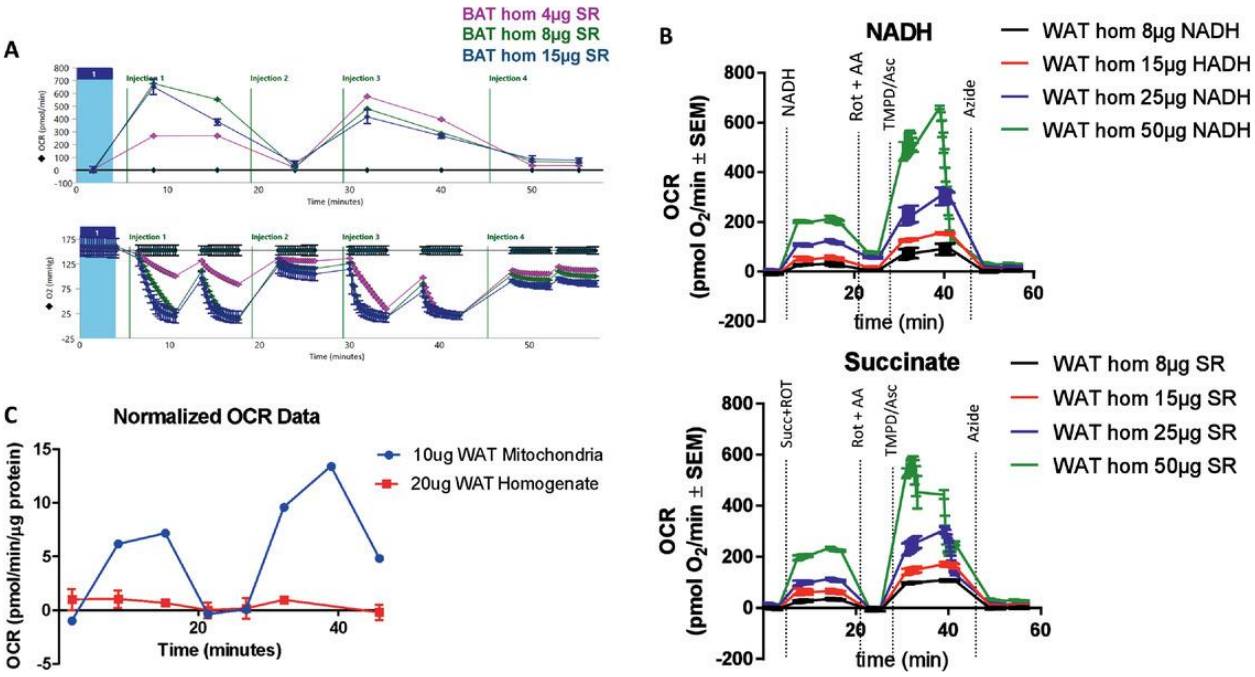

Figure 7: Troubleshooting Frozen Tissue Respirometry Seahorse Traces

Troubleshooting frozen tissue respirometry Seahorse traces. **(A)** A brown adipose tissue (BAT) sample exhibiting signs of oxygen depletion. The top graph of A shows OCR, and the bottom graph shows oxygen levels. At 4 µg of loaded sample, oxygen levels deplete linearly for both measurements after injection 1. As more sample is loaded, oxygen depletion becomes less linear, and between the two measurements oxygen levels do not fully recover, both of which are signs of oxygen depletion affecting respiration results. **(B)** A white adipose tissue (WAT) sample exhibiting inconsistencies between measurement 1 and measurement 2 after compound addition. With 50 µg of WAT loaded, measurement 2 after TMPD/ascorbate addition begins high, but drops dramatically as the measurement cycle continues, ultimately affecting the overall respirometry trace. When the sample input is decreased, measurements normalize and the drop in measured OCR is not observed. **(C)** A white adipose tissue (WAT) sample measured at 20 µg as a homogenate and measured at 10 µg after concentrating the sample by pelleting the sample and resuspending in a lower volume.

Tables

Table 1: Sample MTDR Plate Reader Assay Data

Sample Number	Raw Absorbance Units (AU)	Raw AU - Background	ug protein loaded via BCA	(Raw AU-Background)/(ug protein)
Background	1940			
1	21540	19600	10	1960
2	19411	17471	10	1747.1
3	23593	21653	10	2165.3
4	36932	34992	10	3499.2
5	41933	39993	10	3999.3
6	18971	17031	10	1703.1
7	34057	32117	10	3211.7
8	39941	38001	10	3800.1
9	49203	47263	10	4726.3

Table 2: Troubleshooting

Observation	Etiology	Solution	Additional Confirmation of Etiology
Low Respiration	Insufficient mitochondrial mass	Remeasure respiration using a larger amount of sample material. Alternatively, using mitochondrial isolates rather than whole tissue homogenate can improve the results when using lower mitochondrial mass samples.	Confirm your mitochondrial content using the assays described in the 'Normalization to Protein or Mitochondrial Content' section of this document.
	Homogenate too dilute/ low mitochondrial mass to total protein ratio	Concentrating the sample material by centrifuging at very high speeds and resuspending in a lower volume can limit the amount of non-mitochondrial "debris" which may clog the pores of the Seahorse plate. Additionally, titrating the amount of sample loaded into the Seahorse plate may also improve performance.	This can be common in tissues like WAT which may have a lot of non-mitochondrial "debris" which can block the pores of the Seahorse plate. This phenotype commonly causes high variability between samples, oxygen depletion, and possible lack of response to compound injections.

	Tissue degredation	Ensure that all samples, buffers, and equipment are kept ice-cold during all steps of the procedure to prevent tissue degredation from occuring.	Confirm that the mitochondrial supercomplexes of your sample are intact using Blue Native Gel-Electrophoresis (BNE).
	Incomplete uncoupling or permeabilization	Add 10 µg/mL final concentration of alamethicin (or your chosen permeabilization agent) to the assay buffer.	Some compounds may have problems getting through samples with a lot of membranous material. One way to check if incomplete permeabilization is occuring is to observe that your sample remains sensitive to oligomycin after treatment with a mitochondrial uncoupler.
	Over-permeabilization	Titrate the detergent until supercomplexes are intact and respiration is elicited with membrane-impermeable substrate NADH.	Confirm that the mitochondrial supercomplexes of your sample (after detergent addition) are intact using Blue Native Gel-Electrophoresis (BNE).
	Insufficient cytochrome c	Titrate cytochrome c for your samples.	Measure cytochrome c in your preparation and supernatant.
	Excess mitochondrial mass (Oxygen depletion)	Down-titrate the amount of sample loaded into the wells to prevent oxygen depletion.	Check the oxygen traces generated during the run in the Seahorse software. J-curving and negative oxygen values (examples shown in Figure 7A) are associated with oxygen depletion.
	Mitochondria are not evenly distributed on the bottom of the sample plate.	If a centrifuge brake is applied when spinning down the sample plate, it is possible that the mitochondria will not be evenly distributed along the bottom of the wells of the Seahorse plate.	Viewing the sample plate under a microscope prior to running the Seahorse will determine if the mitochondria are not evenly distributed along the bottom of the plate.
No NADH Response	Incomplete permeabilization	Add 10 µg/mL final concentration of alamethicin (or your chosen permeabilization agent) to the assay buffer.	The sample remains sensitive to oligomycin after treatment with a mitochondrial uncoupler.

No Succinate+Rotenone Response	Old stocks of S/R	Remake the stocks of Succinate + Rotenone.	After prolonged storage, Succinate + Rotenone may begin to precipitate out of solution.
No Antimycin A response	Non-mitochondrial respiration	Running a mitochondrial isolation rather than homogenates can prevent the observation of non-mitochondrial respiration impacting the results.	Incomplete inhibition of OCR by antimycin A can be common in some human samples. This typically respresents non-mitochondrial respiration can impact OCR under AA.
No TMPD/Ascorbate response	pH imbalance	Adjust the solution to reach pH 7.4 using HCl and KOH.	Test the pH of the TMPD + Ascorbate solution to ensure it is pH 7.4.
After Compound Injection, measurement 1 is dramatically different from measurement 2	Oxygen depletion	Down-titrate the amount of sample loaded into the wells to prevent oxygen depletion. Adding a wait or mixing step in between measurement 1 and measurement 2 can allow oxygen levels to equilibrate between measurements to eliminate variability between the two measurements.	Check the oxygen traces generated during the run in the Seahorse software. J-curving and negative oxygen values (examples shown in Figure 7A-7B) are associated with oxygen depletion.
	NADH Depletion	Higher injection concentrations of NADH, multiple NADH injections, or decreasing mitochondrial loading can alleviate potential NADH depletion.	For Complex I measurement it is possible that with high mitochondrial loading in certain cell types, NADH depletion may occur after measurement 1.
TMPD+Ascorbate-induced OCR is lower than Complex I/II OCR values	Excess mitochondrial mass	Decrease the amount of sample loaded into the sample plate.	Diminished TMPD values can occur as a result of oxygen depletion related to having too much mitochondrial mass loaded

Table 3: Tissue Type Adjustments

Tissue Type	Tissue Collection/Isolation	Respirometry Considerations	Approximate Loading Amounts
Heart	A glass-glass dounce homogenizer should be used to more thoroughly disrupt the tissue for the best results.		1-2 µg

White Adipose Tissue	A glass-glass dounce homogenizer should be used to more thoroughly disrupt the tissue for the best results. Spin samples at 20,000 rpm to further concentrate the sample and potentially remove the fat from the mitochondria.	Using more highly concentrated samples can prevent potential blockage of the measurement pores in the Seahorse plate (Figure 7C)	10-15 µg
Muscle	Increasing the number of homogenization strokes can improve the results with fibrous tissues like muscle. Alternatively, using collagenase type II at 0.25mg/mL final concentration during homogenization can aid in the tissue homogenization process.		6-8 µg
Human samples- white adipose tissue, liver, tumor samples, etc.	Human tissues often have more connective tissue and therefore require more strokes with the homogenizer or enzymatic digestion for the best results.	Human tissues often respire at lower rates than mouse tissues or cell lines. To compensate for this, more tissue should be loaded into the Seahorse plate.	Human Liver: 15-20 µg, Human Adipose Tissue: 10-15 µg, Human Tumor: 8-12 µg
Cell pellets	Alamethicin addition may help further permeabilize the cells. Necessity for extra permeabilization is largely cell-type dependent and should be titrated prior to use in respirometry.		Depends on cell type
Brain	Cells from the brain can often be very membrane rich. To compensate for this, alamethicin may be added to further permeabilize the cells for improved respirometry performance.		6-10 µg

Chapter 2: A Human Brain Map of Mitochondrial Respiratory Capacity and Diversity

Introduction

There are two primary challenges to utilizing respirometry for large human cohorts: (1) the immediate processing required for respirometry, and (2) that the current methodologies are low throughput with limited scalability. The RIFS assay described in Chapter 1 of this thesis, overcomes this first hurdle, allowing for sample material to be frozen down and bio-banked for later respirometry assessment. This still leaves the field with a methodological challenge where to run these large cohorts effectively, we need new techniques to more efficiently process and analyze large respirometry sample sets. In a traditional respirometry experiment, an operator would typically normalize each sample to protein quantity individually, load each sample individually, and then analyze each Seahorse trace individually. While these techniques are suitable for tens of samples, they are incredibly cumbersome for hundreds of samples.

While in theory we knew that the RIFS assay would make large-scale respirometry studies feasible, finding the appropriate research question and sample set to answer it would be challenging. With this in mind, we identified the human brain as a tissue which would benefit from a wider assessment of mitochondria. The brain is largely studied in the context of white matter and grey matter; these two types of matter are typically taken from various brain regions and mixed together to make a large sample pool for experiments and analysis. But what data are we potentially losing out on by mixing together brain regions? Is there mitochondrial diversity in the brain separate from just the type of brain matter? Is there diversity within parts of the same brain region?

In a multi-institutional study led by Dr. Eugene Mosharov and Dr. Martin Picard, we set out to make a human brain map of mitochondrial respiratory capacity and diversity (Mosharov et al. 2024). Using a neurotypical human brain, we divided one 3mm of one hemisphere into 703 voxels/cubes of $3mm^3$. This data set represents the largest known study including mitochondrial

respirometry (in this case in the form of RIFS) and through measuring respirometry in a resolution never before accomplished, we uncovered a foundation for exploring the immense diversity of mitochondrial phenotypes which exist within the brain. Chapter 2 of this thesis will discuss the novel findings we made in performing and analyzing this first-of-its-kind data set, and Chapter 3 of this thesis will discuss the novel methodologies developed to adapt the RIFS platform to a dataset of this size.

Main

Functional neuroimaging techniques capture dynamic electrical, metabolic and hemodynamic brain energy states (Castrillon et al. 2023; Cui et al. 2020; Pinotsis, Fridman, and Miller 2023; Strasser et al. 2020) but offer only indirect measures of the underlying subcellular bioenergetic processes. All basal and activity-dependent brain processes depend on cellular energy transformation, or bioenergetics, involving ATP synthesis by oxidative phosphorylation (OxPhos) within trillions of respiring mitochondria (Padamsey and Rochefort 2023). There are 100-1,000s of these organelles per neuron or glial cell (Pekkurnaz and Wang 2022). Mitochondria molecularly specialize to meet specific cellular demands, direct subcellular activities (Rosenberg et al. 2023; Fecher et al. 2019; Pekkurnaz and Wang 2022; Monzel, Enríquez, and Picard 2023; Rath et al. 2021), and provide the necessary energy to support brain activity. Beyond energetics, mitochondria also participate in other critical functions including cell-cell signaling (Picard and Shirihai 2022) and regulation of neuronal excitability(Styr et al. 2019), neurotransmitter release (Kwon et al. 2016) and modulation of inflammatory processes (Lin et al. 2022; Joshi et al. 2019). As a result, mitochondria must play a vital role in several supporting functions distributed across the brain's large-scale networks. Recent mechanistic studies underscore mitochondria's influence on cognition (Hara et al. 2014; Sharpley et al. 2012) and behaviors (Hollis et al. 2015; Gebara et al. 2021). However, mitochondria are typically examined at the sub-micron scale in cell biology, representing a major

methodological and conceptual scale gap with systems neuroscience, which operates at the scale of millimeters when the whole brain is imaged by magnetic resonance imaging (MRI) at conventional field strength. Therefore, a major knowledge obstacle keeping us from resolving the energetic forces that power and direct complex human brain dynamics is the spatial distribution of energy-transforming mitochondria across brain structures.

Preliminary work has begun bridging neuroimaging with microscopic anatomy, providing breakthroughs for cellular imaging interpretation of human neuroimaging findings (Amunts et al. 2013; Howard et al. 2023; Alkemade et al. 2022). Such advances aspire to inform our understanding of brain development, cognition, mood, and the mechanisms underlying various neuropathologies. To connect cognitive neuroscience and cell biology, here we develop a method to physically voxelize frozen human brain tissue, systematically profile mitochondrial molecular and biochemical diversity across a coronal brain section, and provide an algorithm for predicting mitochondria distribution, density and OxPhos capacity based on MRI data.

Brain Voxelization

To systematically map mitochondrial distribution, diversity, and molecular specialization across the human brain, the first challenge is to physically partition frozen brain tissue at a spatial resolution comparable to MRI. This would enable mapping molecular/biochemical profiles into standard neuroimaging stereotaxic space (Fig. 1a-g).

To address this challenge, we selected a postmortem neurotypical brain (male, 54 years old) with short postmortem interval (PMI = 8 hours, storage at −80°C for 10 years), with negative toxicology for psychoactive medication, drugs and alcohol, negative neuropathology, and negative history of neuropsychiatric disorder (see Methods). A coronal slab of the whole right hemisphere, including cortical and subcortical anatomical structures, was voxelized while maintained frozen at −25°C to preserve enzyme activities and molecular integrity during processing. To physically partition the frozen brain slab at 3 mm isotropic resolution comparable

to MRI, we programmed a computer numerical control (CNC) cutter to engrave a 3×3 mm square grid at 3 mm depth, followed by manual collection and indexing of a total of 703 samples (Extended Data Fig. 1&2, Supplementary Video 1).

Mitochondrial Phenotyping of Brain Voxels

To perform mitochondrial phenotyping at unprecedented scale on hundreds of physical human brain voxels, each sample was first randomly assigned to a well across 96-well plates (later deconvolved using a custom algorithm, Extended Data Fig. 3 and *Methods*), weighed, homogenized and subjected to quality control and basic characterization of total protein concentration and nuclear DNA content. These parameters demonstrated relatively uniform quality across the brain section (Fig. 1h-j). The average voxel weight was 26.2±4.5 mg (mean±SD; predicted weight = 27 mg from 3×3×3 mm voxel dimensions at aqueous volumetric density). Such small tissue samples require high-sensitivity assays for both mitochondrial density and enzymatic activities of the respiratory chain (also known as the electron transport chain, ETC)[5]. Mitochondrial density was assessed using a combination of two mitochondrial markers: citrate synthase (CS) activity and mitochondrial DNA (mtDNA) density. OxPhos enzymes reflecting energy transformation capacity were indexed using three markers: complex I (NADH-ubiquinone oxidoreductase), complex II (succinate dehydrogenase, SDH) and complex IV (cytochrome *c* oxidase, COX) which transport electrons and generate the life-giving transmembrane potential that ultimately powers ATP synthesis by the OxPhos system (Picard and Shirihai 2022).

For robustness, OxPhos enzymatic activities were quantified using two independent assays in different laboratories: a miniaturized colorimetric assay optimized for brain tissue (Rosenberg et al. 2023) and frozen-tissue respirometry (Osto et al. 2020; Acin-Perez et al. 2020) (Extended Data Fig. 3). To increase technical accuracy across the dataset, standard reference samples from the occipital lobe of the same brain (grey matter (GM), white matter

(WM), and voxels of mixed (M) grey/white composition) spanning the spectrum of possible activities were assayed in duplicate within each batch (eight 96-well assay plates) and used to correct for potential batch effects. The result is a uniform MRI-resolution dataset of mitochondrial activity profiles across the entire coronal section of the human brain (Extended Data Fig. 4). We excluded voxels with either too little tissue (samples located at the brain section's edges) or enzymatic activities below the detection limit (mainly from the WM), resulting in ~10% of the voxels missing at least one measure. All mitochondrial features (CI, CII, CIV, CS and mtDNA) were determined in 633 voxels, requiring 27,820 individual samples analyzed by colorimetric, respirometry, biochemical and qPCR assays, including replicates, controls and standards (see Methods).

Maps of Brain Mitochondrial Density and OxPhos Capacity

Mitochondria specialize molecularly and functionally, exhibiting a wide range of energy transformation capacities (Monzel, Enríquez, and Picard 2023). To assess mitochondrial "quality" and functional specialization, we previously developed a simple linear formula where OxPhos activities are divided by mitochondrial mass, yielding an index of OxPhos capacity on a per mitochondrion basis, known as the mitochondrial health index (MHI (Picard et al. 2018)). Here, with a substantially larger brain mitochondrial biochemistry dataset at hand, we discovered that the distributions of individual mitochondrial metrics were left-skewed (Extended Data Fig. 5).

When spheroid organelles have normally distributed radii, metrics related to the spheroid's surface area follow a square-root normal distribution, whereas those related to spheroid's volume are cube-root normalized. A well-established example of such dependence is observed with dense core secretory vesicles in which a similarly left-skewed distribution of neurotransmitter content is normalized by a cube-root transformation(Finnegan et al. 1996). Although mitochondrial morphology is more complex than a sphere, volumetric transformation of

mitochondrial content ($CS^{1/3}$ and $mtDNA^{1/3}$) and OxPhos capacity ($CI^{1/2}$, $CII^{1/2}$, $CIV^{1/2}$) parameters adequately normalized the mitochondrial features (i.e., decreased CV, skewness, and K-S distance). This transformation also allowed us to deconvolve the normal distributions of mitochondrial features for both GM and WM voxels, yielding a final parametric dataset of individual mitochondrial features (Extended Data Fig. 5).

As expected, the transformed mitochondrial content markers were strongly correlated (Pearson's r^2=0.46, p<0.0001, Extended Data Fig. 6a), providing a basis to integrate $CS^{1/3}$ and $mtDNA^{1/3}$ as *MitoD*, representing mitochondria tissue density for each brain voxel (Fig. 2a-c,e; Extended Data Fig. 7a). Mitochondrial DNA copy number (mtDNAcn), which reflects the number of mtDNA genomes per cell nucleus, is also presented (Extended Data Fig. 7b) but is influenced by cellularity and therefore comparison between brain regions cannot be straightforward[5]. Activities of OxPhos enzymes measured by colorimetric and respirometry assays were also highly correlated (Extended Data Fig. 6b-d), and subsequently averaged to integrate them as a robust measure of tissue respiratory capacity (TRC, Fig. 2c,d), representing the *direct quantification of mitochondrial OxPhos capacity per mg of brain tissue*.

Reference GM voxels exhibited significantly lower values for all mitochondrial metrics than reference WM voxels, with intermediate values in voxels of mixed GM/WM composition (Fig. 2d-e, Extended Data Fig. 4, bar graphs on the left of each panel). This is in agreement with prior neuroimaging-based estimates of brain energy metabolism (Rosenberg et al. 2023; Fecher et al. 2019; Tomasi, Wang, and Volkow 2013; He et al. 2022; Yu et al. 2023; Blazey et al. 2019). The data distributions for reference GM and WM voxels exhibited no overlap, highlighting their divergence. As a result, the signal-to-noise ratio to detect differences between GM and WM areas was high, reflected in large effect sizes for all mitochondrial metrics (Hedges' g=3.5-10.7 for GM *vs.* WM). Compared to the protein and cellularity measures that were homogenously distributed across the section (Fig. 1i-j), the maps of mitochondrial features (Fig. 2d-e, Extended

Data Fig. 7) showed clear heterogeneity that overlapped with brain anatomy (Fig. 2a; Extended Data Fig. 1h,i).

To create a volumetric analogue of MHI that reflects tissue-specific specialization of mitochondria for OxPhos and energy transformation, we computed an additional metric that we labeled the *mitochondrial respiratory capacity (MRC)* by expressing each voxel's TRC relative to MitoD (MRC=TRC/MitoD) (Fig. 2c,f). If each mitochondrion across the brain section had the same OxPhos energy transformation capacity, then MRC should have similar values in all brain areas. Conversely, a difference in MRC would indicate the presence of mitochondria with different OxPhos capacity, or degrees of specialization for OxPhos (Picard et al. 2018). Our data establish a variation in MRC both between GM and WM reference samples, and across anatomical structures within the coronal section (Fig. 2f). Thus, beyond the expected variation in mitochondrial density between GM and WM, these results reveal the extent to which maximal respiratory capacity, on a per-mitochondrion basis, varies across the human brain.

Brain-area Specific Differences in Mitochondrial Features

We next registered the coordinates of each voxel to the standard Montreal Neurological Institute (MNI) space (https://www.bic.mni.mcgill.ca/ServicesAtlases/ICBM152NLin2009), the most widely used reference neuroanatomical space for MRI research. Each voxel was manually annotated as GM (n=325), WM (n=132), or mixed (n=176) by an anatomy expert (M.T.d.S.) and labeled with its stereotaxic location (Extended Data Fig. 8). Anatomical identity of the voxels was further confirmed by staining adjacent thin tissue sections for Nissl substance, labeling neurons and glia, and for neuronal nuclear marker NeuN labeling neurons only (Extended Data Fig. 1h,i).

Projecting all annotated voxels with the full set of mitochondrial parameters in a Uniform Manifold Approximation and Projection (UMAP) space produced clusters identified visually that map clearly onto gross voxel composition (GM and WM, Fig. 2g). Conversely, when UMAP

clusters were used to predict the origin of the voxels, they mapped GM and WM voxel locations with 64% and 83% accuracy, respectively (chance level = 51% [GM] and 21% [WM], Extended Data Fig. 9a). Furthermore, GM and WM voxels exhibited large differences in all mitochondrial features (g=1.8-2.6; Fig. 2h). Compared to the GM, the WM contained significantly less mitochondrial mass and total OxPhos capacity (MitoD and TRC), but WM voxels exhibited a disproportionally low TRC relative to MitoD. As a result, the MRC reflecting mitochondria specialization for energy transformation on a per-mitochondrion basis, was lowest in the WM voxels (Extended Data Fig. 9b). The difference between GM and WM voxels in all mitochondrial features was replicated in an independent sample from the right occipital lobe (Fig. 2d-f, bar graphs).

Further analysis focused on GM voxels resulted in four UMAP clusters with distinct mitochondrial activity profiles (Fig. 2i-k; Extended Data Fig. 9c). Notably, we observed that despite having similar MitoD (Fig. 2l,m), compared to subcortical brain regions, cortical GM areas exhibited higher TRC ($p<0.01$, t-test; g=1.1) and MRC ($p<0.01$; g=1.4). An intriguing exception is the putamen, a subcortical structure with the highest TRC and MitoD. This could be attributed to the high density of terminal synapses/neurites and axonal projections in this area (Haber 1986), including large axonal arbors from the tonically active substantia nigra pars compacta dopaminergic neurons (Bolam and Pissadaki 2012), as well as the presence of numerous cell bodies indicated by the highest nDNA content in the putamen. With evolution, the putamen has undergone an evolutionary exaptation that may also account for this difference (Grillner and Robertson 2016). Conversely, we find high cell density and low MRC in the internal and external pallidum, as well as among several WM regions.

In comparative anatomy, the presence or absence of structures across species allow for the phylogenic classification of major human brain structures (Darwin 1912; de Sousa et al. 2023; Friedrich et al. 2021; Pandya, Petrides, and Cipolloni 2015). The brainstem, pallidal, and

striatal areas are uniformly acknowledged as the oldest, while cortical areas represent the most recent evolutionary development. Our results show that both TRC and MRC correlated strongly with the estimated phylogenic age of brain regions. Mitochondria in regions that emerged later in the evolutionary timeline – moving from reptilian to mammalian and further to primates and humans – exhibited higher MRC (rho=0.72-0.75, p>0.01; Fig. 2n). This enzymatic specialization aligns with the hypothesis that an evolutionary gradient exists with an increased metabolic demand (Castrillon et al. 2023). Our data show that this demand is met by a specialized mitochondrial phenotype with high OxPhos capacity per mitochondrion.

Brain Regions and Cell-type Specific Mitochondrial Phenotypes

Specialized mitochondrial phenotypes (i.e., mitotypes) map either to specific brain areas (Rosenberg et al. 2023) or to specific cell types (Fecher et al. 2019; Düking et al. 2022), which differ in their abundance among different brain areas (WM *vs*. GM; cortical *vs*. subcortical). To profile cell-type specific molecular mitochondrial phenotypes across the human brain, we performed single-nucleus RNA sequencing (snRNAseq) on individual nuclei recovered from voxel homogenates prepared for mitochondrial enzymatic measurements presented above. The lysis-oriented chemistry and aggressive mechanical disruption required for mitochondrial enzyme assays contrast with the gentler approaches typically required to generate high-quality preparations for snRNAseq (Slyper et al. 2020), a noteworthy limitation of our approach that should be corrected in future studies seeking to establish cell-type specific mitochondrial phenotypes.

We selected individual voxels from four areas: the middle temporal gyrus (MTg), hippocampus (Hipp), putamen (Put), and corpus callosum (white matter, WM), thereby covering a spectrum of brain areas with wide differences in cell type composition. Histochemical staining of neurons and glia (Nissl) or neurons only (NeuN) on 50 µm-thick brain sections confirmed the expected cellular identity of each voxel (Fig. 3a, Extended Data Fig. 10). After applying stringent

data cleaning and quality control thresholds, we computationally recovered a total of 32,515 nuclei (MTg: 8,945; Hipp: 7,044; Put: 6,176; WM: 10,350) categorized into 9 broad cell types (Fig. 3b), confirming the expected differences in cell composition across each stereotactically-defined voxel (Fig. 3c).

Mitochondrial specialization arises from the regulated expression of ~1,136 validated mitochondrial genes/proteins from MitoCarta3.0 (Rath et al. 2021). Using pseudo-bulk transcriptomes (i.e. mimicking bulk RNAseq), we recovered 1,118 nuclear-encoded mitochondrial genes (not mtDNA) and calculated OxPhos scores for each voxel and OxPhos subunit[5]. As in our molecular and biochemical results, the WM voxel exhibited lower mtDNA-encoded genes than GM voxels (Fig 3d; logFC < −1.5, adjusted $p<0.001$). Overall, relative gene expression of OxPhos complex subunits corresponded well with measured enzymatic activities of CI, II and IV in all brain regions (Fig 3d), providing convergent evidence for the observed enzymatic data. One exception was a lower expression of Complex I and II subunits in the cortex that was not reflected in the activity measures. The putamen had the highest scores for both OxPhos expression and enzyme activity, despite the low abundance of recovered neurons, suggesting that either i) the recovered nuclei do not faithfully represent cell types present in the brain areas, or ii) there are region-specific drivers of enzymatic mitochondrial phenotypes independent of cell type composition, such as local activity or functional connectivity patterns.

To investigate how different cell types may underlie mitochondrial phenotypes by brain region, we compared mRNA abundance of two OxPhos complexes (Complex I and IV) for matching cell types in each of the four voxels. The raw transcriptional profiles of OxPhos complexes clustered by voxel rather than cell type (Fig. 3e, Supplementary File 1), indicating that the major driver of the differences in OxPhos transcriptome for each cell type is the brain region in which it resides. We then extended this analysis to 149 mitochondrial pathways (MitoCarta3.0), composite multi-gene scores that de-emphasize the influence of individual

genes to create more stable estimates of functionally relevant mitotype specialization. Again, we found that transcriptional profiles were more similar between different cell types from the same brain region rather than between similar cell types from different regions (Fig. 3f). Thus, most of the variance in brain mitotypes is attributable to regional variations.

Interestingly, removing the voxel-to-voxel variation in the overall expression levels by z-scoring mRNA levels within each voxel rather than across the whole dataset revealed cell-type-specific mitotypes (Fig. 3g). For instance, relative to other cell types, inhibitory neurons had the lowest expression of OxPhos complexes, while endothelial cells showed the highest expression. Similar robust clustering by cell type rather than voxel location was observed when all mitochondrial gene expression profiles were normalized within each sample (Fig. 3h).

Overall, our single-nucleus transcriptome analyses indicated that while mitotype differences between human brain cell types exist and are conserved across the brain regions examined, global drivers of mitochondrial gene expression influencing all cell types across brain regions drive the most significant mitochondrial variation, consistent with a topological understanding of brain functional organization (Tavor et al. 2016; Margulies et al. 2016; Smith et al. 2009).

Associations of Brain Mitochondrial Phenotypes with Neuroimaging Modalities

We next asked whether mitochondrial phenotypes may be reflected in standard neuroimaging modalities, including T1 and T2, fMRI-BOLD, and diffusion-weighted imaging from hundreds of individuals (Extended Data Table 1, n = 1,870 multi-modal brain MRIs from healthy adults aged 18-35 years (Tsuchida et al. 2021)). Such correlations would allow us to use neuroimaging data to predict mitochondrial features, thereby extending the map of mitochondrial OxPhos capacity to the whole brain and to eventually use neuroimaging data to derive personalized MRI-based maps of mitochondrial phenotypes.

As described above, each voxel from our frontoparietal section was registered to its corresponding resolution-matched voxel in the standard MNI brain atlas. Accurate mapping of each voxel was manually verified. Samples with a sum of GM and WM probabilities less than 70% were discarded to avoid partial volume effect contamination. The remaining 539 voxels with all mitochondrial features measured and correctly mapped into the stereotaxic space were randomly divided into two groups to train the model (80%, or 431 of voxels) and to test the model (20%, 108 voxels) (Extended Data Fig. 11a). Each mitochondrial feature (CI, CII, CIV MitoD, TRC and MRC) was regressed onto 22 structural, functional, and diffusion-based neuroimaging metrics using a stepwise linear regression model (Hocking 1976). Some parameters, such as the orientation dispersion (OD) index, a proxy for neurite complexity (Zhang et al. 2012), correlated positively with all mitochondrial metrics (Extended Data Table 1). On the other hand, some MRI metrics did not correlate with mitochondrial OxPhos, while others correlated differently with specific features with either a positive or negative linear regression weights (Extended data table 1).

Using linear equations from the regression model, the prediction accuracy of mitochondrial features in out-of-sample voxels (20% of samples) based solely on MRI metrics ranged between r^2=0.26-0.36 (all $p<0.0001$, Fig. 4a). In comparison, prediction of the null model with scrambled voxels returned accuracies less than 0.1% ($p>0.7$, Extended Data Fig. 11c). Collapsing the test samples into their respective brain regions, the observed-to-expected correlations were 2-3 times stronger, emphasizing the robust regional variation in mitochondrial phenotypes (Fig. 4b). The out-of-sample accuracy of the model was also tested by using the MRI-based model to predict the mitochondrial markers in the occipital lobe from the same donor brain (not used in the prediction model). When compared across the six mitochondrial features, the model yielded significant agreement between observed and predicted values ($r=0.75$, Fig. 4h). The predicted and observed mitochondrial feature maps, projected on the coronal slice

examined biochemically, showed remarkable similarities (Extended Data Fig. 11d), lending additional support to the model.

Encouraged by the ability of the model to predict out-of-sample mitochondria characteristics based on MRI features, we next expanded it to calculate mitochondria density and OxPhos activities at the scale of the whole brain. The resulting cortical and WM tracks maps revealed regional specialization for all mitochondrial features (n= 1,827,243 voxels at $1mm^3$ resolution; Fig. 4c-e). Mitochondrial specialization is particularly large for MRC and the OxPhos enzymes, and comparatively more modest for the mitochondrial content (MitoD), suggesting that different brain areas are expected to vary less in their mitochondrial content and substantially more in their mitochondrial specialization for ATP synthesis (i.e. MRC). Accordingly, our neuroimaging-based estimates of MRC across the brain showed a significant correlation with maps estimating brain evolution: evolutionary expansion (J. Hill et al. 2010) and evolutionary variability (Croxson et al. 2018) (Extended Data Fig. 12), consistent with the region-based analysis shown in Fig. 2n.

Finally, we generated a UMAP representation of the predicted brain-wide mitochondrial phenotypes (anatomical annotation confidence >80%), which further confirmed the striking contrast between GM and WM regions across all mitochondrial features (Fig. 4f,g). Again, the magnitude of gradients was especially large for CI-IV activities and MRC, reflecting the predicted regional specialization of mitochondria. Furthermore, the multivariate UMAP space mapped relatively well with the anatomical/stereotaxis coordinates of cortical and subcortical GM regions and WM tracts, including regions not presented in our initial brain section. Thus, these results establish an approach to use standard MRI parameters to predict biochemical and molecular mitochondrial profiles across the human brain.

Discussion

We have generated an atlas of mitochondrial content, enzymatic OxPhos activities, and specialization across the human brain, establishing the diversity of mitochondrial phenotypes at a resolution comparable to MRI. Enabled by a novel approach to physically voxelize frozen human brain tissue, our results reveal roles for both regional and cell type-level factors that contribute to molecular mitochondrial phenotype diversity observed throughout the human brain. Notably, the distinct mitochondrial phenotypes between the grey and white matter align with well-known regional variation in metabolic requirements across brain tissue (Rosenberg et al. 2023; Fecher et al. 2019; Tomasi, Wang, and Volkow 2013; He et al. 2022; Yu et al. 2023; Blazey et al. 2019; Castrillon et al. 2023; Cui et al. 2020; Pinotsis, Fridman, and Miller 2023; Strasser et al. 2020). This also may highlight a predisposition for mitochondrial disorders to impact cortical structures, such as stroke-like episodes that selectively affect and spread across cortical areas with a topology not restricted to arterial vascular territories (Cheng, Zhang, and He 2022). These data could also suggest the existence of compensatory mechanisms within the white matter that may mitigate cortical deficits in diseases like stroke(Forkel et al. 2014; Umarova et al. 2017).

The alignment of mitochondria molecularly specialized for energy transformation (high MRC) with evolutionary patterns sheds light on the underlying subcellular bioenergetic infrastructure evolved to sustain the elevated energy costs unique to humans (Pontzer et al. 2016), particularly in regions associated with human-specific cognitive functions (Castrillon et al. 2023). Recent work highlights how cortical brain regions recruited to perform executive functions express high levels of cell surface receptors for neuromodulators, and depend highly on glucose consumption(Castrillon et al. 2023). This dependence also agrees with the neuropsychological vulnerability of evolutionary advanced cognitive functions among individuals with inherited mitochondrial diseases (Moore et al. 2020), and with the cognitive domains

affected by the age-related accumulation of defects on the mitochondrial genome (Klein et al. 2021; Bose and Beal 2016; Borsche et al. 2021).

Rapidly accumulating evidence that neuropsychiatric and age-related brain disorders involve mitochondrial alterations has motivated basic and clinical research communities to image mitochondrial biology in the living brain. In parallel with PET-based metabolic imaging, our model predicting molecular mitochondrial phenotypes across the brain using common neuroimaging modalities (Tsuchida et al. 2021; Van Essen et al. 2013) meets this need and opens the door to exciting questions bridging the scale gap between cognitive neuroscience and mitochondrial biology.

However, some limitations of the present study should be noted. Our prediction model is based on neuroimaging data from a group template and is subject to interindividual anatomical variability. The reliance on a single neurotypical human brain sample, akin to other whole-brain microscopic initiatives (Amunts et al. 2013; Howard et al. 2023; Alkemade et al. 2022), underscores the necessity for additional postmortem data sets to capture the full spectrum of mitochondrial expression diversity across individuals of different sex and across a wide age span. The scale of this task promises to be technically challenging. Nevertheless, mapping inter-individual differences in the sub-cellular energetic architecture – in specific cell types, among different brain regions – appears crucial to advance our understanding of the energetic infrastructure that supports and possibly instructs large-scale brain dynamics in different brains (Gordon et al. 2017).

In sum, our physical voxelization approach and molecular phenotyping study establishes the spatial distribution of mitochondrial diversity within the human brain, revealing robust disparities between grey and white matter and among key cerebral regions. This work not only unveils a gradient that parallels the brain's phylogenetic development but also provides a scalable approach to deciphering the mitochondrial underpinnings of human brain evolution,

development, and disease. Bridging the scale gap from organelle to whole-brain biology and neuroimaging lays the foundation to understand the mitochondrial basis of brain function and dysfunction across a variety of contexts.

Methods

Donor Brain Selection

Donor brains were collected, evaluated, and stored by the Macedonian / NYSPI Brain collection and made available for this study through the Quantitative Brain Biology (Brain QUANT) Institute at New York State Psychiatric Institute (NYSPI). The study was reviewed and approved by the Institutional Review Board at NYSPI. The selected brain was from a 54-year-old neurotypical male who died from a myocardial infarction (PMI = 8 hours, storage time at −80°C for 10 years), had negative toxicology for psychoactive medication, drugs and alcohol, essentially negative neuropathology, and negative history for neuropsychiatric disorders, according to a validated psychological autopsy designed to obtain psychiatric diagnoses by interview of next of kin (Kelly and Mann 1996). According to his relatives, the donor was right-handed, athletic, and did not smoke or drink alcohol. Coronal 2cm-thick slabs of the right hemisphere were flash-frozen in 1,1,1,2-tetrafluoroethane (R-134a, TGS, Skopje, Macedonia) and stored at −80°C. For sectioning, we chose a slab located at stereotactic Montreal Neurological Institute (MNI) coordinates 15.51 mm posterior of the center of the anterior commissure (AC), according to the Human Brain Atlas (Mai, Majtanik, and Paxinos 2015).

Tissue Voxelization and Sample collection

To perform brain partitioning while maintaining the tissue below −20°C to ensure that enzymatic activities are least affected, we developed a novel hardware/software platform. The hardware consisted of a CNC (computer numerical control) router (FoxAlien CNC Router 3018-SE V2) operated in a −25°C freezer room and controlled by a laptop computer in the adjacent +4°C room. A software routine in Igor Pro (WaveMetrics, Inc., OR) was developed to 1) easily

define the parameters to clean and partition a frozen brain slab, 2) generate a G-codes used to control the CNC router, 3) randomize samples and assign them to assay plates, and 4) derandomize the samples after the assays are complete (Supplementary Files 2&3).

Using an occipital lobe slab from the selected brain, sectioning parameters (drill diameter, feed rate, spindle speed, etc.) were optimized to minimize cutting time while avoiding potential tissue damage due to local heating and maintaining reliable operation during the several hours required for brain cutting. See Extended Data Fig. 1a-c for details on the milling procedure. Once the surface of the brain slab was fully milled, it was placed on dry ice. First, four samples of shavings were collected from the surface above one white (SLF) and three gray (putamen, SFg and MFg) areas. These 'dust' samples were processed and quantified together with all other samples. As shown on Extended Data Fig. 2, mitochondrial activities are noticeably affected by local heating and exposure to air.

Next, shavings were gently removed from the surface with a brush and a pre-chilled scalpel and forceps were used to collect individual voxels. The scalpel was inserted into the milled cuts applying light pressure, which released the voxels from the surface of the slab without causing them to pop out. Voxels (703 in total) were then individually picked up with forceps and placed into pre-labeled and pre-weighed 0.5ml PCR tubes on dry ice. Tubes were then re-weighed to determine the weight of the tissue, transferred to 1.5 ml tubes, and stored at −80°C until future processing. To minimize potential batch effects and to blind the experimenter to the origin of the voxel, samples were scrambled using an Igor Pro routine: unique coordinates of each sample on the brain map were substituted with new, randomly generated coordinates on eight 96-well assay plates.

Brain Histology

After voxel collection, 0.3 mm of the surface was cleaned/leveled again with a 12.7 mm flat-tip drill bit (Extended Data Fig. 1d-f). The metal plate with the slab was then mounted on a

freezing microtome and 50 µm-thick cryosections were collected onto glass slides for histological evaluation. For anatomical mapping of neurons and glia, and alignment of cell populations with the collected voxels, we performed tissue staining for neuronal nuclear marker (NeuN), and Nissl as previously described (Boldrini et al. 2019) with some modifications to adapt the immunostaining to frozen tissue.

In brief, for NeuN immunohistochemistry (IHC), whole hemisphere frozen sections mounted on glass slides were dried at room temperature for 1h, then fixed in 4% paraformaldehyde in phosphate buffer (PB; 0.1M; pH 7.4) for 3h at 4°C. After 3 washes in PBS at RT, sections were incubated in 3% H_2O_2 and 10% methanol in PBS for 10 minutes, followed by 3 washes in PBS. After 1h pre-incubation in blocking buffer (10% normal horse serum, 0.3% Triton X-100 in PBS), sections were incubated with mouse monoclonal antibodies against NeuN protein (Anti-NeuN, clone A60; 1:20K dilution; Millipore, St. Louis, MO, USA) overnight at 4°C. Sections were then washed 3 times in PBS and incubated with secondary biotinylated horse antibodies against anti-mouse IgG (1:200 dilution; Vector, Newark, CA), followed by avidin/biotinylated peroxidase complex (Vectastain ABC kit elite, Vector) for 2h at RT (1:100 Avidin,1:100 Biotin in PBS) and then 5 min in 0.05% diaminobenzidine (DAB) in 0.1M NaAc.

For Nissl stain with Cresyl violet, after NeuN immunostaining sections were dried in a desiccator overnight followed by delipidation in inceasing percentages of ethanol to 100%, followed by 100% xylene. Then, sections were rehydrated starting from xylene and ending in H_2O, and stained in Cresyl Violet (0.1% Cresyl violet Acetate, 0.25% glacial Acetic Acid in H_2O). The staining was differentiated in 90% EtOH + 10% glacial acetic acid. Finally, sections were placed in 100% EtOH followed by 100% xylene before coverslipping.

Sample Preparation for Mitochondrial Assays and snRNAseq

Homogenization buffer (1mM EDTA and 50mM Triethanolamine) was added to each sample at 1:50 (g:ml) ratio. Homogenization was performed with 2 tungsten beads using a

Tissue Lyser (Qiagen, cat# 85300) run at 30 cycles/sec. Samples were homogenized for 1 minute, then incubated on ice for 5 min followed by another 1-min cycle of homogenization. The beads were then removed, and samples underwent 3 freeze/thaw cycles, which was determined to result in higher mitochondrial activities. Samples were placed at −80°C for 15 minutes, then transferred to a RT water bath for 4 min. Homogenate from each sample before the freeze/thaw cycles (100-200µl) was collected for snRNAseq analysis. Protein concentration was measured in 15µL of each sample using the Pierce BCA Assay Kit (Thermo 23225) per manufacturer instructions. Absorbance at 562nm was measured on Tecan Spark plate reader. Sample protein concentration was determined based on the linear regression of an 8-point BCA standard curve (0-20µg) on a plate-by-plate basis. Samples were stored at −80°C.

Colorimetric Assays of Mitochondrial Enzyme Activities

Enzymatic activities were quantified as previously described[5] with several modifications. Briefly, activities of Citrate Synthase (CS), Complex I, Succinate Dehydrogenase (SDH/ complex II), Cytochrome C Oxidase (COX/ complex IV) were measured spectrophotometrically in 96-well plates using Spectramax M2 (Spectramax Pro 6, Molecular Devices). Linear slopes reflecting changes in absorbance of the reporter dyes were exported to Microsoft Excel and converted into enzymatic activities using the molar extinction coefficient and dilution factor for each assay. The assays were optimized for the amount of homogenate and substrates to produce stable readings across all samples. Three *loading control* samples - grey matter (GM), white matter (WM), and mixed tissue from the occipital lobe slab of the same brain - were run in duplicates on each plate to ensure that controls would be identical between plates run on different days. Thirty voxels of each tissue type were homogenized and pooled to produce technical replicates of the same samples.

Each sample was assayed in three technical replicates (assayed on different plates) plus the same number of negative controls, except CIV that requires only one nonspecific activity

measure. Overall, 8 plates * 4 assays * (3 replicas + 2.5 negative controls) = 176 plates were analyzed by colorimetric assays. Samples were thawed in a room temperature water bath for 4 minutes on the morning of the assays. On each day, 90 samples plus 6 (duplicates of the three) loading controls were transferred into a 96-deepwell block. A 96-multichannel pipette (VIAFLO 96 # 6001) was used to load samples from the block into each of the 96-well triplicate plates and triplicate nonspecific activity plates for each assay. 10 µl of homogenate was used to measure activity for each of the enzymes. Plates were stored at 4°C before the assay. Each day, 22 plates were processed: 6 plates for 3 assays and 4 for the CIV assay.

Citrate synthase (CS) enzymatic activity was determined by measuring the increase in absorbance of 5,5'-dithio-bis-(2-nitrobenzoic acid) (DTNB) at 412nm at 30°C in 200µL of a reaction buffer containing: 200 mM Tris (pH 7.4), 10 mM acetyl-CoA, 10 mM DTNB, 2 mM oxaloacetic acid, and 10% w/v Triton-x-100. The rate of conversion of DTNB into NTB^{2-} ions indicates the CS enzymatic activity. To measure non-specific activity, oxaloacetate was removed from the assay mix.

Complex I (CI) activity was determined by measuring a decrease in the absorbance of 2,6-dichloroindophenol (DCIP). Kinetics of changes in DCIP absorbance was measured at 600nm at 30°C in 200 µl of a reaction buffer containing: 50 mM potassium phosphate (pH 7.4), 50 mg/ml bovine serum albumin (BSA), 20 mM decylubiquinone, 80 mM nicotinamide adenine dinucleotide (NADH), 20 mM DCIP, 400 µM antimycin A, 50 mM potassium cyanide (KCN). Antimycin A and KCN were used to inhibit electron flow through complexes III and IV. The negative control included CI inhibitors rotenone (500 µM) and piericidin A (200 µM).

Complex II (CII, Succinate Dehydrogenase [SDH]) activity was determined by measuring the decrease in absorbance of DCIP at 600 nm at 30°C in 200 µl of a reaction buffer containing: 50 mM potassium phosphate (pH 7.4), 50mg/mL BSA, 500 µM rotenone, 500 mM succinate-tris,

50 mM KCN, 20 mM decylubiquinone, 20 mM DCIP, 50 mM ATP, 400 µM antimycin A. The negative control included 500 mM sodium-malonate, which inhibits CII.

Complex IV (CIV, Cytochrome c oxidase [COX]) activity was determined by measuring a decrease in cytochrome C absorbance. The rate of conversion of cytochrome C from a reduced to oxidized state was measured at 550 nm at 30°C, in 200µL of reaction buffer containing: 100 mM potassium phosphate (pH 7.5), 10% w/v n-dodecylmaltoside and 120µM of purified reduced cytochrome C. The negative control omitted tissue homogenate to determine the auto-oxidation of reduced cytochrome C.

For each assay, activity was determined by integrating the OD change over a certain time period and then subtracting the non-specific activity. As some samples had very different OD kinetics, two separate integration times were used for each assay which ensured that samples that had a delayed start or samples that saturated quickly were all accounted for. CS activity was determined by integrating OD412 change over both 150-250 seconds and 250-500 seconds and by subtracting the non-specific activity. CI activity was determined by integrating OD600 change over 50-300 seconds and 300-600 seconds, and by subtracting the rate of NADH oxidation in the presence of rotenone and piericidin A from the total decrease in absorbance. CII activity was determined integrating OD600 change over 100-400 seconds and 400-700 seconds, and by subtracting the absorbance in the presence of malonate from the total decrease in absorbance. CIV activity was determined by integrating OD550 change over 50-150 seconds and 150-300 seconds, and by subtracting the non-specific activity from the total decrease in absorbance.

For each assay, the later integration time resulted in more consistent measures for control activities across all plates. Therefore, the activities of the control duplicate samples on each plate were averaged for each of the three controls. Each individual control value was then divided by its duplicate average to determine a correction factor. Correction factors for the

duplicate control samples on each plate were then averaged. The average normalization factor across the three controls was then used to normalize the plates. Both the earlier integration time values and the later integration time values from each sample were then multiplied by the final normalization factor per plate. Non-specific activity plates were integrated over the full range of the two integration times for each assay (150-500 CS, 50-600 CI, 100-700 CII, 50-300 CIV).

Once plates were normalized, each sample had values for both the earlier integration time and the later integration time on all three triplicate plates. The higher value between the two integration times was selected for each plate. Of the three selected values (one from each triplicate plate), the two closest values were selected, and the least similar value was discarded. This resulted in duplicate activity measures for each sample. Mitochondrial enzymatic activities were determined by averaging the duplicates, and the specific activity of each sample was calculated as the total activity minus non-specific activity (negative control). Non-specific activity was also calculated by taking the two closest of three measures, except for CIV which only has one non-specific activity plate. For CIV the average non-specific activity value from each plate was applied to all samples on the plate.

Respirometry assays

Complexes I, II and IV

The basic protocol optimized for previously frozen tissue samples was used as previously described(Osto et al. 2020; Acin-Perez et al. 2020). In short, the brain homogenate samples were loaded in duplicate onto XF96 Seahorse plates to measure the maximal oxidative capacity of either ETC Complexes I and IV or Complexes II and IV on a Seahorse XFe96 instrument. Complex I and IV are measured by sequential injection of NADH, Antimycin A, TMPD/Ascorbate, and Azide, while Complex II and IV are measured by injecting Succinate/Rotenone, Antimycin A, TMPD/Ascorbate, and Azide.

Investigators running respirometry assays were blinded to the sample identity until all processing and analysis of the results were complete. Each Seahorse assay plate had 8 control wells: the GM, WM and mixed tissue controls that were identical to those used for colorimetric assays, mouse liver mitochondrion (a control for Seahorse and injection function), and a blank control. Samples were loaded at 15uL volume and normalized to protein concentration after data acquisition.

Respirometry Data Analysis was performed as previously described[32]. Briefly, oxygen consumption rate (OCR) data were extracted from duplicate Seahorse runs using the Agilent Wave Analysis software. Complex I OCR was calculated as the post-NADH injection OCR minus the post-Antimycin A injection OCR. Complex II OCR: post-succinate/rotenone injection OCR minus the post-antimycin A injection OCR. Complex IV OCR: post-TMPD/ascorbate injection OCR minus the post-azide injection OCR.

After values for Complex I-IV OCR were normalization for protein concentration, traces were analyzed for acceptance criteria. Minimal OCR thresholds (<2SD of the average readings from WM samples) were set to 0.5 pmol/min/µg for Complexes I and II, and 1.5 pmol/min/µg for Complex IV. If a sample had Complex I or II OCR readings that passed their acceptance criteria, Complex IV OCR values must exceed 80% of their respective Complex I OCR or Complex II OCR reading. Overall, one Complex I OCR value, one Complex II OCR value, and two Complex IV OCR values must pass all acceptance criteria. If a sample did not meet the criteria, the assays were rerun with 25µL sample instead of 15µL for the initial run. If a sample did not meet the acceptance criteria after the rerun, the data was not included in the final data set. Overall, out of 703 analyzed samples, 70 samples did not pass acceptance criteria for Complex I activity, 35 for Complex II activity, and 19 for Complex IV activity.

Mitochondrial and nuclear DNA (mtDNA and nDNA)

mtDNA and nDNA densities as well as mtDNA copy number (mtDNAcn) were measured as previously described[5] with minor modifications. Homogenates were lysed at 1:10 dilution in a lysis buffer (100 mM Tris HCl pH 8.5, 0.5% Tween 20, and 200 g/mL proteinase K) for 16 hours at 55°C, 10 minutes at 95°C, and then briefly at 4°C. Plates were then stored at −80°C and thawed to 4°C before performing qPCR. The reactions were run in triplicates in 384-well plates using a liquid handling station (ep-Motion5073, Eppendorf), with 12 µl of master mix (TaqMan Universal Master mix fast, Life Technologies #4444964) and 8 µl of the sample lysate, for a final volume of 20 µl. Each plate contained 90 samples, duplicates of the three loading control samples, a negative control (lysis buffer without homogenate), and 8 serial dilutions of HfB1 standard (1:4 dilutions), all of which were measured in triplicates. qPCR reaction with Taqman chemistry was used to simultaneously quantify mitochondrial and nuclear amplicons in the same reactions: ND1 (mtDNA) and β-2 microglobulin (B2M, nDNA). The Master Mix included 300 nM of primers and 100 nM probe: ND1 forward primer: GAGCGATGGTGAGAGCTAAGGT, reverse primer: CCCTAAAACCCGCCACATCT, and the probe: HEX-CCATCACCCTCTACATCACCGCCC-3IABkFQ. The B2M forward primer: CCAGCAGAGAATGGAAAGTCAA, reverse primer: TCTCTCTCCATTCTTCAGTAAGTCAACT, and the probe: FAM-ATGTGTCTGGGTTTCATCCATCCGACA-3IABkFQ.

The plates were sealed, briefly centrifuged at 2,000g, and subjected to 40x cycles on a QuantStudio 7 flex instrument (Applied Biosystems Cat# 448570): 50°C for 2min, 95°C for 20s, 95°C for 1min, and 60°C for 20s. To ensure comparable Ct values across plates and assays, thresholds for fluorescence detection for both ND1 and B2M were set to 0.08. Averages, standard deviations, and coefficients of variation (CV) were computed between qPCR triplicates and an exclusion cutoff of Ct>33 was applied. Control Ct values were averaged across all plates for each of the three controls, and each plates' control values were then divided by the average to determine a normalization factor. The average normalization factor across the three controls

was then used to normalize each plate. mtDNAcn was derived from the ΔCt calculated by subtracting the average mtDNA Ct from the average nDNA Ct and mtDNAcn was calculated by $2^{(\Delta Ct)}\times 2$. For measures of mtDNA density, the Ct value was linearized as $2^{Ct}/(1/10^{-12})$ to derive relative mtDNA abundance per unit of tissue.

MitoTracker Deep Red (MTDR) staining

Measurement of mitochondrial content in previously frozen sample homogenates using MTDR was performed as outlined in Refs: (Osto et al. 2020; Acin-Perez et al. 2020). Briefly, 2.5-80 µg of sample material (based on BCA protein calculations) was loaded to a clear, flat-bottom 96-well plate together with 100µL of MAS buffer containing 1µM MTDR. After 10min incubation at 37°C, MTDR was removed by centrifuging the plate for 5 min at 2000 x g at 4°C, with no brake for deceleration. The supernatant was carefully removed, and samples resuspended in 100µL of MAS buffer without MTDR. Fluorescence was measured using a Tecan Spark plate reader using 625 nm excitation and 670 nm emission. Relative mitochondrial content was determined after controlling for background fluorescence using a blank well. Note that because of high variability in MTDR assay values it correlated poorly with CS and mtDNA (Extended Data Fig. 6a) and was not used for the analysis.

Overall number of samples

The following biochemical assays were performed to analyze 703 voxels (including replicates and controls): BCA (8 x 96-well plates, 768 samples), MTDR (8 plates, 768 samples), CI, CII and CS colorimetry (48 plates, 13,608 samples), CIV colorimetry (32 plates, 3024 samples), CI, CII and CIV respirometry (44 plates, 7,384 samples), and mtDNA/nDNA (24 plates, 2268 samples). Overall, 164 x 96-well plates (some not fully loaded) and 27,820 individual readouts, including replicates and controls were analyzed. Of the 703 original samples, 633 voxels had all mitochondrial features (CI, CII, CIV, CS and mtDNA) determined, of which 539 voxels mapped accurately into the MNI stereotaxic space.

Single nucleus RNA sequencing (snRNAseq)

Frozen cell homogenates from four human brain areas (cortex, hippocampus, putamen, and corpus callosum, Fig. 3a) were used for single nucleus RNA sequencing (snRNAseq). Briefly, samples in homogenization buffer (Clontech, Cat: 2313A), were thawed on ice, then centrifuged at 500 x g for 5 minutes at 4°C, washed with 4 ml ice-cold EZ prep buffer (Sigma, Cat: NUC-101) with 0.2% RNAse inhibitor and incubated on ice for 5 minutes. After centrifugation, the nuclei were washed in 4 ml Nuclei Suspension Buffer (NSB, 1x PBS, 0.01% BSA and 0.1% RNAse inhibitor). Isolated nuclei were resuspended in 100-500 µl NSB depending on pellet size and filtered through a 35 µm cell strainer (Corning, Cat: 352235). Nuclei were counted using the Nexcelom Cellometer Vision 10x objective and an Acridine Orange & Propidium Iodide (AO/PI) stain. 20 µl of the AO/PI was pipet mixed with 20 µl of the nuclei suspension and 20 µl was loaded onto a Cellometer cell counting chamber of standard thickness (Nexcelom, Cat: CHT4-SD100-002) and counted with the dilution factor set to 2.

The single-nuclei library preparation was constructed using 10x Chromium Next GEM Single Cell 3' Reagent Kits v3.1 (Dual Index) (10x Genomics, Pleasanton, CA) according to the manufacturer's protocol. Briefly, a total of ~10,000 nuclei were loaded on the 10x Genomics chromium controller single-cell instrument. Reverse transcription reagents, barcoded gel beads, and partitioning oil were mixed with the cells for generating single-cell gel beads in emulsions (GEM). After reverse transcription and barcoding of the cDNA, GEMs were broken, and pooled fractions were recovered and amplified via PCR. The amplified cDNA was then separated by SPRI size selection into cDNA fractions containing mRNA derived cDNA (>400bp), which were further purified by additional rounds of SPRI selection. GEX sequencing libraries were generated from the cDNA fractions, which were analyzed and quantified using TapeStation D5000 screening tapes (Agilent, Santa Clara, CA) and Qubit HS DNA quantification kit (Thermo Fisher Scientific). Libraries were pooled and sequenced together on a NovaSeq 6000 with S4

flow cell (Illumina, San Diego, CA) using paired-end, dual-index sequencing with 28 cycles for read 1, 10 cycles for i7 index, 10 cycles for i5 index, and 90 cycles for read 2. Samples from the four different brain regions were processed for snRNAseq on the same day to avoid batch effects.

The FASTQ files were processed using the 10x Genomics CellRanger package (v.6.0.0) with human reference data “GRCh38-2020-A” and a command line option “--include-introns”. Raw UMI count matrices were further processed using the Cellbender package (v.0.1.0) with command line options of 2,000 expected cells and 20,000 total droplets to remove debris and doublets. Cells with a range of 200-5000 genes, at least 500 counts, and less than 11% mitochondrial DNA genes were kept, and ribosomal genes were removed. The data was log-normalized, scaled, and doublets were removed using DoubletFinder (Fleming et al. 2023). The four datasets were integrated using Harmony (Korsunsky et al. 2019). Broad clusters were identified using the human motor cortex dataset from Azimuth (Bakken et al. 2021) and unspecific clusters were removed. Each dataset was down-sampled to 5000 nuclei per dataset for downstream mitochondrial analyses.

For mitochondrial analysis of the snRNAseq data, we first filtered for all human MitoCarta3.0-annotated mitochondrial genes (MitoCarta3.0,(Rath et al. 2021)). To calculate MitoPathway scores, we used the average expression of all mitochondrial genes of each respective pathway, as annotated in MitoCarta3.0, either for pseudobulk expression of each voxel, or each voxel and cell type. A detailed description of the data analysis can be found in a supplementary markdown file, linking each figure and analysis with the respective code. Detailed markdown of the RNAseq analysis can be found in Supplementary File 1.

Uniform Manifold Approximation and Projection for dimension reduction

UMAP method (Becht et al. 2019) was used to reduce the dimensions of mitochondrial features. UMAP is a non-linear embedding method that distributes data variability along major

axes. It preserves the original pairwise distance between the input data structure over the global distance by projecting data into a newly constructed manifold. The UMAP manifold follows the theoretical framework of Riemannian geometry and algebraic topology. Cells with similar mitochondrial values cluster together in the UMAP morphospace, while those with different features are further apart.

Voxel registration to Stereotaxic Montreal Neurological Institute (MNI) Space

The image of the brain slab before milling (Extended Data Fig. 1b) was converted to Neuroimaging Informatics Technology Initiative (NIfTI) format using a homemade code (Supplementary File 4). Then, a corresponding grid overlay (Extended Data Fig. 8) was delineated manually onto the converted brain slice using FSLeyes as part of the FMRIB Software Library v6.0 (https://fsl.fmrib.ox.ac.uk/) to produce a digital version of the grid saved as an independent NIfTI file. Each voxel of the digital grid was assigned a unique number and labeled as being gray, white or mixed matter by an expert anatomist (MTS). Additionally, each voxel was labeled with an anatomical label derived from the Atlas of Human Brain Connections (Catani et al. 2012).

Next, we registered the coronal slice to the MNI space (MNI152 nonlinear 6th generation; http://www.bic.mni.mcgill.ca) using affine and elastic deformation provided in the MIPAV v10.0 software package (http://mipav.cit.nih.gov). After visual inspection for the alignment, the same deformation was applied to the digital grid to obtain a digital grid in the MNI space (Extended Data Fig. 8). The grid was subsequently split and binarized so that each voxel corresponded to one binary NIfTI file. To create a representation of the mitochondrial values in the MNI stereotaxic space, values collected for each sample were attributed to each corresponding NIfTI file that were subsequently summed to produce individual maps of the 6 mitochondrial parameters (CI, CII, CVI, MitoD, TRC and MRC).

To produce comparisons between these values and neuroimaging, we used neuroimaging values derived from averaged images computed from a sample of 1870 university students (Tsuchida et al. 2021) (Extended Data Table 1) and the human connectome project (Van Essen et al. 2013). First, mapping of each voxel within the MNI space was manually verified and samples with a sum of GM and WM probabilities less than 70% (95 samples) were discarded to avoid partial volume effect contamination. The remaining 539 voxels with all mitochondrial features measured and correctly mapped into the stereotaxic space were randomly divided into 80% 'learning' (431 samples) and 20% 'testing' (108 samples) datasets (Extended Data Fig. 11). Predictive model was built by means of 6 stepwise backward linear regressions with neuroimaging values used as independent variables to predict each of the 6 mitochondrial values (i.e. CI, CII, CIV, MitoD, TRC and MRC) in the learning dataset. In the backward hierarchical linear regression, predictors are eliminated one by one, starting from the least significant. The procedure of elimination continues until the comparison between two consecutive models is not statistically significant. To test a null distribution of the values, the same analysis was performed on a randomized version of the same dataset (Extended Data Fig. 11c). Next, the models were applied to the 20% 'testing' dataset to verify out-of-sample quality of predictions. Then, the model was extended to all the brain voxel of the MNI space at $1mm^3$ resolution to produce a whole brain map for each mitochondrial value. 3D maps of predicted mitochondrial features for the whole human brain are available at https://identifiers.org/neurovault.collection:16418.

Evolution and mitochondrial values

To determine whether increased mitochondrial OxPhos follows a phylogenetic gradient, we used two maps to estimate cortical evolution (Extended Data Fig. 12). The GM variability map has been shown to reflect evolution and individual differences in humans and our closest evolutionary relatives (Croxson et al. 2018). The second map compares macaque-to-human

cortical expansion using a transformation map from Caret (Essen and Dierker 2007). This map was created by aligning 23 landmarks in both species and measuring the geodesic distance between homologous regions (http://brainvis.wustl.edu/).

Statistical analysis

Data was analyzed and graphed using Igor Pro (Wavemetrics, Lake Oswego, OR; RRID:SCR_000325), Python Programming Language (RRID: SCR_008394), R Project for Statistical Computing (RRID: SCR_001905) and Prism 8.0 software (GraphPad Software Inc, San Diego, CA; RRID:SCR_002798). Data sets with normal distributions were analyzed for significance using unpaired Student's two-tailed t-test or analysis of variance (ANOVA) followed by Tukey's post hoc test. Data sets with non-normal distributions were analyzed using the Mann-Whitney U test or Kruskal-Wallis test with Dunn's adjustment for multiple comparisons. The violin plots are displayed as median ± quartiles; line graphs and data in the text are expressed as mean ± standard error of the mean (SEM). The statistical tests are listed in the figure legends.

Figures

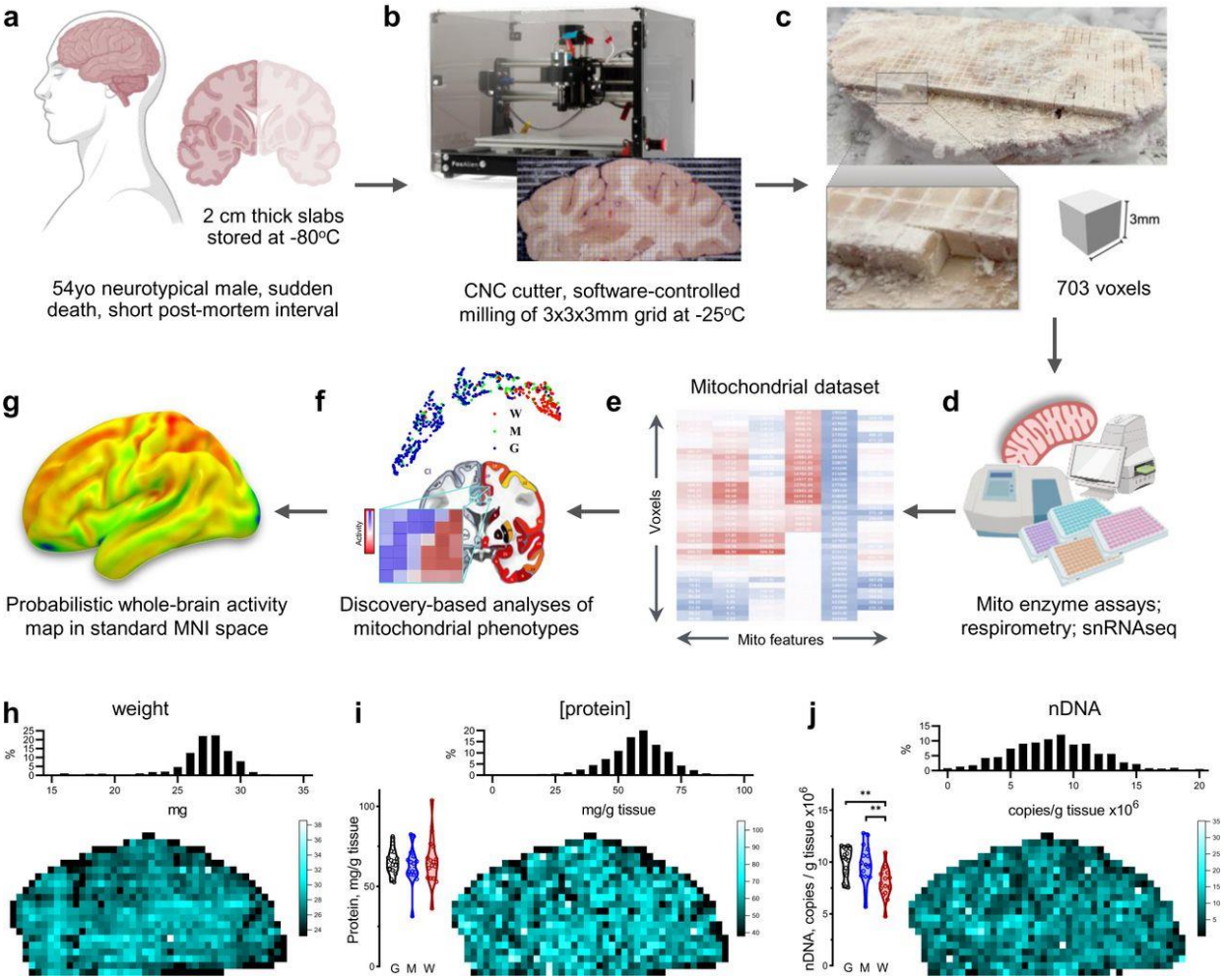

Figure 1: Overall Strategy of Brain Voxelization and Mapping

a, Postmortem brain tissue was sectioned into ~2 cm thick coronal slabs, flash frozen in refrigerant HFC-134a and stored in −80°C freezer for 10 years (see Methods). **b,** A slab located at stereotactic Montreal Neurological Institute (MNI) coordinates 15.51 mm posterior to the center of the anterior commissure (Mai, Majtanik, and Paxinos 2015), was mounted on a computer numerical control (CNC) cutter operated in a −25C freezer room. **c,** The top surface was cleaned and leveled, and a square 3×3 mm grid was milled with a 0.4 mm drill bit to the depth of 3 mm. Brain voxels were manually collected, the surface cleaned once more, and several 50 µm cryosections were collected for histological evaluation. **d,** Each of the >700

samples was weighed, homogenized and ran through an array of biochemical tests, generating matrixes of mitochondrial features linked to voxel coordinates on the brain slice. **e,** Each voxel was characterized based on relative activities and abundance of mitochondrial complexes. **f,** Dimensionality reduction and clustering analysis was performed to identify different mitochondria phenotypes. Maps of mitochondrial features were registered onto a standard MNI space and correlated with average MRI readouts for the same brain regions. **g,** Finally, MRI data was used to predict mitochondrial features and to extend mitochondrial maps to the whole brain. **h-j**. Basic properties of collected voxels, including their (h) weight, (i) protein content and (j) nuclear DNA content. Histograms of each parameter values are shown on top and mapping of values on the brain slice at the bottom. Bar graphs on the left show repeated measurements of the corresponding values in control gray (G), white (W) and mixed (M) matter samples from the occipital lobe of the same brain that were used as normalization controls in the assay plates (see Extended Data Fig. 2).

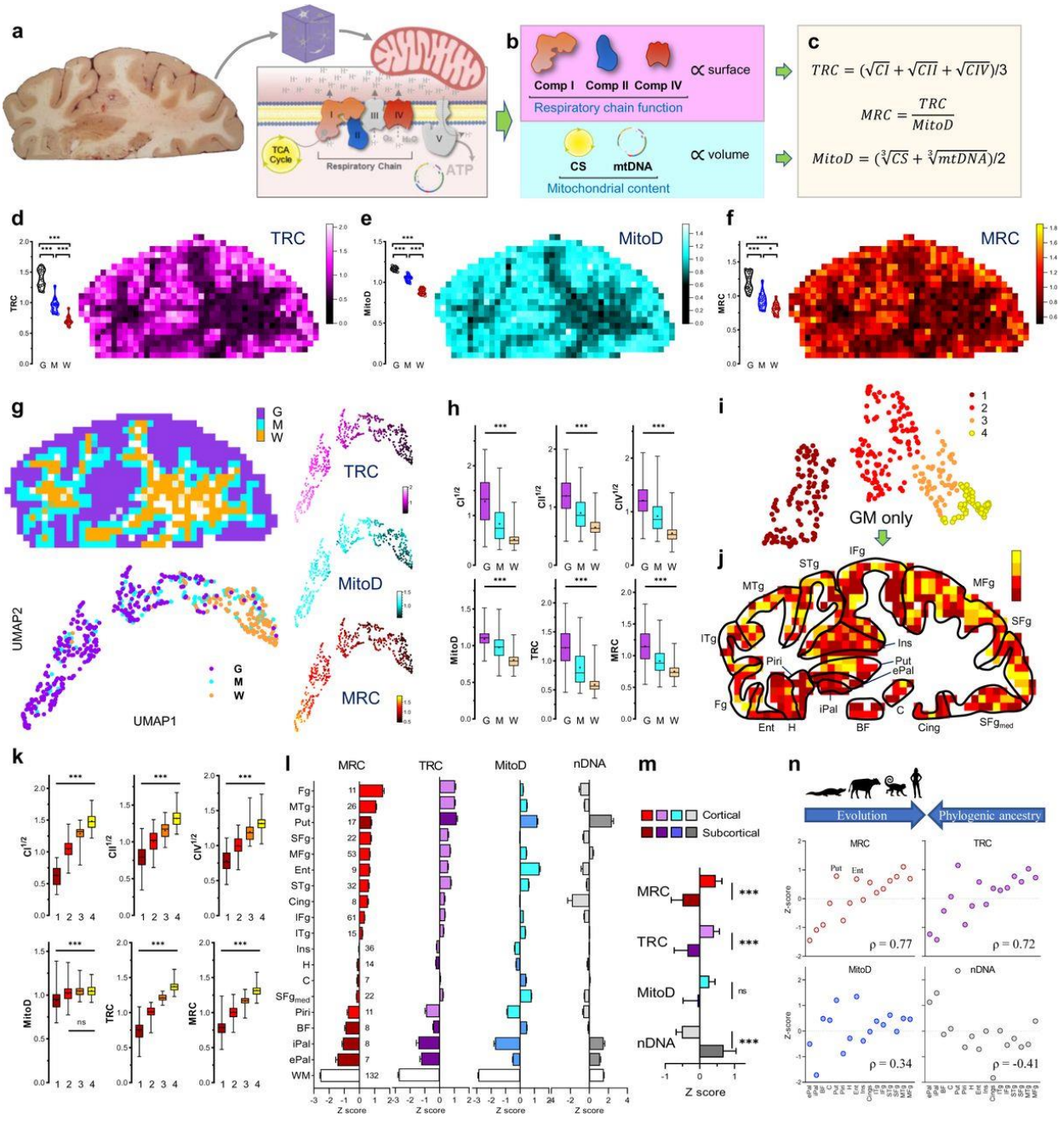

Figure 2: Mitochondrial density and Respiratory Complexes Activity Assays

a, Human brain slab before voxelization and schematic of the inner mitochondria membrane with respiratory chain (RC) complexes I-V. **b,** If organelle radii are normally distributed, activities of RC complexes that are proportional to the membrane surface should follow square root normal distribution. Citrate synthase (CS) and mtDNA levels are proportional to mitochondria

volume and thus should follow a cube root normal distribution. **c,** Formulas for Tissue Respiratory Capacity (TRC), mitochondria density (MitoD) and Mitochondria Respiratory Capacity (MRC). Note that complex activities are normalized by tissue weight during sample preparation. **d-f,** Maps of TRC (d, derived from Extended Data Fig. 4c,d), MitoD (e, average of two panels on Extended Data Fig 4a), and MRC (f). Bar graphs on the left of each panel show distributions of repeated measures of control gray, white and mixed matter samples on different assay plates. **g,** Based on MNI space location (Extended Data Fig. 7), 633 voxels that had all 6 mitochondrial features (CI, CII, CIV, MitoD, TRC and MRC) were divided into gray (G, n=325), white (W, n=132) and mixed (M, n=176) matter clusters. Uniform Manifold Approximation and Projection (UMAP) algorithm was applied for dimension reduction. UMAP plots correlating clusters with physical location of each voxel (left) or z-score values of TRC, MitoD and MRC in each voxel (right). **h,** Bar (25 - 75 percentile) and whiskers (min and max) plots of mito features in voxels mapped to GM, WM and mixed tissue in MNI space. ***-all groups are significantly different from each other by one-way ANOVA with Tukey's post-hoc test ($p<0.001$). **i,** UMAP plot and clusters of mitochondrial features of GM voxels. **j,** Mapping of voxel UMAP clusters on specific brain areas (see below for abbreviations). **k,** Comparison of mitochondrial features in four GM clusters identified on i. ***-significantly different from each other by one-way ANOVA with Tukey's post-hoc test ($p<0.001$); for MitoD, only cluster 1 is different from all other clusters. **l,** Comparison of mitochondrial features in groups of voxels mapped into specific brain areas in the MNI space. Subcortical areas are shown in darker shades. **m**, Average z-scores of mitochondrial features in cortical and subcortical areas. ***-significantly different by t-test ($p<0.01$). **n,** Comparison between measured values and the known phylogenetically organization of main brain areas derived from comparative anatomy studies. Spearman's rho is shown at the bottom-right. ePal, external pallidum; iPal, internal pallidum; BF, basal forebrain; C, caudate; Put, putamen. Areas also present in mammals with some close equivalent in reptiles:

Piri, piriform cortex; H, hippocampus. Areas also present in mammals but not in reptiles: Ent, entorhinal cortex; Ins, insula; Cing, cingulate cortex. Neocortex in primates: ITg, inferior temporal gyrus; STg, superior temporal gyrus; SFg, superior frontal gyrus. Neocortex in humans: MTg, middle temporal gyrus; MFg, middle frontal gyrus.

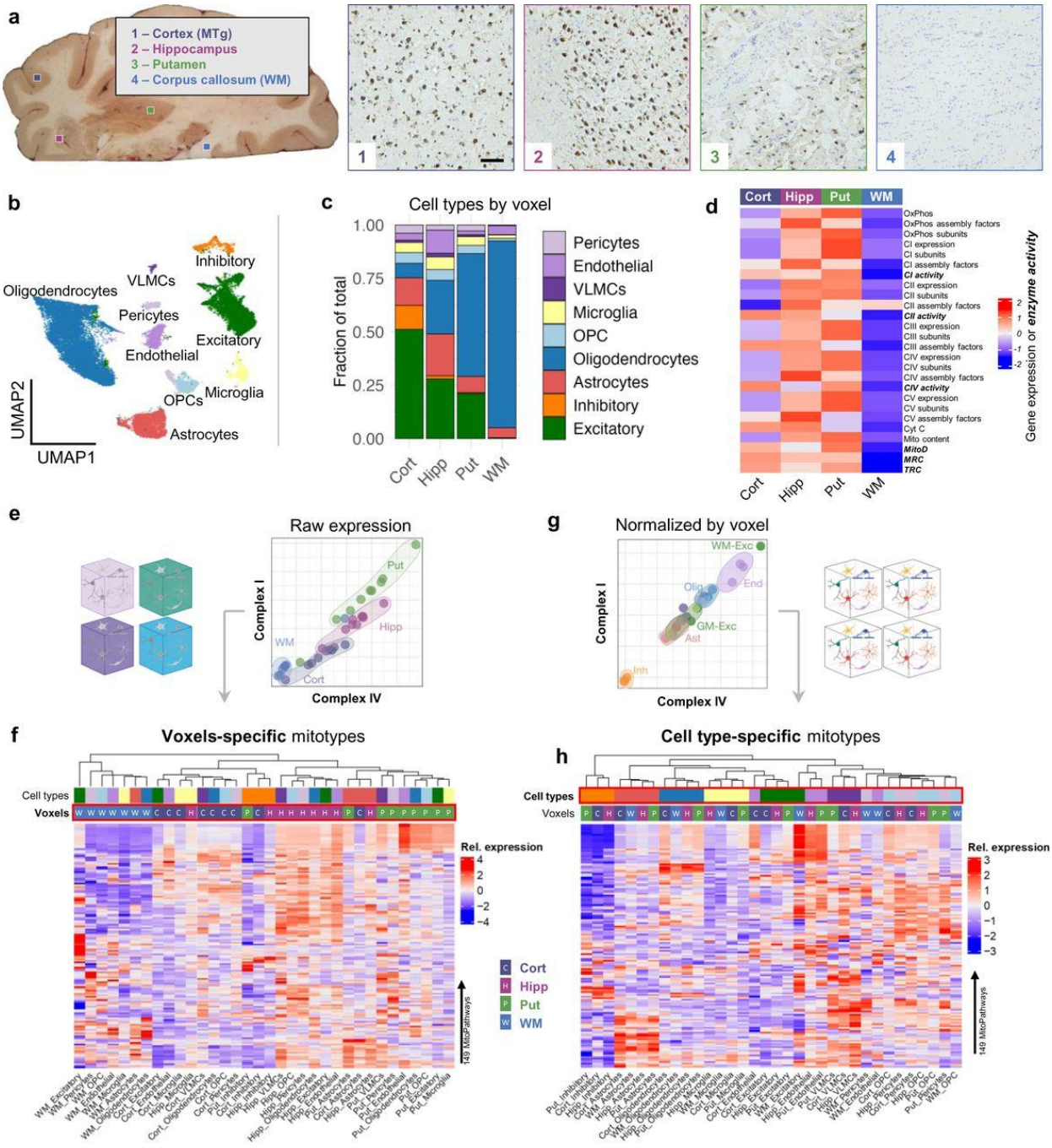

Figure 3: snRNAseq Analysis of Selected Voxels

a, Location of voxels selected for snRNAseq analysis and their histological evaluation. Thin brain slices were stained with Nissl (blue, all nuclei) and immunolabeled for NeuN (brown, neuronal cells). Scale bar is 100 μm. **b**, UMAP plot of cell clusters identified by snRNAseq analysis of 4 voxels shows 9 major cell types. **c**, Cell type proportions in each of the 4 voxels. **d**, Heatmap of OxPhos pathway gene expression scores of each voxel (pseudobulk expression per sample), together with the activity measurements (bold). **e**, Correlations between complexes I and IV expression. Each data point represents pseudobulk expression of OxPhos subunits in each voxel/cell type and is color-coded by the voxel type. **f**, Heatmap of 149 mitochondrial pathway expression scores (see Supplementary File 1). Each column represents raw expression scores in a voxel/cell type color coded in the first two rows (same colors as in *a* for voxels and *c* for cell types). Note clustering of the samples by their voxel type. **g**, Correlations between complexes I and IV expression after z-score normalization of expression levels within each voxel type to account for region-specific differences. Each data point is color coded by its cell type. **h**, Heatmap of mitochondrial pathways expression scores in voxels/cell types after expression was normalized within each voxel. Clustering of samples by their cell type is now obvious.

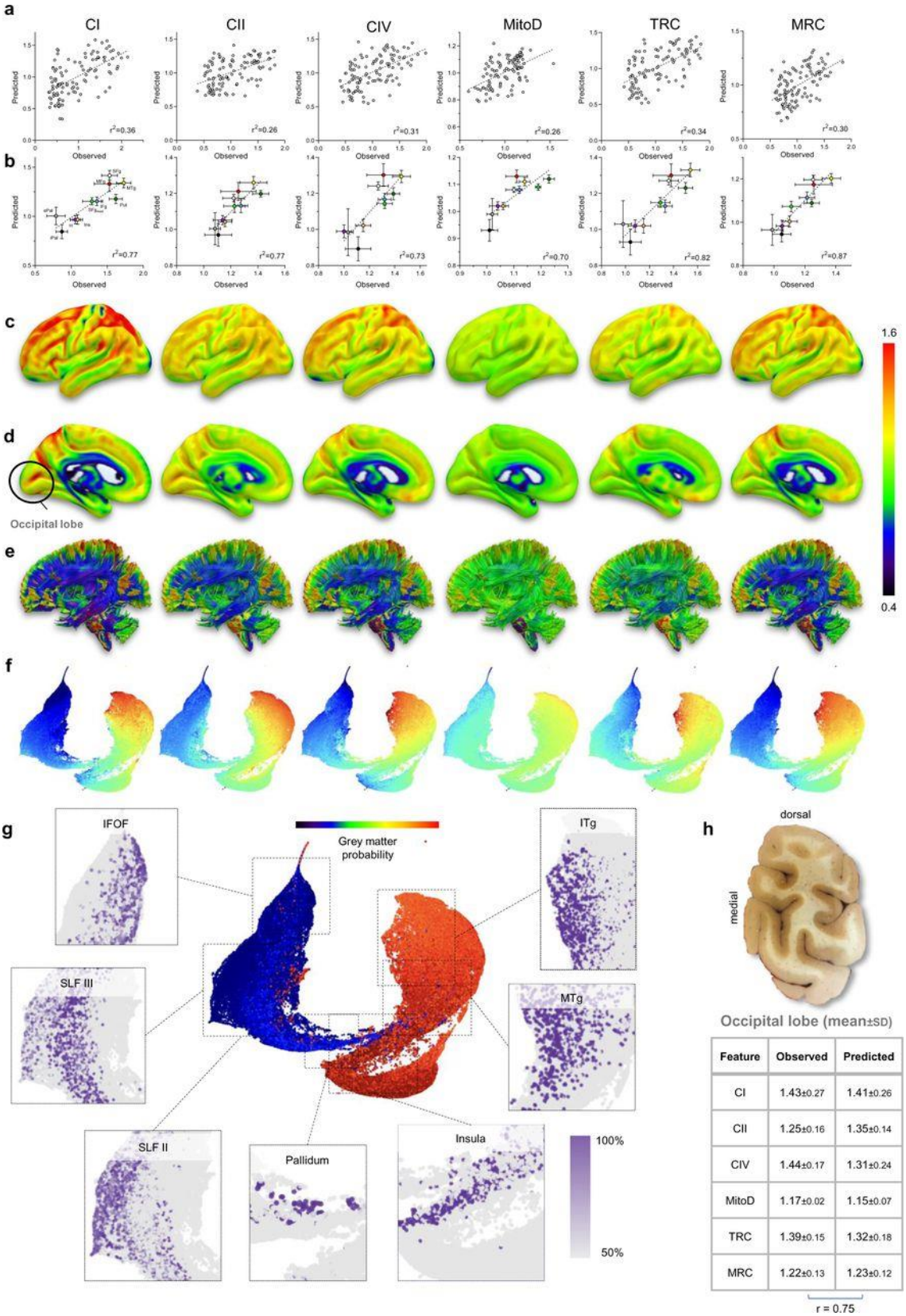
a
CI
CII
CIV
MitoD
TRC
MRC
Predicted
Observed
r²=0.36
r²=0.26
r²=0.31
r²=0.26
r²=0.34
r²=0.30
b
r²=0.77
r²=0.77
r²=0.73
r²=0.70
r²=0.82
r²=0.87
c
d
Occipital lobe
e
1.6
0.4
f
g
IFOF
Grey matter probability
ITg
SLF III
MTg
SLF II
Pallidum
Insula
100%
50%
h
dorsal
medial
Occipital lobe (mean±SD)
Feature
Observed
Predicted
CI
1.43±0.27
1.41±0.26
CII
1.25±0.16
1.35±0.14
CIV
1.44±0.17
1.31±0.24
MitoD
1.17±0.02
1.15±0.07
TRC
1.39±0.15
1.32±0.18
MRC
1.22±0.13
1.23±0.12
r = 0.75

Figure 4: Projected Mitochondrial Activities of the Whole Brain

a, Scatterplots of 20% out-of-sample prediction of mitochondrial profiles (see Extended Data Fig. 11). **b,** Correlations between observed and predicted mitochondrial features for brain areas rather than individual samples. Both 'learning' and 'testing' samples were used. n**=**5 voxels (ePal and iPal), 7 (MTg), 9 (MFg), 11 (IFg_{med}) 15 (H, Put and SFg), 27 (Ins), 33 (IFg). Slopes of all linear regressions on *a* and *b* are different from zero ($p<0.0001$; Pearson's r^2 is shown on each graph). **c-e,** Prediction of whole brain values for the lateral (c), medial (d) surfaces and the white matter connections (**e,** lateral view). 3D maps are available at https://identifiers.org/neurovault.collection:16418. **f,** UMAP embedding of the whole brain at 1 mm^3 resolution, colors indicate mitochondrial activity profiles. **g,** UMAP plot of the whole brain with colors indicating the probability of each point being located in the white or gray matter. Insets show probabilities of voxels being in specific white matter (inferior fronto-occipital fasciculus, superior longitudinal fasciculus) or gray matter (pallidum, insula, middle temporal gyrus, inferior temporal gyrus) brain structures ($p < 0.0001$ Bonferroni corrected for multiple comparisons). **h,** An image of the occipital lobe brain slab before milling (top) and summary table of mitochondrial features in the pooled gray matter OL samples used as loading controls (see Extended data Fig. 3). Predicted values were generated by averaging MRI-based model predicted mitochondrial metrics in 10 randomly selected GM voxels in the MNI space. Observed and predicted datasets are not different by 2-way ANOVA ($F_{1,144}=0.69$, $p=0.41$); Pearson's r is shown below the table.

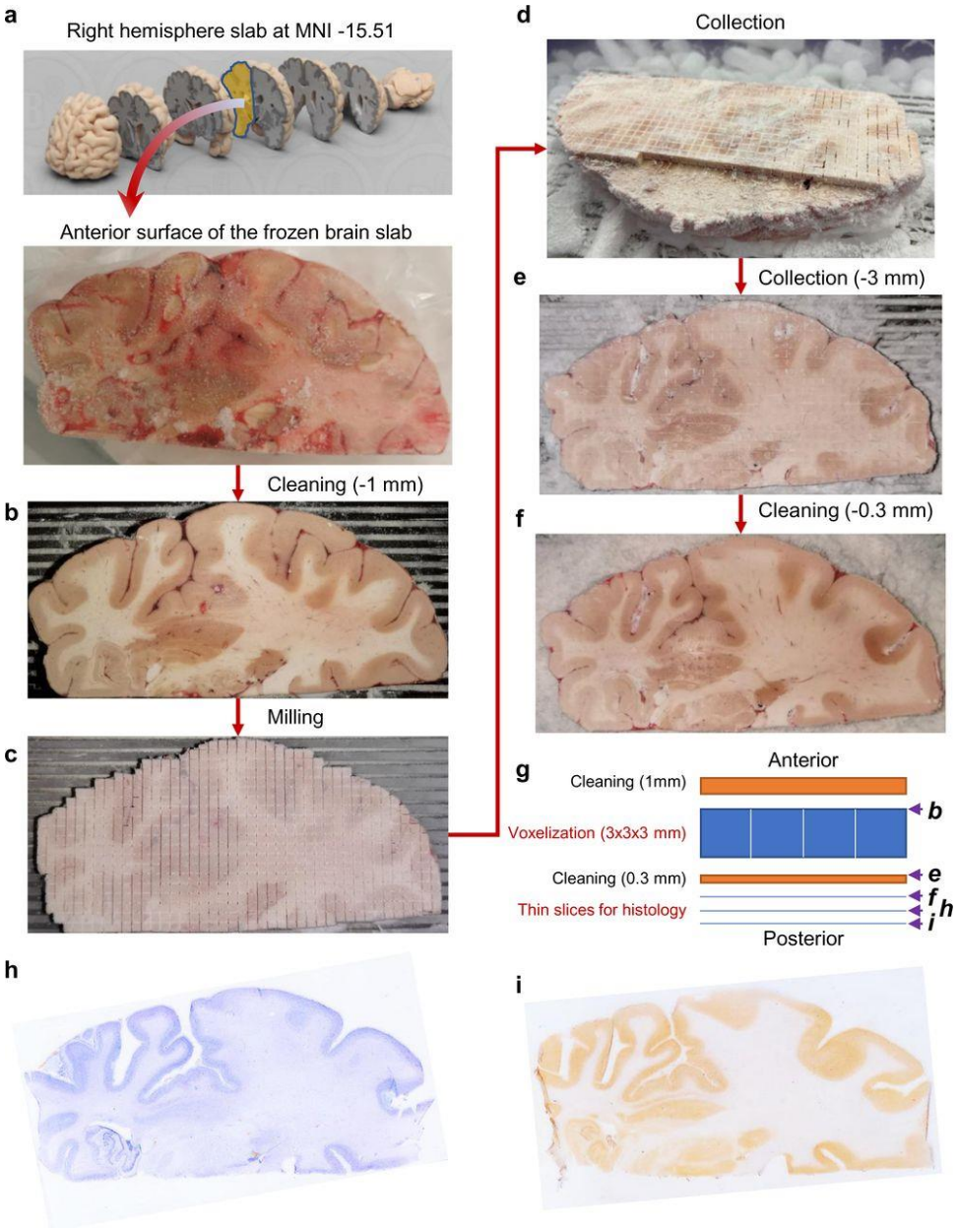

Extended Data Figure 1: Workflow of Tissue Collection

a, The right hemisphere coronal slab was mounted on a metal plate with an OCT compound with the top (anterior) surface of the slab parallel to the plate. **b,** After affixing the plate to the computer numerical control (CNC) cutting area, the top surface was cleaned with a 12.7 mm flat-tip drill bit rotating at 100 RPM and moving horizontally at 300 mm/sec. After cleaning 1 mm from the top, morphological brain structures were clearly visible and the surface was parallel to

the plane of drill bit movement, ensuring that voxels will be of a uniform height. **c,** A 3×3 mm grid was milled with a 0.4 mm drill bit rotating at 10,000 RPM and moving horizontally at 250 mm/sec. During a single pass, 0.2 mm of the depth was milled, requiring 15 passes to reach the desired 3 mm of cut depth. Total milling time for a 130.8 x 61.25 mm hemisphere was ~5h. **d,** Fully milled slab was placed on dry ice. First, four samples of shavings were collected from the surface above one white and three gray areas (Extended Data Fig. 2). Next, shavings were gently removed from the surface with a brush and a pre-chilled scalpel and forceps were used to collect 703 individual voxels. **e,** Following sample collection, slab surface was cleaned once more with a 12.7 mm drill bit. **f,** The metal plate with the slab was then mounted on a freezing microtome and several 50 µm-thick cryosections were collected for histological evaluation. **g,** Summary of the steps during the collection of brain voxels and thin sections. Letters on the right refer to images shown on the corresponding panels. **h and i,** Thin brain section stained with Nissl to show neurons and glia either alone (h) or in combination with an immunostaining against neuronal nuclear antigen NeuN to highlight neuron-enriched areas (i).

a

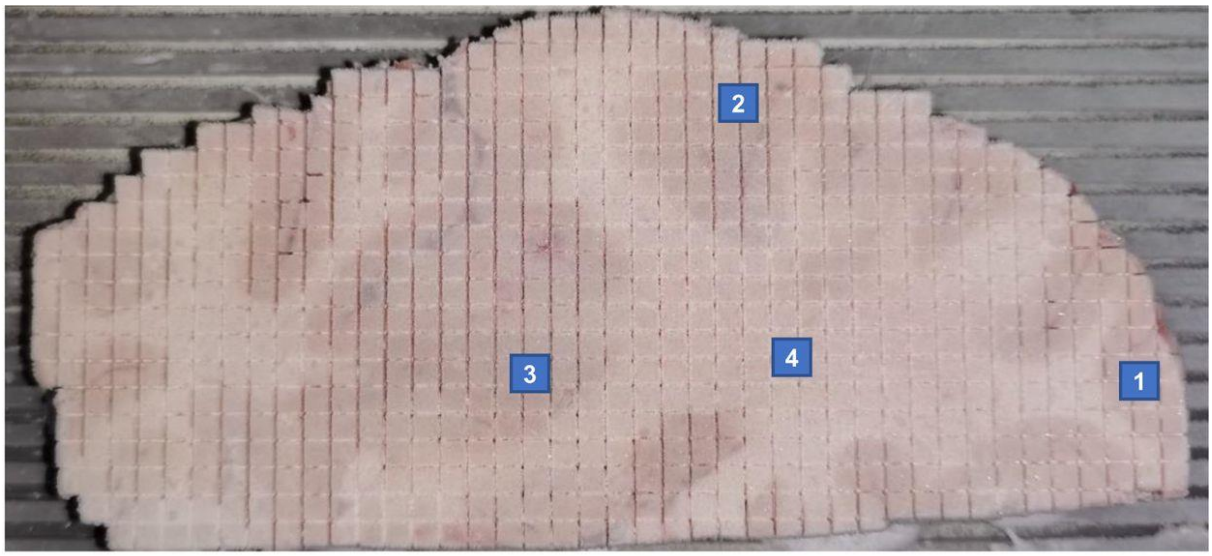

b

	Area	MitoD		TRC		MRC	
		tissue	dust	tissue	dust	tissue	dust
1	SFg	1.15 ± 0.07	0.97 (**85%**)	1.3 ± 0.19	0.53 (**40%**)	1.14 ± 0.18	0.54 (**48%**)
2	MFg	1.06 ± 0.04	1.01 (**96%**)	1.4 ± 0.27	0.54 (**39%**)	1.31 ± 0.21	0.53 (**40%**)
3	Put	1.16 ± 0.03	0.98 (**85%**)	1.42 ± 0.18	0.73 (**51%**)	1.22 ± 0.13	0.74 (**61%**)
4	SLF	0.69 ± 0.02	0.66 (**96%**)	0.46 ± 0.12	0.44 (**95%**)	0.68 ± 0.18	0.67 (**99%**)

Extended Data Figure 2: Collection and Analysis of Tissue Shavings

a, Positions of collection sites of the four tissue shavings. Samples 1-3 were above the grey matter areas, while 4 was above a white matter area. **b,** Comparison of mitochondrial activities between the four 'dust' samples and corresponding tissue samples collected below after tissue voxelization. Values are mean ± SD. While all mitochondrial features (MitoD, TRC and MRC, see Fig 2c for definitions) were lower in all dust samples compared to tissue collected below, MitoD was less different between brain dust and tissue block. Moreover, in sample 4, brain dust and voxels features appear to be very similar, but this likely indicates that colorimetry and respirometry assays are at their detection limit when measuring mitochondria complex activities in the white matter.

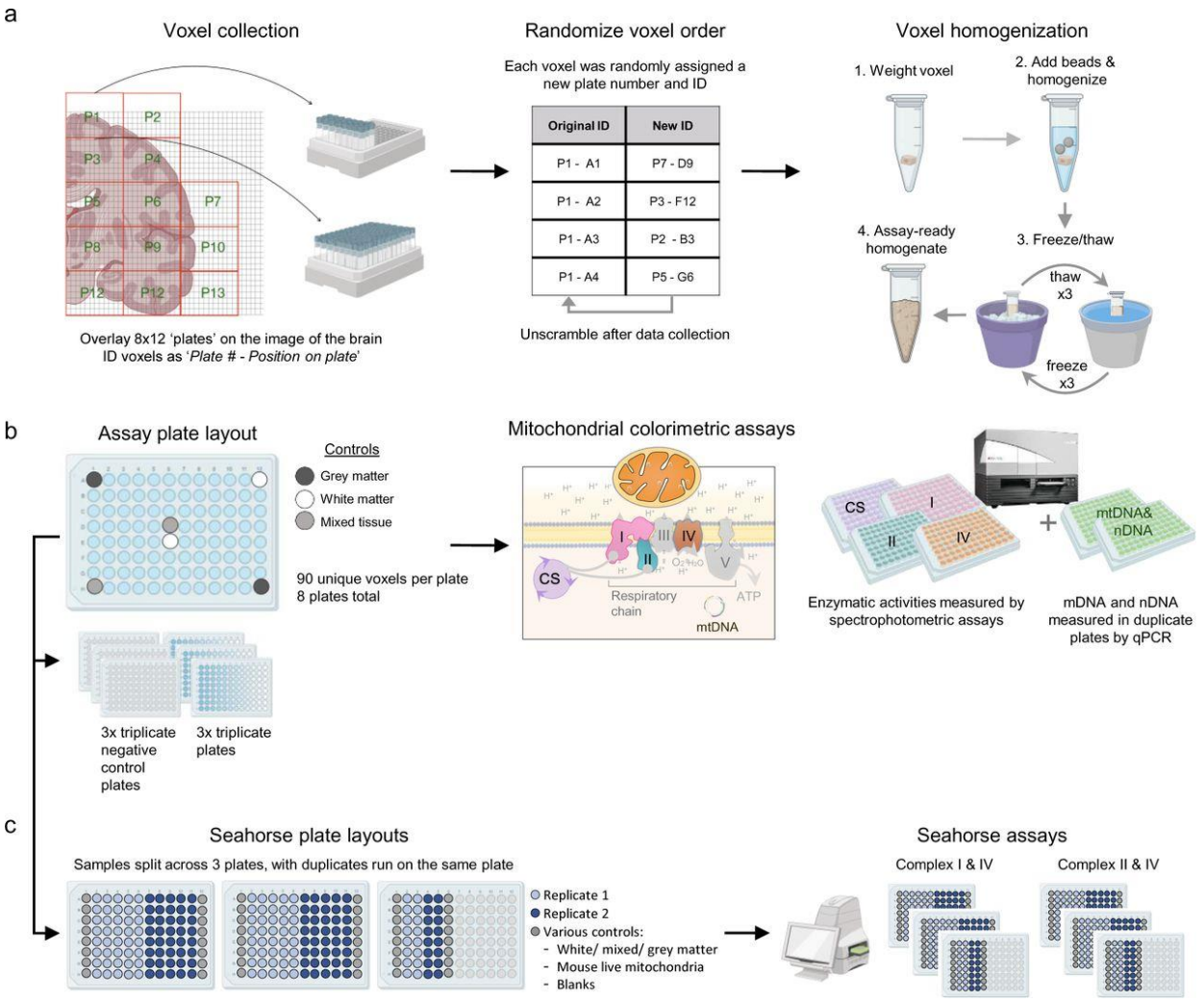

Extended Data Figure 3: Workflow for Mitochondrial Colorimetric and Respiratory Assays

a, Brain voxel collection and preparation. **b,** Voxel plating and data collection for colorimetric mitochondrial assay and qPCR. **c,** Frozen tissue respirometry plate layouts derived from the assay plates in *b* to accommodate all samples and ran in duplicate. Samples were loaded into Seahorse plates at a constant volume rather than constant protein content.

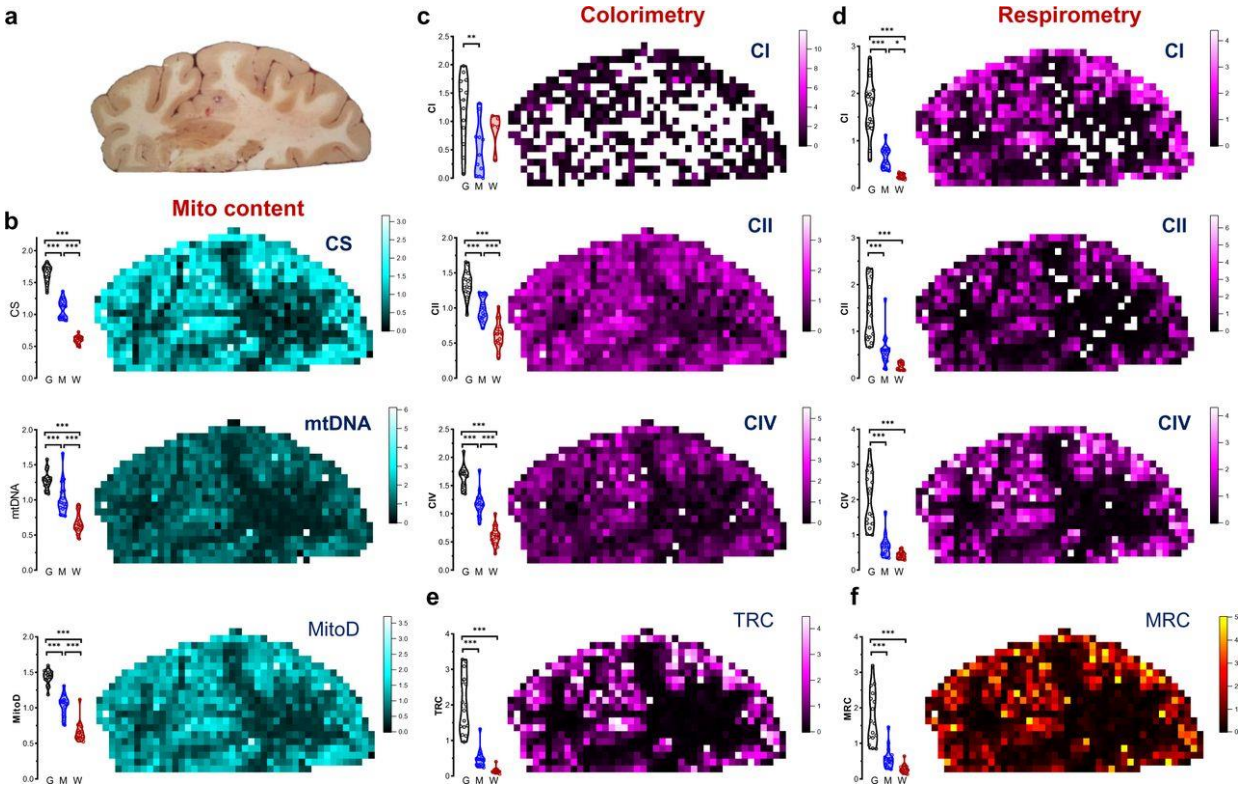

Extended Data Figure 4: Raw Mitochondrial Features Measured by Colorimetric and Respirometry Assays

a, Image of the brain slab before voxelization. **b,** Distributions of non-transformed values (i.e., values are in a linear scale) of citrate synthase (CS) activity, mitochondrial DNA (mtDNA) density and mitochondrial density (MitoD). **c and d,** Mapping of mitochondria complexes I, II and IV (CI, CII and CIV) activities measured by colorimetry (c) and respirometry (d) assays. **e and f,** Tissue Respiratory Capacity (TRC) and Mitochondria Respiratory Capacity (MRC) calculated from raw (non-transformed) values of enzymatic activities. Same maps derived from power transformed values of enzymatic activities are shown on Fig. 2e-f. Activity readouts were normalized to each group's mean. Bar graphs on the left of the panel show distributions of repeated measures of control gray, white and mixed matter samples on different assay plates (i.e., data points are technical replicates of the same samples).

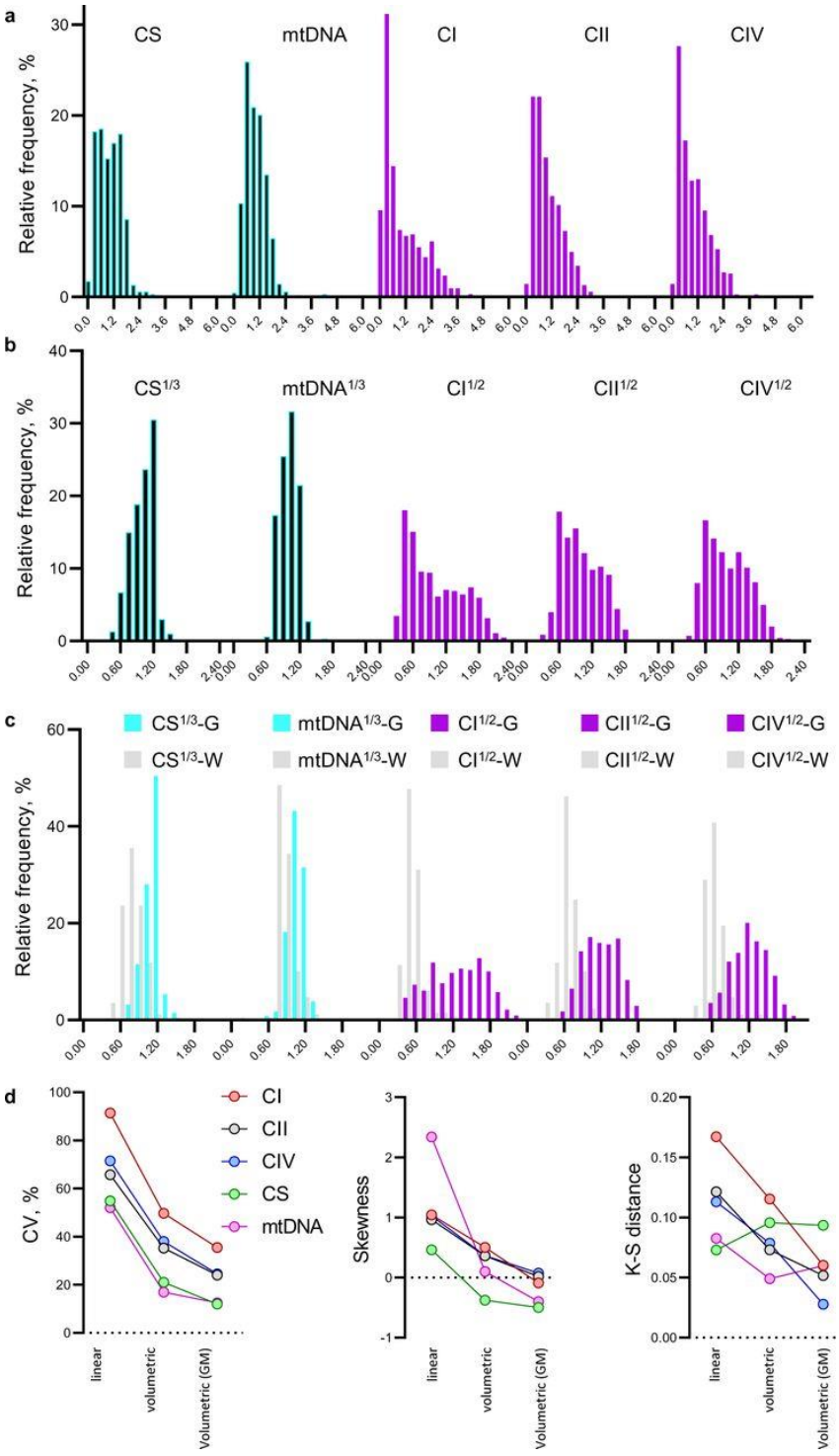

Extended Data Figure 5: Volumetric Transformation of Mitochondrial Parameters Normalizes Their Distributions

a, Distributions of complexes I, II and IV activities, CS activity and mtDNA density. Complex activities are averages from colorimetry and respirometry assays. **b,** Volumetric transformations of the data on *a*. Mitochondria density metrics and OxPhos complexes activities were calculated as averages of cube root and square root values from colorimetric and respirometry assays. **c,** Same data as *b* with voxels assigned to Gray matter (G, n=339) and White matter (W, n=169) clusters based on their anatomical location. Voxels with mixed identity (n=194) are not shown for simplicity.

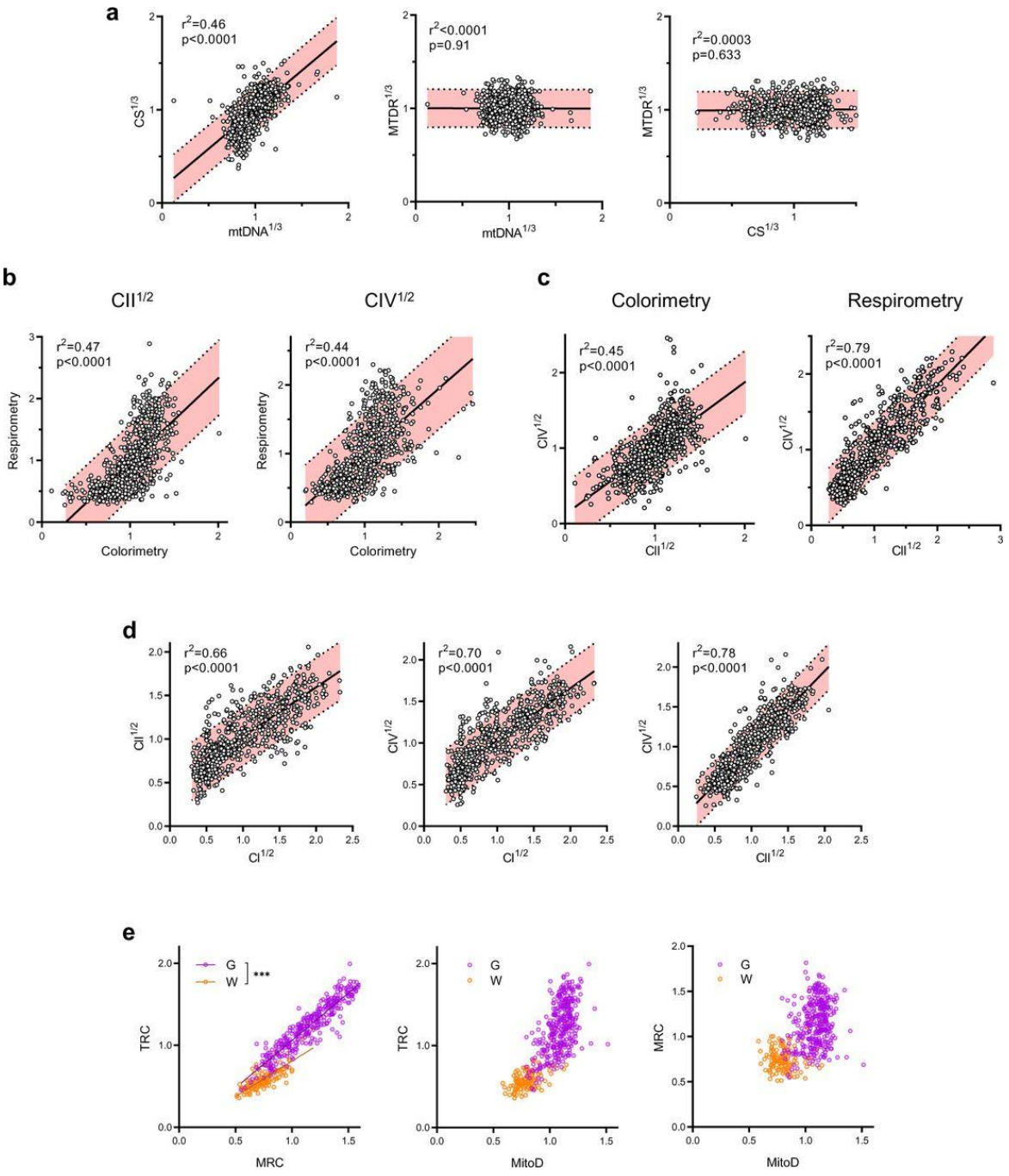

Extended Data Figure 6: Correlations Between Mitochondrial Parameters Assayed Using Different Techniques

a, CS activity and mtDNA density, which are related to mitochondria mass, are positively correlated. Because of the high variability in MitoTracker Deep Red (MTDR, a far-red fluorescent probe used to chemically mark and visualize mitochondria in cells) values, they

correlated poorly with CS and mtDNA, thus MTDR was not used for the analysis. **b and c,** Relationship between CII and CIV activities measured by colorimetric and respirometry assays. **d,** Correlations between CI, CII and CIV activities (an average between colorimetric and respirometry assays). **a-d,** Pearson's r^2 values show how well datapoints follow the linear regression; *p* values indicate if the slope of the regression line is significantly different from zero; shaded areas represent 90% confidence interval. **e,** Relationship between TRC, MRC and MitoD values (see Fig. 2c for definitions) in gray and white matter voxels. *** - the slopes of linear regressions are different with p<0.001.

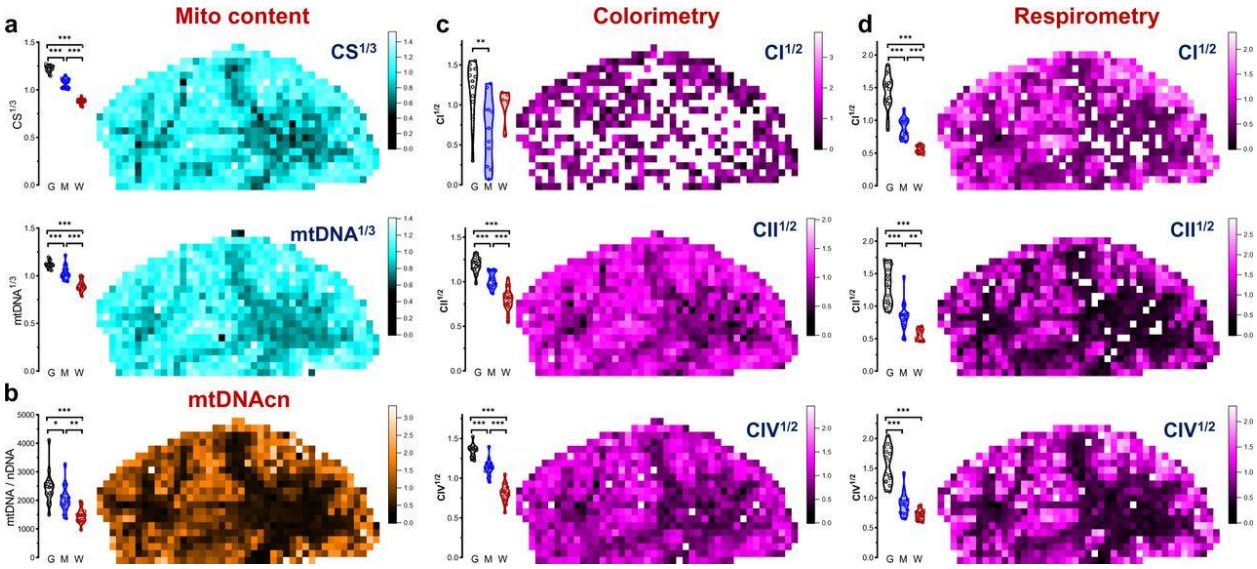

Extended Data Figure 7: Mitochondrial Features Measured by Colorimetry and Respirometry Assays.

a, Distributions of CS activity and mtDNA density. **b,** Measurements of mtDNA copy number (mtDNAcn) derived as a ratio of mitochondrial over nuclear DNA (mtDNA/nDNA). **c and d**. Mapping of CI, CII and CIV activities measured by colorimetry (c) and respirometry (d) assays. Because of the high variability of CI activities measured by colorimetry (c, top), these data were not used for TRC calculation. All values except mtDNAcn are normalized to each group's mean. Bar graphs on the left of each panel show distributions of repeated measures of control Gray,

White and Mixed matter samples on different assay plates (i.e., data points are technical replicates).

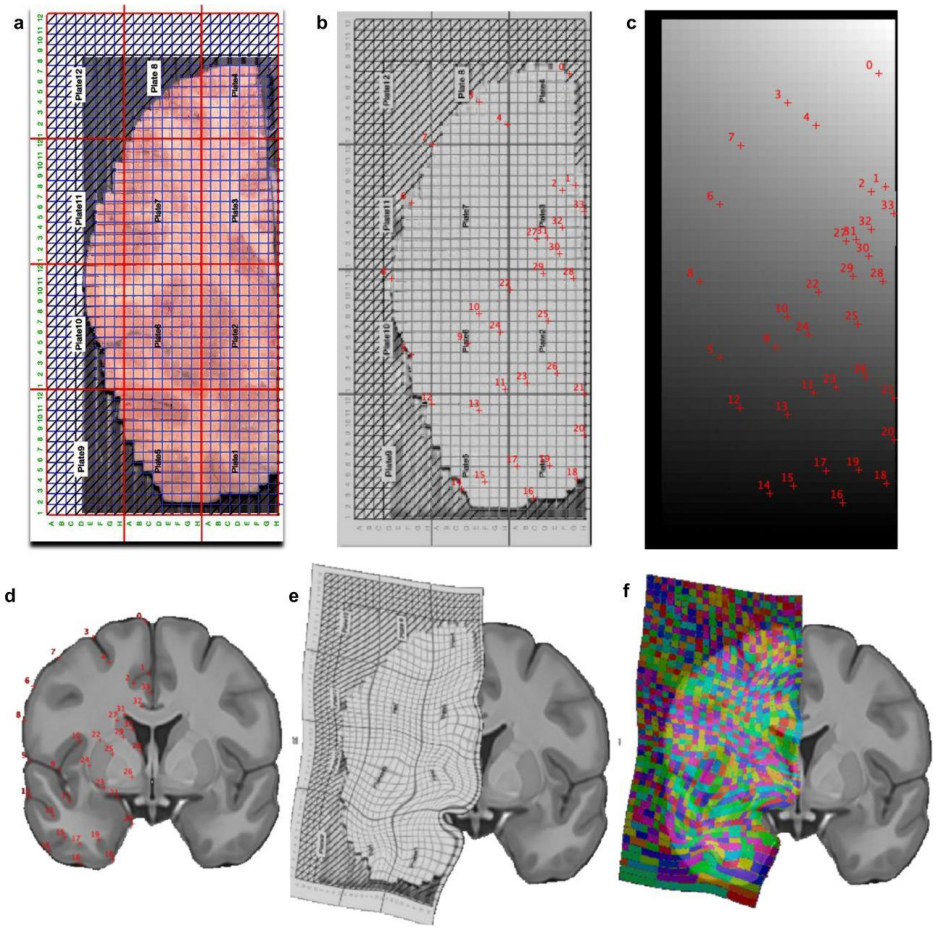

Extended Data Figure 8: Morphing the Partitioned Brain Slice into Montreal Neurological Institute (MNI) Space

a, Image of the partitioned brain slice with an overlaid milling grid. **b,** Conversion of the brain slice into Neuroimaging Informatics Technology Initiative (NIfTI) format and identification of 34 anatomical landmarks. **c,** Manual creation of NIfTI grid corresponding to the milling grid with the same coordinates. **d,** Identification of the anatomical landmarks as on *b* in the magnetic resonance imaging stereotaxic space (MNI152). **e,** Warping and deformation of the coordinates from *b* to *d*. **f,** Application of this deformation to *c* displayed in color onto the MNI152 for visual convenience. The following 34 anatomical landmarks were identified: top of the interhemispheric

fissure (0), surface (1) and deepest (2) point of the cingulate sulcus, surface (3) and deepest point (4) of the superior frontal sulcus (6), middle of the middle frontal gyrus (7), surface of the inferior frontal sulcus, middle surface of the inferior frontal gyrus (8), surface (5) and deepest point (9) of the lateral fissure, highest (10) and lowest (11) point of the circular insular sulcus, surface (12) and deepest point (13) of the superior temporal sulcus, surface (14) and deepest point (15) of the inferior temporal sulcus, surface (16) and deepest point (17) of the accessory temporopolar sulcus, surface (18) and deepest point (19) of the entorhinal sulcus, middle of the entorhinal cortex (20), most medial points of the amygdala (21), superior (22), inferior (23), lateral (24), and medial (25) putamen, most medial internal globus pallidus inferior (26), superior (27), inferior (28) lateral (29) and medial (30) caudate, highest point of the lateral ventricles (31), deepest point of the callosal sulcus (32) and middle of the cingulum gyrus (33).

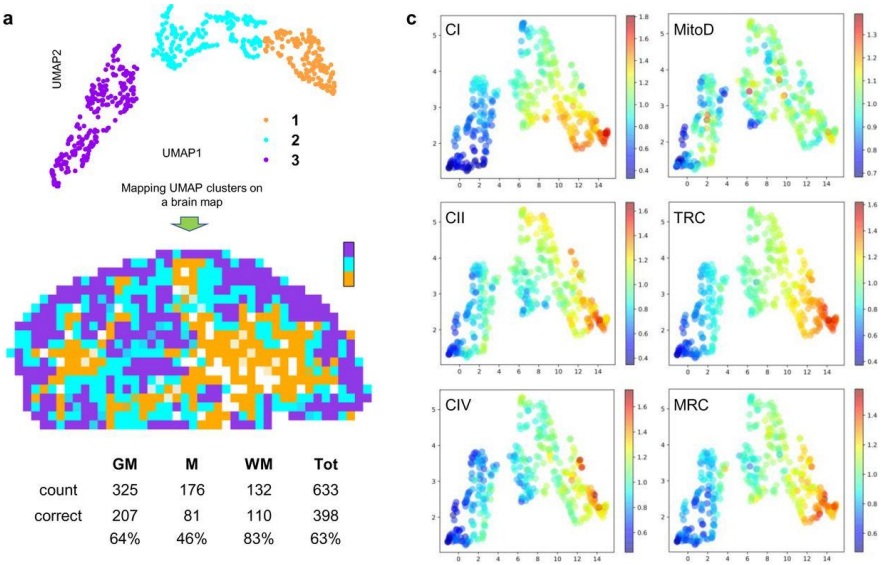

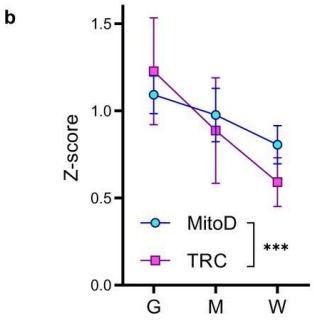

Extended Data Figure 9: Clustering of Brain Voxels by Similarities of Mitochondrial Density and OxPhos Activity

a, Three visually defined UMAP clusters (upper) obtained after dimensionality reduction of mitochondrial features of all brain voxels (Fig. 2g) were used to predict whether voxels originated from GM, WM or a mixed sample (middle). The table lists prediction accuracy with the number of voxels of each type and the fractions that were identified correctly. $X^2(2, N=1031)=10.3$, $p<0.01$. **b,** Both MitoD and TRC values were higher in GM than the WM voxels (same data as on Fig 2h are used; mean±SD), but the TRC decreases more than MitoD. ***-$p<0.0001$ by 2-way ANOVA ($F_{1,1260}=18.67$). **c,** Distribution of z-score values of each mitochondrial feature on the UMAP plot of GM voxels only (Fig. 2i).

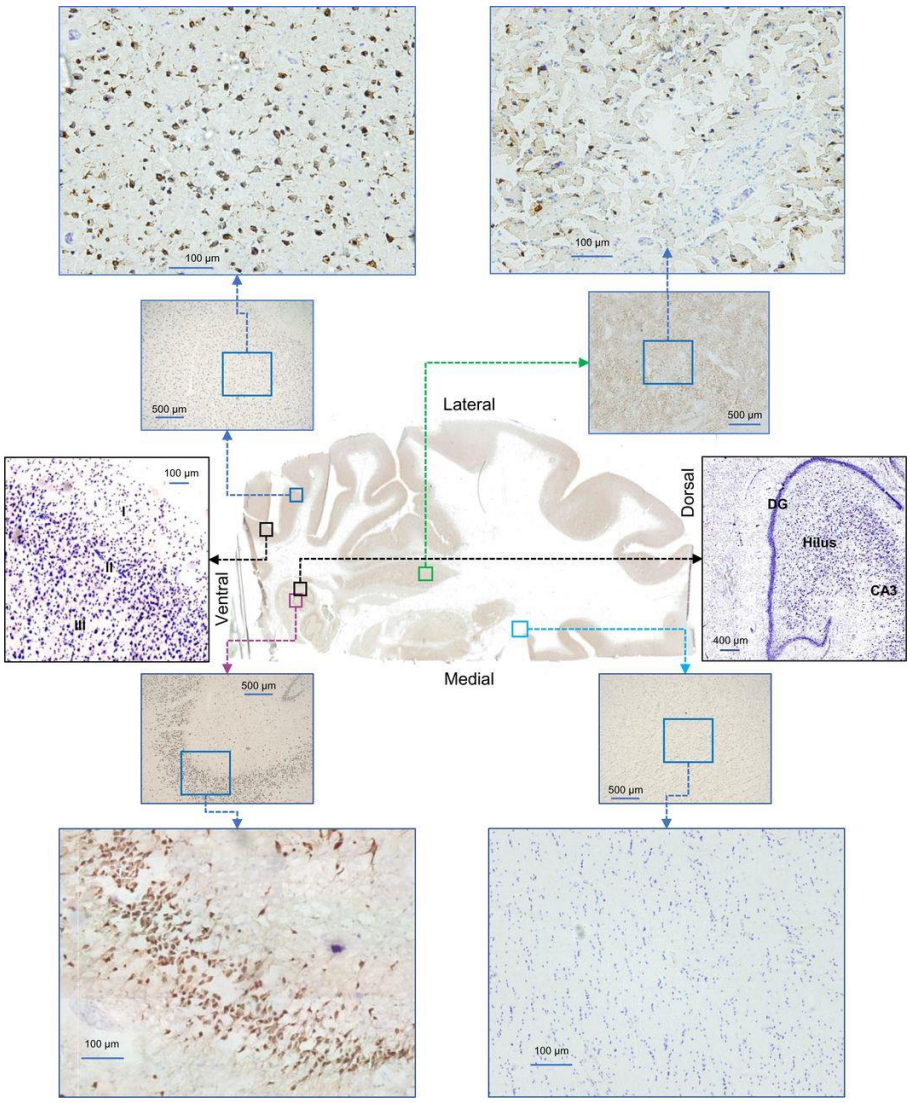

Extended Data Figure 10: Histological Evaluation of Brain Areas Used for snRNAseq Analysis

Staining of 50 µm sections obtained after brain voxelization (see Extended Data Fig 1) with Nissl stain (blue, neurons and glial cells) and NeuN (brown, neuronal cells). Two panels in black frames show Nissl-only stained sections with annotated cortical (layers I-II) and hippocampal (dentate gyrus, hilus and CA3) areas.

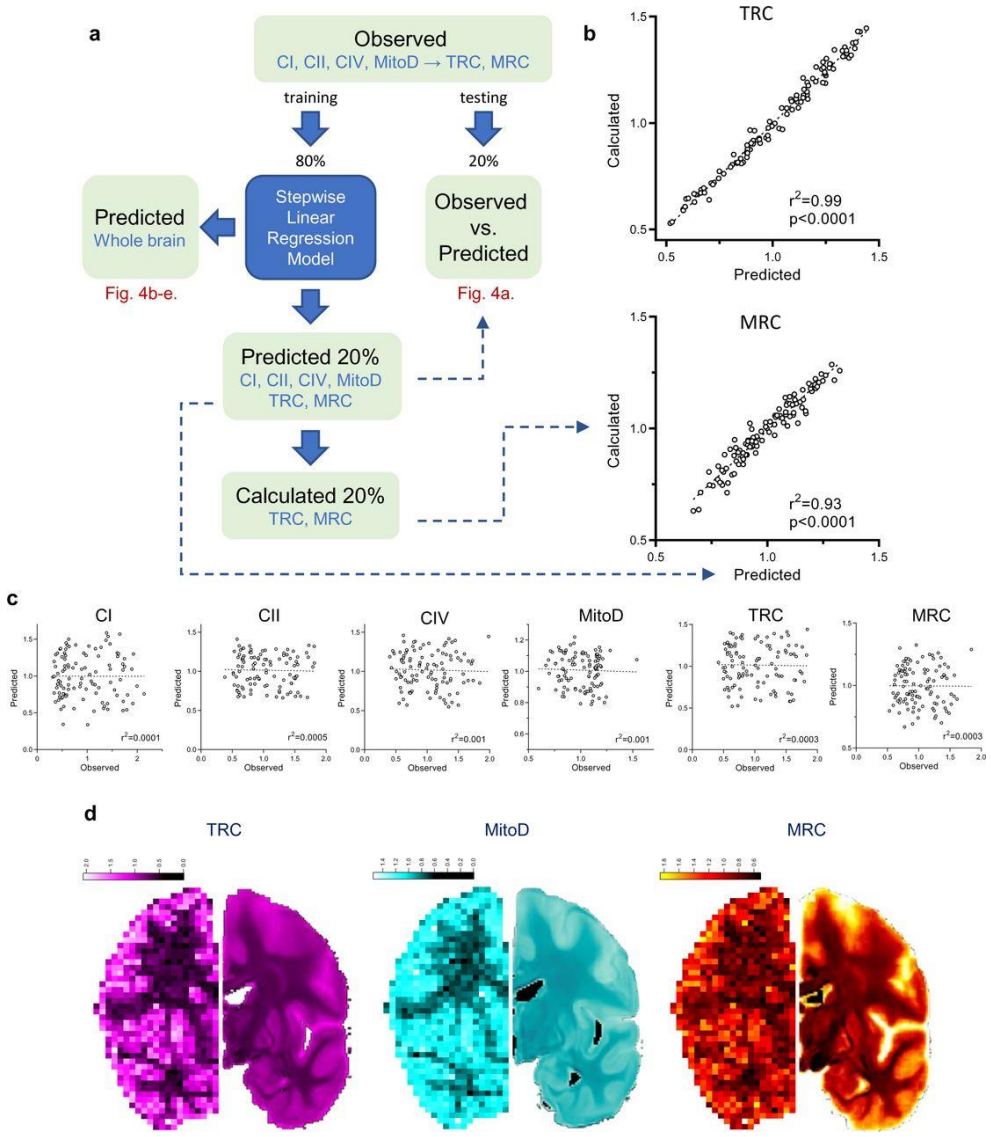

Extended Data Figure 11: Workflow of Data Processing with Stepwise Linear Regression Model

a, Voxels that had all 6 mitochondrial parameters (4 independent and 2 derived) and with a sum of GM and WM probabilities more than 70% (n = 539 'observed' voxels) were randomly split into 80% learning (n = 431) and 20% testing (n = 108) datasets. A model was built by predicting each of the 6 mitochondrial values in the learning dataset using stepwise backward linear regression of neuroimaging values (Extended Data Table 1). The model was then applied to the testing dataset to verify predictions accuracy. Correlation between observed and predicted

values of the testing dataset are shown on Fig. 4a. Next, the predictive models were extended to all the brain voxel of the MNI space to produce a whole brain estimated map for each of the mitochondrial values at 1 mm^3 resolution (Fig. 4b-e). **b,** Correlation between TRC and MRC values either predicted by the model or calculated from predicted CI, CII, CIV and MitoD values (see formulas on Fig. 2c). Strong correlation between predicted and calculated values for TRC and MRC shows the robustness of the model as it's able to accurately predict derived parameters (TRC and MRC) without the knowledge of the independent readouts they were derived from (CI, CII, CIV and MitoD). **c,** Scatterplots of 20% out-of-sample prediction of mitochondrial profiles (same data as on Fig. 4a) after the pairing between observed and predicted values was scrambled. Slopes of all linear regressions are not different from zero ($p>0.7$; Pearson's r^2 is shown on each graph). **d,** Predicted (upper row) vs. observed (lower row, same data as on Fig 2d-f) maps of values for TRC, MitoD and MRC from the same coronal plane. Scale bars are in z-score units.

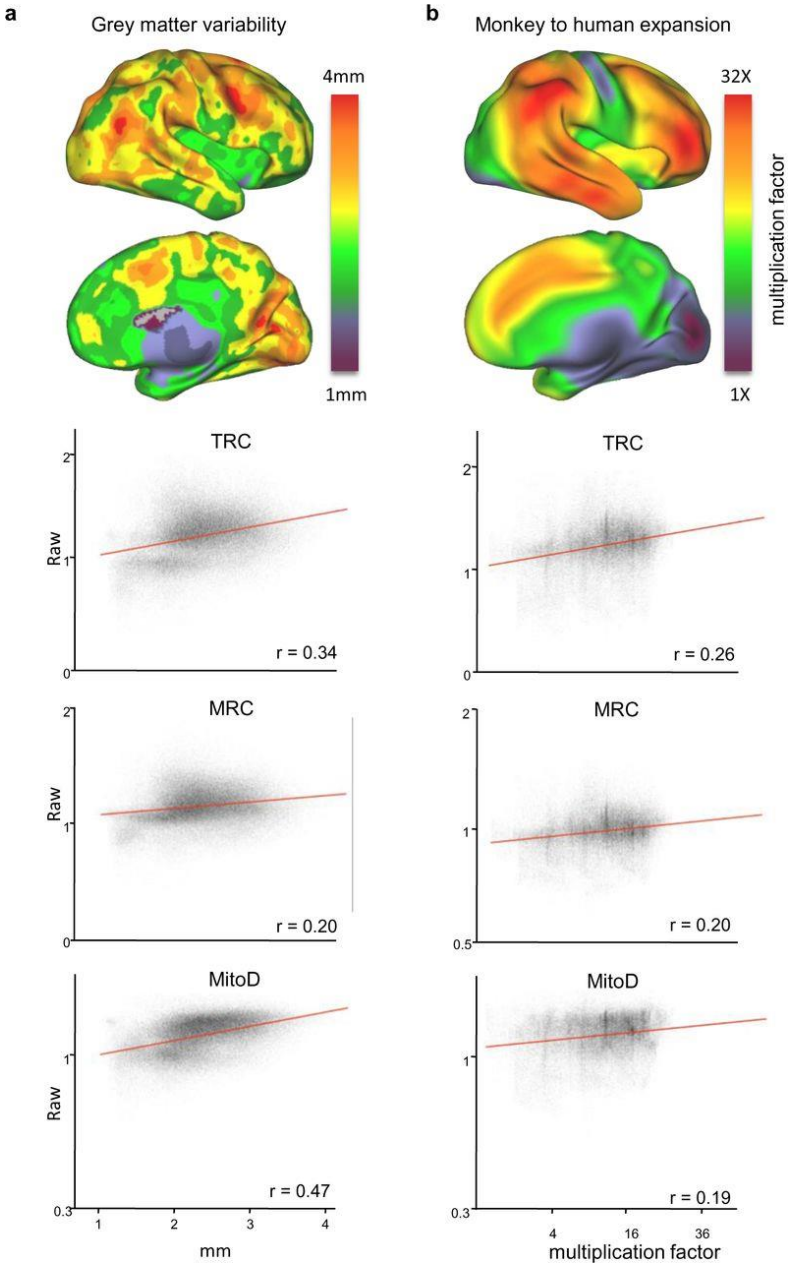

Extended Data Figure 12: Higher Mitochondrial Activity in Phylogenetically Younger Brain Areas

a-b, Comparison between predicted values and indirect measures of brain evolution such as grey matter variability (a) and monkey-to-humans areal expansion (b).

Tables

	Abbreviation	MRI metric	CI	CII	CIV	MitoD	TRC	MRC
Diffusion MRI	AD	axial water diffusivity		.242			.246	
	FA	white matter density			.681	.820		
	RD	radial water diffusivity	-.365		.439	.632		-.175
	StreDensity	streamlines density		-.184				
	ICVF	intra-cellular volume fraction	-.371					
	ISOCF	extra-cellular volume fraction		-.158	-.438	-.445	-.330	
	MD	mean water diffusivity						
	OD	orientation dispersion index (neurite complexity)	.363	.323	.628	.499	.481	.334
Structural MRI	T1W	T1w imaging						
	T2W	T2w imaging	-.245	-.304	-.458	-.410	-.330	-.244
	T1w/T2w	T1w/T2w ratio	-.656	-.580	-.723	-.622	-.617	-.593
	FLAIR	imaging approach to see the anatomy of the brain		-.221		-.339		
	CT	cortical thickness						
	inner_CSA	local surface for inner cortical ribbon						
	plial_CSA	local surface for outer cortical ribbon						
	GM	probability of gray matter	-1.038		-1.382		-1.177	-.939
	WM	probability of white matter	-1.082		-1.263	-.312	-1.040	-.906
Functional MRI	Max_activity	maximum bold derived from fMRI			.380		.333	.501
	Reho	regional homogeneity		.145		.135		
	Entropy	synaptic complexity derived from fMRI			-.386		-.365	-.560
	ALFF	amplitude of Low-Frequency Fluctuation						
	fALFF	ratio between low and and high frequency fluctuations						

Extended Data Table 1: List of neuroimaging metrics and their standardized beta coefficient relationship with the mitochondrial features.

Chapter 3: Performing and Analyzing Large-scale Studies of Seahorse Respirometry Data

Introduction

As discussed in Chapter 2 of this thesis, one of the main limitations to utilizing respirometry in research is its scalability. The current methodologies make generating respirometry data for large cohorts or high-resolution tissue studies prohibitively difficult and time-consuming. As omics-sized data sets become more popular, methodologies need to adapt to be compatible with experiments of this size. With the development of the RIFS assay circumventing the limitations preventing the acquisition of large cohorts for respirometry, we now need new methodologies in congruence with the new sampling cohorts we can assemble. Though RIFS overcomes these challenges to scalability, the largest studies of respiration have assessed between 24 and 96 samples in a “high-throughput” capacity which could still be considered relatively low-throughput compared to many “omics” and screening techniques utilized today (Rogers et al. 2011; Fuchs et al. 2023; Vekaria et al. 2024). Studies with this level of sample numbers can rely on the low throughput experimental planning, normalization, and analysis techniques which are most commonly used for respirometry (Osto et al. 2020; Acin-Perez et al. 2020). If respirometry is a technique which we want to scale with the RIFS platform, new experimental questions and considerations must be made with regard to the planning, technical, and analytical changes required to achieve this type of large scalability.

In Chapter 2 we detailed the multi-institutional effort to assemble a mitochondrial respirometry study which would test the limits of scalability for the RIFS assay. In the study entitled “A Human Brain Map of Mitochondrial Respiratory Capacity and Diversity”, our team sought to map mitochondrial function for a coronal slab of the whole right hemisphere of a neurotypical human male brain (Mosharov et al. 2024). This brain slice was frozen and CNC milled into 703 cubes/voxels of 3mm^3 in size with the intent of assembling a heatmap of

mitochondrial respiratory capacity across an entire slice of a human brain hemisphere at higher resolution than ever before.

Performing respirometry on such a large number of samples, especially when blinded to the sample types, required many novel experimental considerations. These included the planning and plate layouts for this many samples, determining the proper controls for a study of this nature, and the development of automated analysis and quality control protocols to analyze what would turn out to be the largest respirometry study and data set generated to date. In this paper, we will outline the techniques developed for scaling respirometry to a data set of more than 700 samples and 11,000 data points, such that future studies of this scale and larger which incorporate respirometry techniques may gain insight into the considerations required when assessing a sample set of this size.

Main

Mitochondrial research has grown exponentially in the last two decades, and at the forefront of mitochondrial studies are measurements of mitochondrial function, specifically respirometry. Respirometry is the measurement of oxygen consumption rate (OCR) by the mitochondria which occurs through Complex IV of the Electron Transport Chain (ETC). This technique represents the gold-standard of measurements of mitochondrial function for two primary reasons: (1) oxygen consumption is an output for which we have advanced ways of very accurately measuring small changes in the partial pressure of oxygen *in vitro*, and (2) respirometry represents an integrated measurement of energy metabolism, reflecting changes in the energy producing processes which come before the electron transport chain and also the energy consuming processes which result from the tight coupling of the ETC with ATP production. With these considerations in mind, respirometry is a technique which has become a primary building block in the understanding of mitochondrial biology.

Despite being such an integral measurement to understanding whole tissue metabolism and bioenergetics, respirometry has multiple limitations. Notable among these limitations is the necessity for tissue samples to be obtained and processed freshly, within hours of initial access, for respirometry experiments. This limits the scalability of respirometry studies and prevents larger clinical studies from biobanking samples, rerunning samples, or relocating samples to locations with the appropriate expertise and equipment to perform a respirometry study. With this in mind, Acin-Perez et al. (2020) details a novel approach to allow for the measurement of mitochondrial respiration in samples which were previously frozen (Acin-Perez et al. 2020). In short, the freezing and thawing of the mitochondria results in the loss of some of the components required for respiration to occur, the respirometry in previously-frozen samples (RIFS) assay adds back these principal components allowing for the measurement of maximal ETC respiratory activity in tissues, cells, and homogenates (Acin-Perez et al. 2020; Osto et al. 2020). This technique overcomes the necessity for fresh tissue samples and allows for biobanking of large numbers of samples for respirometry measurements, overcoming one of the main factors limiting the scalability of respirometry studies. Though RIFS overcomes these challenges to scalability, the largest studies of respiration have assessed between 24 and 96 samples in a “high-throughput” capacity which could still be considered relatively low-throughput compared to many “omics” and screening techniques utilized today (Rogers et al. 2011; Fuchs et al. 2023; Vekaria et al. 2024). Studies with this level of sample numbers can rely on the low throughput experimental planning, normalization, and analysis techniques which are most commonly used for respirometry (Acin-Perez et al. 2020; Osto et al. 2020). If respirometry is a technique which we want to scale with the RIFS platform, new experimental questions and considerations must be made with regard to the planning, technical, and analytical changes required to achieve this type of large scalability.

With these challenges to scalability in mind, we worked with a multi-institutional team based out of Columbia University and led by Dr. Martin Picard and Dr. Eugene Mosharov to assemble a mitochondrial respirometry study which would test the limits of scalability for the RIFS platform. In the study entitled “A Human Brain Map of Mitochondrial Respiratory Capacity and Diversity”, our team sought to map mitochondrial function for a coronal slab of the whole right hemisphere of a neurotypical human male brain (Mosharov et al. 2024). This brain slice was frozen and CNC milled into 703 cubes/voxels of $3mm^3$ in size with the intent of assembling a heatmap of mitochondrial respiratory capacity across an entire slice of a human brain hemisphere at higher resolution than ever before.

Performing respirometry on such a large number of samples, especially when blinded to the sample types, required many novel experimental considerations. These included the planning and plate layouts for this many samples, determining the proper controls for a study of this nature, and the development of automated analysis and quality control protocols to analyze what would turn out to be the largest respirometry study and data set generated to date. In this paper, we will outline the techniques developed for scaling respirometry to a data set of more than 700 samples and 11,000 data points, such that future studies of this scale and larger which incorporate respirometry techniques may gain insight into the considerations required when assessing a sample set of this size.

Study Details:

The full details of the study are outlined in “A Human Brain Map of Mitochondrial Respiratory Capacity and Diversity” but the details which are applicable to the RIFS study will be outlined here (Mosharov et al. 2024). A postmortem neurotypical brain was obtained from an age 54 male individual and was stored at -80°C for 10 years. The coronal slab of the whole right hemisphere of the brain was CNC milled into 703 voxels of $3mm^3$ in size and manually collected and indexed for the study. Additionally, the 1mm slice trimmed from the brain to clean and prep

the surface was collected for white, mixed, and grey matter controls to be used throughout the study. Each voxel was randomly assigned a new plate number and sample position to blind the sample type and location to those performing the assays. These voxels were weighed and then homogenized using a bead homogenization technique and then plated into sample plates for the RIFS study with 2 grey matter, 2 mixed matter, and 2 white matter controls on each sample plate (Figure 1A). These sample plates were plated into Seahorse sample plates to run the RIFS assay to measure maximal mitochondrial respiration of Complex I, Complex II, and Complex IV for all samples (Figure 1B).

Running the initial 703 voxels, the control samples, and any rerun voxels required 50 XF96 Seahorse runs. Of the initial 703 voxels tested, 60/703 (8.5%) required a rerun for at least one of the ETC complexes assessed. Of the 703 voxels for the study, 633/703 (90.0%) passed all quality control criteria for Complex I, 668/703 (95.0%) passed for Complex II, and 684/703 (97.3%) passed for Complex IV. For Complex I, II, and IV we generated 11,968 data points which passed all acceptance criteria for the study.

Technical Considerations:

Challenges to Think About	Considerations to make before running Seahorse samples	How we handled these challenges
How large is the scale of your experiment?	• How many samples? Are you blinded to the sample type? • How many technical replicates will you need? • What study controls can be used to assess the quality of the data? • Can you run a subset of the samples to test if your process is streamlined?	• Though we were blinded to the type of brain matter we were sampling, brain controls of grey, white, and mixed matter were pretested to determine the feasibility of the project. • Technical duplicates were sufficient for this project. • Pretesting allowed us to streamline the experimental process to convert single-channel techniques into fewer multi-channel pipettes.
Are your samples going to be energetically similar?	• How will you normalize sample concentration? • Can you load your plates with a multi-channel? • How will your choice effect your data at the end of the study?	• Pretesting determined that normalization to total protein could be performed after loading to a normalized volume, thereby streamlining the sample loading process. • This decision did require later quality control metrics to correct for potential artifacts.
How will you run these samples?	• How many instruments do you have access to? • How can you minimize freeze-thaw cycles and the time samples are left at room temperature? • How will the data look when you finish?	• Instrument availability allowed us to run multiple Seahorse runs in a day while keeping the sample plate on ice for a minimal amount of time. • Maintaining consistent plate loading across all runs allowed for easier data handling when consolidating all of the data.

Seahorse experiments rely on multiple technical considerations to ensure that samples run consistently and within the signal to noise of the instrument. While factors like sample normalization, sample loading, and the choice of controls and plate layouts are of minimal concern with tens of samples and one or two Seahorse runs, they become much greater hurdles when scaling to hundreds of samples and tens of Seahorse runs. This section will detail how we handled the scaling of these technical limitations, mainly the normalization of large numbers of blinded respirometry samples, our choices of control samples, and our choice of plate layouts for this study.

Normalization to Tissue Content:

Previous studies measuring mitochondrial activity in the brain have shown that grey matter and white matter differ greatly with regard to mitochondrial energetics (Rosenberg et al. 2023; Fecher et al. 2019; Tomasi, Wang, and Volkow 2013; He et al. 2022). While in a typical respirometry experiment, you could normalize the white matter, grey matter, and mixed matter

separately so that they all will have activity levels which are within the signal to noise of the Seahorse platform (as shown in Figure 2A), this is not feasible in a sample set of this scale. Using a single channel to separately load every sample at different volumes for normalization could take hours per Seahorse plate, not to mention that these samples are blinded to the operator and therefore we could not identify the brain matter type before each assay. To overcome this technical hurdle, we ran pre-testing normalization experiments (Figure 2B-D) to determine if loading using a single volume of sample and normalizing to protein content after the respirometry run would be viable for our different sample types.

In Figure 2B we see the respirometry traces of grey matter control samples ran at 10, 15, and 20µL. At 20µL of sample we begin to observe artifacts representative of a respirometry sample which has been loaded at too high of a concentration. After TMPD/Ascorbate injection we observe an expected increase in OCR consistent with an increase in sample concentration, but at the second measurement we see that this increased OCR is not sustained. Taking a closer look at the oxygen levels within the wells of these samples (Figure 2C), you can see that at 20µL of sample we are depleting oxygen too rapidly, resulting in a phenomenon known as “J-curving” (discussed in Osto et al., 2020 troubleshooting of the RIFS assay) (Osto et al. 2020). This data showcases the potential problems associated with loading respirometry samples at too high of a concentration and reveals that 20µL of tissue will be too large for this study.

In Figure 2D we see the respirometry traces of white matter control samples ran at 10, 15, and 20µL. With these lower oxygen consuming samples we observe the opposite trend, where at 15 and 20µL our traces are sensitive to our mitochondrial substrates and inhibitors, but at 10µL we see a significant amount of noise in the form of decreased reproducibility of technical replicates and unstable responses to injection compounds.

Based on these pre-testing experiments we decided to run all samples at 15µL. At this concentration the white matter samples remained sensitive to all compounds and could be

accurately detected, while the grey matter samples did not show any sign of consuming too much oxygen. While normalization via this technique worked very well for the large majority of samples in this study, it must be noted that this system only works in tandem with a quality control system for the data which can identify samples with OCR values below the detection of the Seahorse assay so that they may be reran. We will discuss how we dealt with these types of samples in the Analytical Considerations section of this document.

Control Samples:

For a study of this size, control sample selection was highly important to not only assess run performance, but also to later determine appropriate quality control criteria. Included on each run were background wells for the Seahorse to normalize against, brain matter controls (2 grey, 2 mixed, and 2 white), and mitochondrial controls. The following section 'Planning and Plate Layouts' will discuss how these controls were arranged onto every Seahorse plate. The brain matter controls were made from the 1mm slice of brain which was CNC milled to clean and prep the brain hemisphere for the voxelization process, providing material which is virtually identical to the voxels used as our sample material for the study. The brain matter controls serve to indicate at the high, medium, and low oxygen consumption levels that the assay is working properly and that the measurements are within the signal to noise of the Seahorse platform. The mitochondrial controls are crude isolations of liver mitochondria from mice (Osto et al. 2020) which were aliquoted for this study so that all aliquots had the same number of freeze-thaw cycles. These controls work very well on the RIFS platform and provide proof that the Seahorse compounds are measurement cycles are working properly for each run.

Planning and Plate Layouts:

While typical respirometry or RIFS experiments utilize only 1 or 2 Seahorse XF96 sample plates, this study's 703 samples across 8 sample plates which need to be assessed for ETC Complex I, Complex II, and Complex IV required a more nuanced and organized plate

layout strategy. Figure 3 depicts the plate layouts that we utilized for this study. Each plate of samples from the study location is labeled as a “Sample Plate”; the 703 samples plus controls utilized in the study came in 8 separate 96 well Sample Plates. Samples within each Sample Plate were then labeled 1-96 with grey matter controls at positions 1 and 96, mixed matter controls at positions 8 and 44, and white matter controls at positions 45 and 89 (these control locations represent the four corners and the center of each Sample Plate).

For clarity in the terminology used in this paper, plates containing the brain samples from the study will be labeled as a “Sample Plate”. Plates created for the purpose of loading into the Seahorse for a respirometry experiment will be referred to as a “Seahorse Plate”.

Our plate layouts for this study needed to consider these criteria: all samples needed to be ran in duplicate; all Seahorse sample plates needed to include all 6 of the study controls, 4 mitochondrial Seahorse controls, and background calibration wells; all samples needed to be ran for the Complex I/Complex IV assay as well as the Complex II/Complex IV assay; and the layout must be designed to load our samples using a multichannel pipette. Figure 3 depicts the plate layout used for the study which satisfied all of our conditions. Seahorse plates 1 and 2 are dedicated for the Complex I/Complex IV assay, Seahorse plates 3 and 4 are dedicated for the Complex II/ Complex IV assay, and Seahorse plate 5 has half of the plate dedicated to Complex I/Complex IV and the other half of the plate dedicated to Complex II/Complex IV. Samples 9-48 were ran on Seahorse plates 1 and 3 in duplicate, samples 49-88 were ran on Seahorse plate 2 and 4 in duplicate, and samples 1-8 and 89-96 were ran on Seahorse plate 5 in duplicate. Control samples (6 brain controls, 4 mitochondrial controls, and background wells) were put in columns 1 and 12 of each Seahorse plate. If a control sample was included in the sample set of that Seahorse plate (e.g.: sample 44 of each sample plate was a brain control sample) then that sample was excluded from columns 1 or 12 of the Seahorse plate since it would be run elsewhere on that plate. Using this plating format, all samples for 1 Sample plate could be split

into 5 Seahorse plates such that they are ran in duplicate with all requisite controls for all desired ETC complexes.

Analytical Considerations:

Challenges to Think About	Considerations to make before running Seahorse Samples	How we handled these challenges
How will you get your data off of the Seahorse in an organized and consistent way?	• Consider an automated spreadsheet where the Seahorse data can be directly copied and pasted which can organize your data identically for all runs (including any calculations you want to look at). • Consider automated spreadsheets to consolidate multiple Seahorse runs into a consistent format. • Consider providing each sample with a unique identifier to track its progress through the analysis methods.	• Our automated spreadsheets converted the data coming directly from the Seahorse into a consistent and organized plate layout. This layout could then be placed in a second automated spreadsheet to consolidate the multiple Seahorse runs for each sample plate into a single organized block for later quality control analysis. • Each sample was provided with an identifier with the plate number and well coordinate within that plate.
How can you automate quality control for these samples? What trends do you see in the data?	• Look at random assortments of samples and observe any trends in your data (both good and bad). • Are your samples near the Seahorse lower limit of detection? Consider a low OCR threshold. • Are you samples near the Seahorse upper limit of detection? Consider an upper OCR threshold or J-curve detection method.	• Control samples ran on every plate were analyzed manually to observe trends within the data and to establish a lower limit of detection for the brain samples ran. • Samples near the lower limit of detection were detected using a minimum OCR threshold for samples. Samples not meeting this threshold were designated to be rerun with more sample input.
What acceptance criteria should I apply to the data?	• How well did your control samples perform? Is your quality control procedure accurately eliminating poorly performing samples? • How many of your technical replicates per sample are performing properly?	• We observed in our study that some samples had lower Complex IV capacity than Complex I/II capacity, to combat this we incorporated a second quality control metric for minimum Complex IV capacity. • We decided that an accepted sample must have at least one accepted Complex I data point, one Complex II data point, and two Complex IV data points.
What samples should I rerun?	• Which samples were near the Seahorse limit of detection? • Which samples were inconsistent across technical replicates? • How are you compiling and running these samples?	• Samples which did not pass either quality control metric were rerun at a higher sample volume for either Complex I/IV only, Complex II/IV, or both depending on which criteria did not pass.

Typical Seahorse runs may have between 16 to 96 samples, and while it may take a bit of time, analysis and quality control practices are normally done on a sample-by-sample basis. With these lower throughput experiments an operator can look at each Seahorse trace

individually to assess wells which may not have injected properly or technical replicates which did not perform very similarly and exclude them from the final analysis on this basis. With the hundreds of samples in this study, looking at every sample and control was not feasible, and with this in mind we had to create novel automated methods and quality control metrics to deal with the immense amount of data generated in this project in a high-throughput manner.

Analysis of RIFS Seahorse Data:

The details for analyzing a Seahorse trace or a RIFS experiment are detailed in Osto et al. (2020), this document will cover the considerations and optimizations we made to analyze a Seahorse data set of this size in a high-throughput manner. In short, three parameters must be measured for each sample: Complex I driven respiratory capacity (NADH stimulated OCR – Antimycin A stimulated OCR), Complex II driven respiratory capacity (Succinate/Rotenone stimulated OCR- Antimycin A stimulated OCR), and Complex IV driven respiratory capacity (TMPD/Ascorbate stimulated OCR – Azide stimulated OCR). These values represent the ETC complex maximal respiratory activities which can then be normalized to protein content to achieve a normalized maximal respiratory capacity with the units (pmol O_2/min)/μg protein. Figure 4A showcases a Seahorse trace for one of the samples in our study assessing Complex I and Complex IV, visually highlighting the measurements used in our study.

Automated Data Handling, Calculations, and Organization:

To prevent possible user errors when handling and analyzing the Seahorse data and to keep the data in an organized format, an automated Excel worksheet was created to transform the Normalized Rate Data coming from the Seahorse instrument into a universal format which would be applied to all runs. In short, the BCA (total protein) normalization data for each sample was added to the Seahorse data using the normalization tools within the Agilent Wave Seahorse Analysis Software. From the Wave software, each run was exported as an Excel document which provides the run data in multiple sheets, one of which labeled “Normalized Rate (Plates)”

which provides the normalized OCR of each well for every measurement cycle of the Seahorse. Measurement data could then be copied and pasted into the “Automated SH Plate Analysis” Excel worksheet we created. When this is done, the data automatically fills into the accompanying tables where the following are calculated: average baseline OCR, average 1st injection OCR, average Antimycin A OCR, average TMPD OCR, average Azide OCR, Injection OCR-AA OCR, TMPD OCR-Azide OCR, and the difference between the two technical replicates for the Injection OCR-AA OCR and TMPD OCR-Azide OCR values. The average normalized OCR measurement calculations consolidate the multiple measurements made after each injection into one average measurement in the case that a reading is not consistent. The Injection OCR-AA OCR and TMPD OCR-Azide OCR calculations automatically determine the Complex I/II driven respiratory capacity (depending on the injection used for that plate) and the Complex IV driven respiratory capacity respectively. Additionally, these metrics are collated into two tables which in isolation can provide quick information regarding the performance of a single plate. These two tables can also be copied and pasted into the “5 Plate to Column Analysis” worksheet which consolidates the data from the 5 Seahorse runs of a single sample plate into 8 columns which detail every calculated metric for each Seahorse trace. These tools allow each Seahorse run to be analyzed and organized in an identical manner, making later interpretation and analysis of the data much easier.

Establishing our Quality Control Parameters:

High-throughput respirometry studies cannot afford to look at every single data point individually to assess whether a sample should or should not be accepted for the study due to technical issues. With this in mind, for this study we had to come up with our own parameters which could detect a Seahorse trace which was abnormal. This section will detail these parameters and our justification for including them in our study.

Oxygen Consumption Rate Thresholding- Low OCR Threshold:

As was described in the previous section of this paper ‘Normalization to Tissue Content’, while loading all samples at equivalent volume for the Seahorse runs was the most feasible method to achieve higher throughput, it meant that lower OCR samples would be near the limit of detection of the Seahorse platform. With this in mind, we needed to create a minimum threshold of OCR/µg which samples would have to meet. Any sample which did not meet this criteria was placed in a list to be rerun, but at a larger volume (and therefore higher protein concentration) to provide it with an opportunity to perform within the signal to noise of the Seahorse platform on its rerun.

We established this threshold measurement using the brain control samples ran on every Seahorse run of the study. A flowchart of the decisions made in establishing these OCR threshold values is outlined in Figure 5A. We began by manually looking at every control sample trace to subjectively determine if the control sample did or did not perform reliably on the Seahorse. If all manually selected traces were excluded from the study, we calculated an average OCR of 0.88 with a standard deviation of 0.26 (Figure 5C). The provided us with a minimum expected threshold of [0.88 – 2*(0.26)] which equals an expected threshold of 0.36 OCR/µg. While we could have chosen 0.36 OCR/µg as our threshold, we found that this value was not selective enough, leaving some manually determined poor performing samples in the data set. We decided to slowly increase the quality control threshold from the 0.36 OCR/µg value until two criteria were met for all white matter control traces: our population of controls fell within the 95% confidence interval of expected standard deviation as calculated by linear regression of the other brain matter controls used in the study and our manually excluded samples were all excluded (Figure 5B).

Given that rerunning these samples was not of huge inconvenience we increased the threshold to 0.5 OCR/µg to be cautious with the data set and rerun more samples. Following a similar method, we determined a similar threshold for Complex IV (TMPD-Azide). Our final OCR

thresholds were the following: Complex I and Complex II samples must be greater than 0.5 pmol O_2/µg protein and Complex IV samples must be greater than 1.5 pmol O_2/µg protein. Figure 4B-D showcase example Seahorse traces from the study set which did not pass the Complex I, Complex II, or Complex IV OCR threshold values and were therefore excluded or reran for the study based on the final study inclusion criteria described below.

Oxygen Consumption Rate Thresholding- TMPD Accommodation:

After initial analysis of the data and manual observations of assorted sample traces, we observed that certain samples would have valid Complex I or Complex II values, but the subsequent Complex IV measurement would be lower by comparison. Given the sequential nature of the Seahorse assay and the fact that stimulation of Complex I or II is measuring OCR of Complex IV, it should not be possible for a sample to have a higher OCR for Complex I or II than it has for Complex IV. However, there are a few technical reasons this might occur: the TMPD/Ascorbate injection (Complex IV substrate) may not have injected properly for these samples; there may be some sample material lifting from the plate during the time-course of the Seahorse experiment; or, given that many samples which exhibited this phenomenon had higher OCR values, this may be a result of slight J-curving from excess oxygen depletion from the Seahorse well. Regardless of the reason, we required an automated method of identifying these types of samples for rerunning or exclusion from the study. After looking through a selection of samples and grey matter brain controls which exhibited this phenomenon, we decided that the Complex IV OCR value must be at least 80% of its respective Complex I or Complex II OCR value. Figure 4E showcases an example Seahorse trace from the study which did not meet the TMPD accommodation criteria. Any sample not meeting this criterion was either excluded from the study or rerun based on the final study inclusion criteria described below.

Study Inclusion Criteria and Management of Sample Reruns:

With the two quality control measures in place (Low OCR threshold and TMPD Accommodation) each trace was analyzed individually from its technical duplicate. Each trace was first analyzed via the low OCR threshold and provided with a Pass or Fail for Complexes I, II, and IV. At this point, the passes and fails were tallied; if a sample had at least one passing Complex I measurement, one passing Complex II measurement, and two passing Complex IV measurements, then the sample was accepted to the study and did not require a rerun. Any sample which did not meet this criteria was placed into one of four categories depending on what quality control criteria did not pass: Only Complex I failure, Only Complex II failure, Complex I and Complex II Failure, or Only Complex IV failure. These samples were then accordingly binned for future reruns where Only Complex I and Only Complex II failures would only need to be reran for their respective failing complex, Only Complex IV failures would be run for Complex I/IV since Complex I values are typically more prone to failure and would benefit more for additional replicates, and Complex I and Complex II failures would have to be reran for both complexes.

Rerun samples were manually assigned to a Rerun Sample Plate Layout and ran (as discussed previously) at a higher loading volume than in the first runs, 25µL for reruns rather than 15µL. These samples were analyzed using a new low OCR threshold of 0.3 pmol O_2/µg protein made identically to the threshold discussed in the “Oxygen Consumption Rate Thresholding- Low OCR Threshold” section above. If the rerun data provided increased the number of successful measurements such that a sample now meets the acceptance criteria of one passing Complex I measurement, one passing Complex II measurement, and two passing Complex IV measurements then this data could now be included in our study.

This quality control process including the inclusion of rerun samples, is showcased in the excel worksheet entitled “Plate 4 Data QC Filtering”. In this worksheet, all samples from Sample Plate 4 of our study set are first marked for whether they pass or fail our OCR threshold criteria.

If they pass this criterion, they are then assessed to determine if they pass the TMPD Accommodation Threshold. If at this stage a sample passes our study inclusion criteria then that sample is not rerun. If at this stage a sample is does not pass our study inclusion criteria for either Complex I, Complex II, or Complex IV then they are reran using the appropriate assay and the rerun data is added into the study set using each sample's unique study identifier. After all original data and rerun data are included into the study set and have passed all quality control metrics, then final study inclusion assessments can be made to determine the final data to be used for the study.

Discussion:

This document describes many of the considerations and challenges we faced in producing and analyzing a first-of-its-kind high-throughput respirometry data set. While we have attempted to make the considerations of this study universally applicable, some of the choices made during the study were bespoke to our study set. For example, our automated analysis sheets are designed to work with the mix/measure protocol used specifically in this study. While our spreadsheets could be easily adapted to other experimental settings, these adjustments would still have to be made to be adapted to your study. This becomes especially applicable with regard to our acceptance criteria, which largely was made based on the trends that we observed after running and analyzing our data. While we have outlined the tendencies in our data and the analysis choices we made in response, we would recommend that researchers look for the potential signs which are indicative of suboptimal respirometry data (e.g.: the troubleshooting sections of Osto et al.) and to look at a random assortment of data points within your study to determine if these phenomena exist and if so, how to detect and handle these events in an unbiased way.

One of the most important notes in a study of this size is to prepare, test, and practice your protocols as much as possible before running the entire sample set. From our experience

in this study, we found that many of the considerations which became vital to the success of the study, like loading by volume rather than protein concentration and finding a plate map which would allow all of our samples to be loaded using a multichannel pipette, were first found when doing our initial pretesting experiments. Assuming that your sample material is not limited or precious, we strongly advise performing some small-scale experiments and analyses before expanding to a sample set of hundreds of samples.

Our laboratory has the benefit of having multiple Seahorse XF96 instruments which we could utilize at the same time to reduce the number of freeze-thaw cycles on the samples during this study. For labs without access like this, extra considerations may need to be made to the number of samples which can be run with consideration to sample integrity throughout the study, with potential acceptance criteria for samples which may have experienced protein degradation throughout the course of testing.

One analytical consideration we chose to not include in this study was the analysis of multiple measurements between each compound injection. This decision was based on the fact that we did not observe many samples which had unstable data across the multiple measurements after each injection and inclusion of another quality control metric to identify these samples would have had very minimal impact to the final data set. To account for this, future studies could include an OCR over time slope for replicate data points to analyze samples which are not identical across multiple measurements, or a delta across measurements which could identify these types of samples for possible rerun or exclusion from the study.

As respirometry becomes a more important and accessible assay in the mitochondrial research field, we will soon need the resources and expertise to perform and analyze larger and larger respirometry experiments and data sets. Using this unprecedented study set, we hope that this document will provide future researchers with the experimental considerations,

procedural knowledge, and analytical framework to execute respirometry studies of this magnitude.

Figures

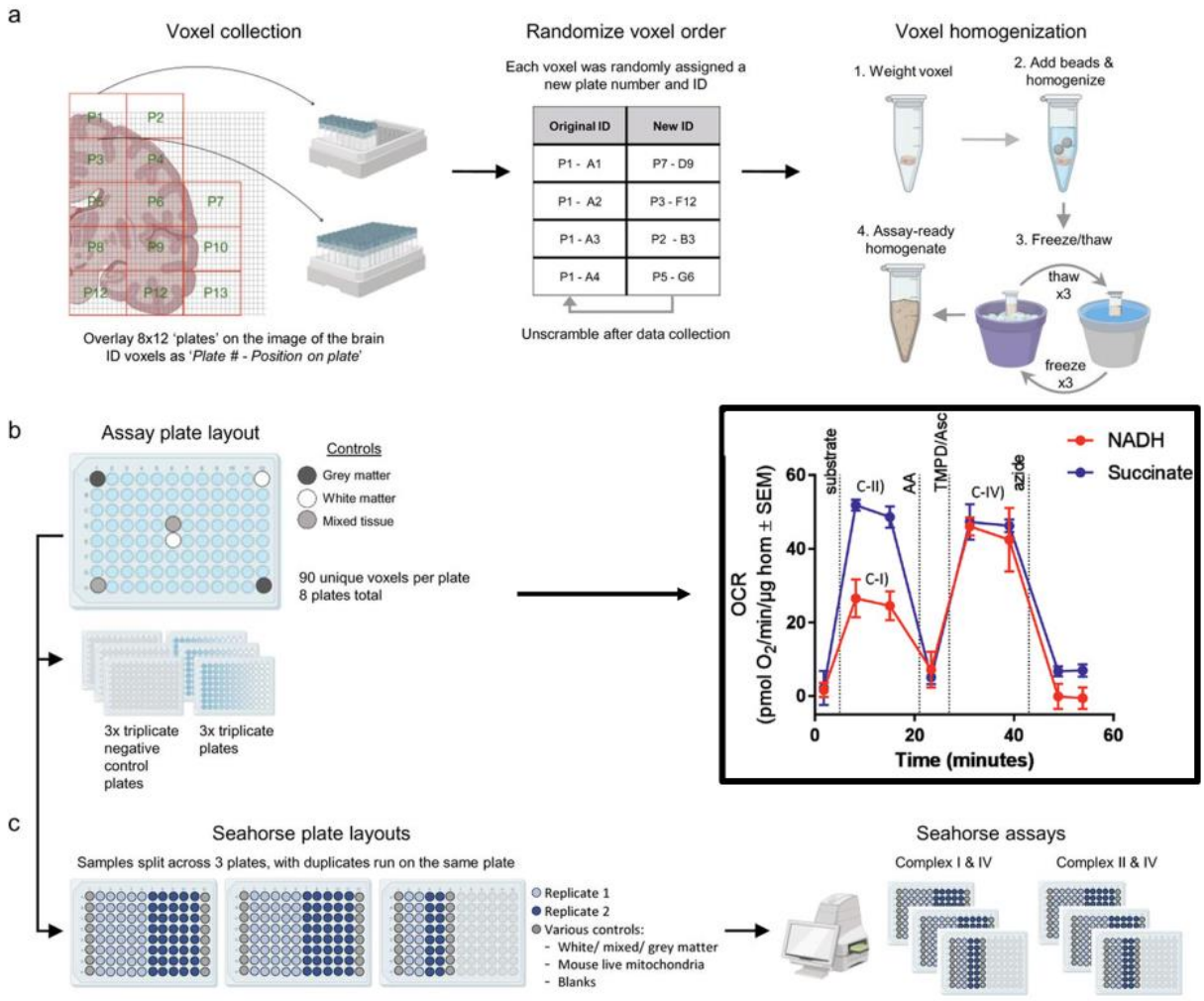

Figure 1: Flowchart of Brain Sample Collection and Respirometry Workflow (Adapted from Mosharov et al. 2024 and Osto et al. 2020)

a) Brain voxels were collected and randomly assigned a plate number and identification number for tracking throughout the study. These samples were bead homogenized and plated into multiple sets of “daughter plates”, one of which was used for the respirometry described in this paper. (b) Plates containing the brain samples were aliquoted into Seahorse respirometry

sample plates and ran using the RIFS protocol assessing ETC Complex I, II, and IV maximal capacity.

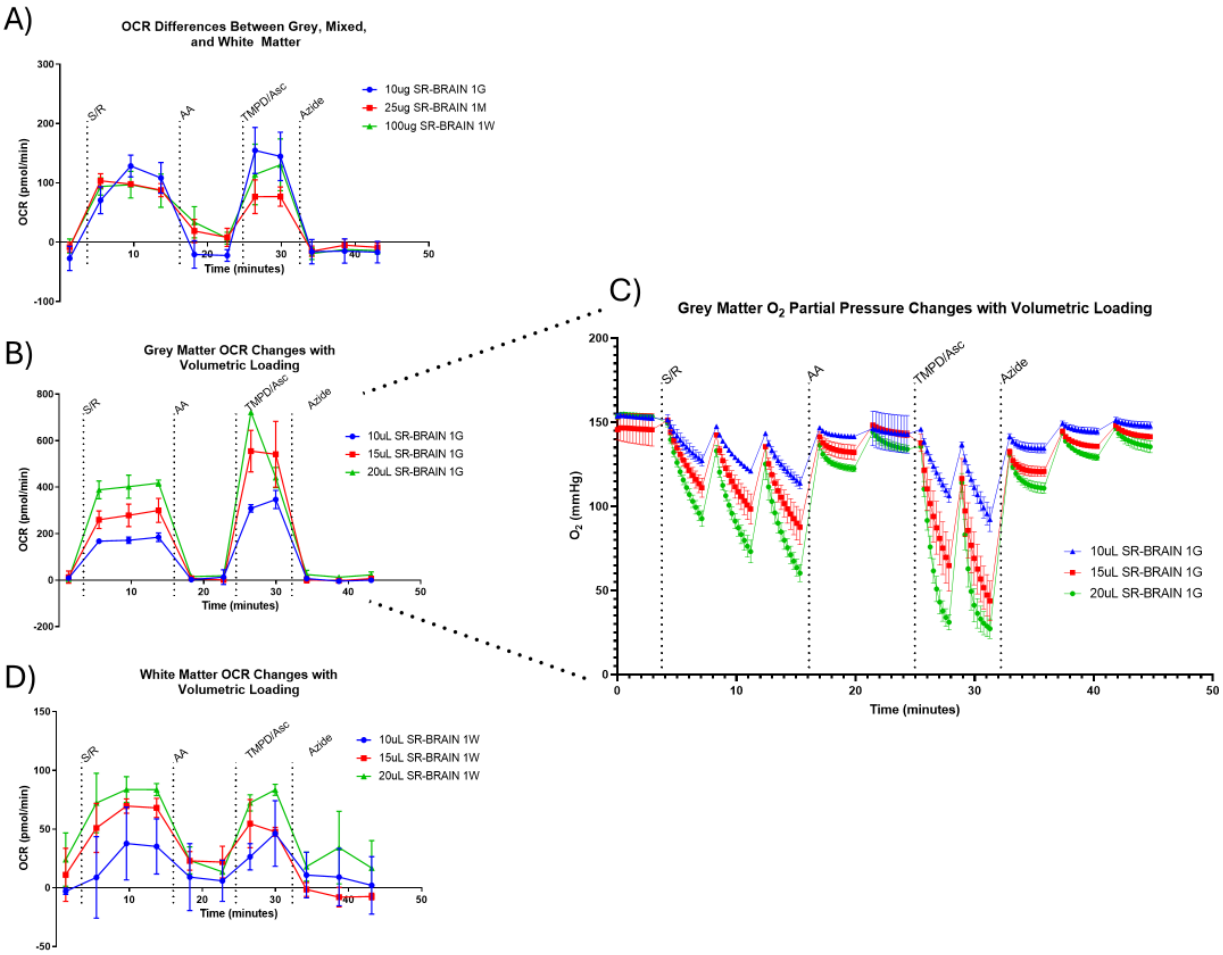

Figure 2: Sample Normalization by Volume is a Viable Technique for High-throughput Respirometry Using Energetically Different Sample Tissues

(a) Grey brain matter (blue), white brain matter (green), and mixed brain matter controls (red) were ran using the traditional loading method of normalizing total protein loading to result in approximately equivalent OCR. Grey matter loaded at 10µg, mixed matter loaded at 25µg, and white matter loaded at 100µg show similar OCR in this experiment. Though this method assures that all samples will run within the signal to noise of the Seahorse instrument, it requires loading samples individually and knowing the sample type, two factors which are not feasible in a blinded study of this magnitude. (b) Grey matter brain controls are run at differential volume

rather than differential protein (10µL, 15µL, and 20µL). While 10µL and 15µL loading has no artifacts, at 20µL we observe inconsistency of the TMPD/Asc measurements indicative of sample overloading. (c) Oxygen partial pressure trace of the respirometry results described in (b). At 20µL we observe “J-curving”, an artifact of sample overloading where excessive oxygen consumption is preventing proper re-equilibration of oxygen levels within the Seahorse well. (d) White matter brain controls are run at differential volume rather than differential protein (10µL, 15µL, and 20µL). While 15µL and 20µL loading has no artifacts, at 10µL we observe decreased sample reproducibility indicative of being below the signal-to-noise of the Seahorse instrument.

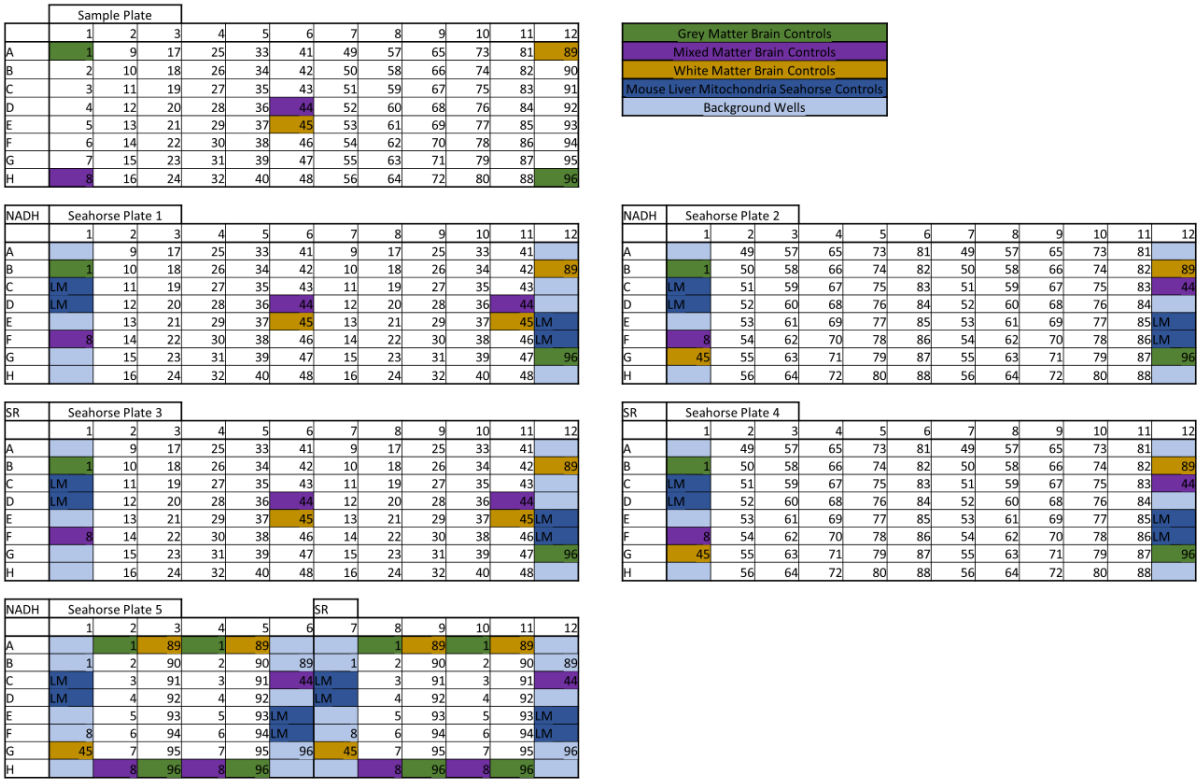

Figure 3: Plate Layouts Utilized for High-throughput Respirometry- Transitioning from a Single Sample Plate to 5 Seahorse Plates

These were the plate layouts utilized to run all of our Seahorse experiments in this study. The “Sample Plate” in the upper right shows one of the “daughter plates” containing 96 of the brain samples for our study including the plate positions of grey, white, and mixed matter controls

across the plate. One of these sample plates was split into five Seahorse run plates for respirometry. Seahorse Plates 1 and 2 were dedicated to the Complex I/Complex IV RIFS protocol, plates 3 and 4 were dedicated to the Complex II/Complex IV RIFS protocol, and plate 5 is half Complex I/Complex IV and half Complex II/Complex IV. Samples 9-48 from the Sample plate were run on Seahorse plates 1 and 3 in duplicate, samples 49-88 were run on Seahorse plates 2 and 4 in duplicate, and samples 1-8 and 89-96 were run on Seahorse plate 5 in duplicate. Control samples (6 brain controls, 4 mitochondrial controls, and background wells) were put in columns 1 and 12 of each Seahorse plate. If a control sample was included in the sample set of that Seahorse plate (e.g.: sample 44 of each sample plate was a brain control sample) then that sample was excluded from columns 1 or 12 of the Seahorse plate since it would be run elsewhere on that plate. Using this plating format, all samples for 1 Sample plate could be split into 5 Seahorse plates such that they are ran in duplicate with all requisite controls for all desired ETC complexes.

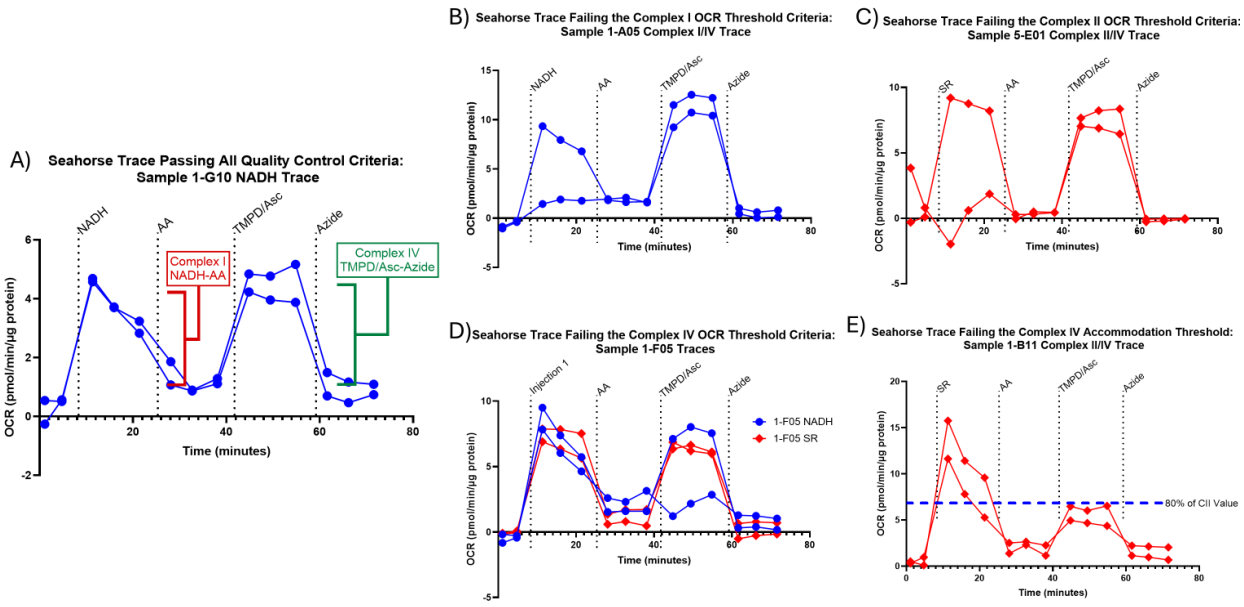

Figure 4: Example Seahorse Trace Which Did Not Pass Our Analytical Quality Control Thresholds

(a) Seahorse traces from a brain sample which passed all quality control criteria for our study. (b) Seahorse traces from a brain sample which failed our Complex I OCR threshold with one trace exhibiting a Complex I value less than 0.5 pmol/min/µg. (c) Seahorse traces from a brain sample which failed our Complex II OCR threshold with one trace exhibiting a Complex II value less than 0.5 pmol/min/µg. (d) Seahorse traces from a brain sample which failed our Complex IV OCR threshold with one trace exhibiting a Complex IV value less than 1.5 pmol/min/µg. (e) Seahorse traces from a brain sample which failed our TMPD Accommodation threshold with both traces exhibiting Complex IV values less than 80% the value of their respective Complex II values.

A)

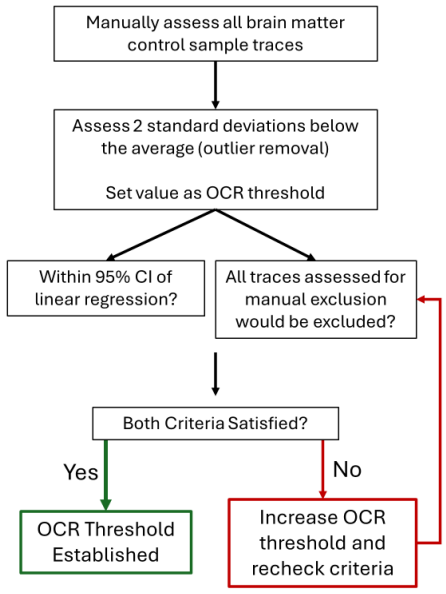

B)

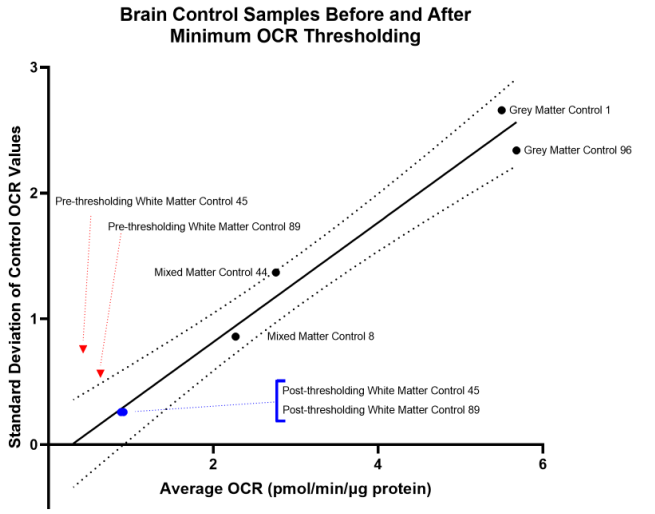

C)

		Average OCR Before Manual Exclusion (pmol O_2/min/µg protein)	Standard Deviation	Average OCR After Manual Exclusion (pmol O_2/min/µg protein)	Standard Deviation
White Matter Control 45	NADH-AA (Complex I)	0.42	0.76	0.91	0.26
White Matter Control 89	NADH-AA (Complex I)	0.63	0.56	0.88	0.26
White Matter Control 45	SR-AA (Complex II)	0.65	0.76	1.18	0.50
White Matter Control 89	SR-AA (Complex II)	0.82	0.52	1.11	0.33
White Matter Control 45	TMPD-Azide (Complex IV)	1.59	1.06	2.50	0.64
White Matter Control 89	TMPD-Azide (Complex IV)	1.55	0.79	2.20	0.55

Figure 5: Flowchart and Considerations Made to Establish Oxygen Consumption Quality Control Thresholds

(a) A flowchart overviewing our decision-making process when selecting an appropriate OCR threshold. We first manually assessed all brain matter control samples to determine which should not be included in the study. We assessed via outlier removal methods that an appropriate starting point would be approximately 0.36 pmol/min/µg, but setting the threshold at

this level did not meet our criteria that the controls must be within the 95% linear regression of variance and must exclude all traces which would have been excluded by manual selection. This process led us to final OCR thresholds of 0.5 pmol/min/µg for Complex I and II and 1.5 pmol/min/µg for Complex IV. (b) Assessing the variance across our brain matter controls compared to their average OCR levels. The filled line indicates the linear regression of the control samples while the dotted line plots the 95% confidence interval of that linear regression. Before threshold application (red) our two white matter controls were outside of this 95% confidence interval, while after quality control using this threshold our controls now result near our linear regression line. (c) A table showing the changes in average OCR and standard deviation of the white matter control samples before and after manual thresholding assessment.

Sample Data and Automated Spreadsheets and Calculation Sheets

In this chapter references are made to excel worksheets containing automated calculation sheets and example data. These will be attached to this thesis in the form of an Excel notebook with appropriately labeled worksheets.

Chapter 4: Salivary Cells as a Non-invasive Biomarker to Assess Mitochondrial Respirometry in Human Subjects

Introduction

Mitochondria, once regarded as simple ATP batteries, are now understood to have a multifaceted role in metabolic adaptation and signal transduction within the cell. Mitochondrial dysfunction contributes to a wide variety of disease states, including cardiovascular, neurodegenerative, and autoimmune disorders (Lopes et al. 2022; Billingham et al. 2022; Poznyak et al. 2020). Despite an expanding understanding of the role of mitochondria in disease, clinicians lack feasible diagnostics to assess mitochondrial function, ultimately limiting the translational utility of the many advances in mitochondrial biology.

Countless techniques have been developed to measure and observe mitochondria. At the forefront of these techniques is mitochondrial respirometry, the measurement of oxygen consumption by the electron transport chain (ETC). Oxygen consumption occurs at Complex IV of the ETC. As oxygen consumption is coupled with the activity of Complex V (ATP Synthase) and substrate oxidation pathways, OCR responds to upstream changes in ETC function *and* downstream changes in energy utilization. Because it provides an integrated measurement of metabolic activity and mitochondrial function, respirometry is one of the gold standards for mitochondrial measurement (Divakaruni and Jastroch 2022).

While respirometry is an effective technique for cell and animal models, its utility in human specimen is hampered by two major limitations: human samples must be acquired using invasive tissue biopsies, and these samples for respirometry must be processed and run within hours of acquisition on specialized and complex equipment. Together, these challenges make the adoption of respirometry measurements for human specimens painful, expensive, difficult to scale, and largely inaccessible for most clinical laboratories.

Recent methodological breakthroughs have mitigated the requirement for fresh tissue for respirometry. Described in Acin-Perez et al. (2020) and Osto et al. (2020), the respirometry in previously frozen tissue assay (RIFS assay) allows for measurements of maximal ETC activity from samples which have been previously frozen for storage (Acin-Perez et al. 2020; Osto et al. 2020). Traditional methods require fresh tissue because cytochrome c and essential ETC substrates like NADH and succinate are lost from the inner membrane space as the mitochondrial membranes are ruptured during the freeze-thaw cycle. In the RIFS assay, exogenous cytochrome c and the requisite ETC substrates are added to the sample, allowing the measurement of maximal OCR. The RIFS assay permits samples to be collected at various times and/or locations, then frozen and shipped to locations with the instrumentation and knowledge to perform respirometry. The RIFS methodology is a crucial technical advancement for the adoption of respirometry, overcoming one of the fundamental challenges for clinical utilization.

Though the RIFS assay facilitates clinical respirometry, most methods measure mitochondrial function in skeletal muscle samples. While these samples are advantageous for respirometry due to high mitochondrial content and low heteroplasmy compared to other tissue types, they require highly invasive tissue biopsies to obtain (Acin-Perez et al. 2021). The reliance on primary tissue for respirometry is the most significant barrier to human utilization, though recent research has revealed that primary tissue may not be required to assess mitochondrial dysfunction. Tyrell et al (2016) show that the respirometry profiles of systemic biomarkers, including maximal respiratory capacity, correlate with that of skeletal muscle (Tyrrell et al. 2016). This and subsequent research reveals that metabolic dysfunction is systemic and can therefore be assessed in circulating cells.

Recently, researchers have begun to search for alternative tissues for respirometry, most notably peripheral blood mononucleocytes (PBMCs) isolated from whole blood and cultured

fibroblasts. While both tissue types have shown some promise, they are suboptimal for clinical implementation. Both tissues are difficult to sample, difficult to process, and have limited practical utility as respirometry samples; PBMCs isolated from whole blood are often contaminated with platelets, which distort OCR measurements, and cultured fibroblasts have altered metabolic characteristics compared to fibroblasts *in vivo* (Acin-Perez et al. 2021). With these challenges in mind, we need a respirometry sample that is easy to collect and easy to process.

We have identified that the cellular content in saliva is a sample material which overcomes the challenges of clinical respirometry. Previous research has shown that buccal epithelial cells in the oral cavity conserve mtDNA mutations found in the muscle or blood, suggesting its potential utility as a systemic biomarker of mitochondrial ETC status (Frederiksen et al. 2006). In this paper, we detail the development and troubleshooting of a novel respirometry assay which integrates the RIFS respirometry platform with novel salivary cell sample preparation. We found that salivary leukocytes represent a viable cell type for mitochondrial respiration which is not only easy to sample, but lacks the platelet contamination observed in similar blood-based energetics methods. This assay allows for the measurement of mitochondrial function in humans in a sample type which is easy to obtain and can be obtained repeatedly for time-course based studies, making respirometry in humans more feasible than ever before.

Main

Saliva Contains Two Categories of Cell Types, Both Containing Mitochondria

The cells in saliva have been used as a biomarker for many pathologies, with most studies focused on DNA for genomic or viral tests (Song et al. 2023). While it has been much more niche, some studies have focused on assessing mitochondria in saliva, largely focusing on changes in mitochondrial DNA copy number in saliva and buccal epithelial cells in the mouth

(Frederiksen et al. 2006; Trumpff et al. 2019; 2022). The cellular content in saliva can generally be divided into two cell types: buccal epithelial cells and salivary leukocytes (Theda et al. 2018). The proportions of these two cell types can vary greatly depending on how you sample cells from the mouth; buccal swabs will collect mostly buccal epithelial cells while the collection of whole saliva or a mouthwash collection provides a more heterogeneous population of these two cell types (Figure 1A). These two cell types can be more clearly distinguished using Pap staining. Buccal epithelial cells (top) represent the majority population in saliva and are characterized by a large surface area (50-150μm in diameter), prominent single nuclei showcasing a "fried egg" shape, and distinct colorization of their cytoplasm when Pap stained. Salivary leukocytes (bottom) represent a minority population in saliva and are much smaller in size (5-15μm in diameter) and appear on a Pap stain as purple-stained puncta. At higher magnification, the leukocytes can be further categorized as different types of immune cells like leukocytes, lymphocytes, and segmented cells (Figure 1B). *When referring to these cell types throughout this paper, "**buccal epithelial cells"** and "**salivary leukocytes"** will refer to isolations of those specific cell types. Cell populations from saliva which have not been isolated to separate the two cell types will be referred to as **"whole saliva"** samples.*

While whole saliva has mitochondrial DNA which can be measured and sequenced, the presence of mitochondria and the ETC proteins in these cell types has not been previously measured (Trumpff et al. 2022; Jiang et al. 2005). Shown by both Western blotting for ETC complexes and by fluorescence imaging techniques, we observe that not only are mitochondria and their ETC complexes present, but their mitochondria maintain membrane potential (Figure 2A-B)). These data show that the cells from saliva have mitochondria that contain ETC proteins, and therefore could be a viable candidate for respirometry measurements. While these cells have the components required for respiratory activity, attempts to perform the RIFS protocol on a mixed population of salivary cells with minimal processing resulted in unsuitable respirometry

measurements. Showcased in Figure 2C alongside a control population of mouse liver mitochondria to exhibit what a typical respirometry trace looks like, we observe abnormally high pre-injection oxygen consumption (occurring before injection number 1 of the Seahorse instrument) and minimal response to most of our mitochondrial substrates and inhibitors. While this experiment stresses that some novel processing will be required for respirometry in this cell type, we did observe that our sample strongly responded to azide, an inhibitor of ETC Complex IV. This highlights that the oxygen consumption observed in this experiment is predominantly mitochondrial in nature and is not a result of background or non-mitochondrial oxygen consumption, providing promise that this assay is viable.

Removal of Microbiome from the Salivary Cell Population Reduces Respirometry Artifacts

It is well known that the mouth is home to more than 700 types of bacteria, fungi, and yeast which make up the oral microbiome (Deo and Deshmukh 2019). While bacteria do not have a traditional ETC, there are many alternative sources of oxygen consumption which may interfere with OCR measurements performed by the Seahorse XF96 respirometry instrument (Seahorse in short). Additionally, it is known that many bacteria species are resistant to Antimycin A (ETC Complex III inhibitor), a phenomenon we observed in our preliminary attempts running salivary cells on the Seahorse platform (Figure 2C) (Ramachandran and Gottlieb 1961; Dunn 2023). As described by others, we observed that after staining our cells with DNA stains (DAPI and Hoescht) as per Rudney and Chen (2006), not only are bacteria present, but the oral bacteria often adhere to the exterior of the buccal epithelial cells (Figure 3A) (Rudney and Chen 2006; Griessl et al. 2021; Fox, n.d.). With these factors in mind, we wanted to determine if a reduction of bacterial content in this sample type will improve overall respirometry results.

With these factors in mind, we wanted to determine if a reduction of bacterial content in this sample type will improve overall respirometry results. We first attempted leveraging the large size difference between buccal epithelial cells and bacteria species. Buccal epithelial cells

average between 80-100 μm while bacterial species on average measure at most 5-10 μm. With this in mind, we filtered our sample with a 40μm filter with the intent of keeping the epithelial cells above the filter and most bacteria flowing through the filter. RT-qPCR for bacterial 16S rRNA shows that there is a 2.5-fold decrease in bacterial content between the small size fraction and the large size fraction, supporting our hypothesis that small bacterial species pass through the filter (Figure 3B). Adding time-based incubations of PenStrep antibiotics to the sample, we observe that with each size-based filtration we measure that the unfiltered fraction has less bacteria than that of the filtered fraction, and incubation with antibiotics up to 60 minutes decreases the bacterial content of both the filtered and unfiltered fractions (Figure 3C).

With techniques established to reduce bacteria in our whole saliva respirometry samples, we performed respirometry on samples which have undergone these bacterial reduction steps. In Figure 3D we compare respirometry traces from the two cellular fractions obtained from 40μm filtration (shown in Figure 3B to result in approximately a 2.5-fold change in 16S rRNA bacterial content). The small fraction
(less than 40μm in size) shows higher pre-injection respiration and lower compound sensitivity (specifically Antimycin A) when compared to the large fraction (greater than 40μm in size) which contains lower bacterial content. Utilizing gentamycin (a gram-positive antibiotic) and magnetic bead exclusion of bacterial endotoxin to reduce bacterial content even further (in combination with aggressive homogenization to attempt to remove bacteria which may be inside the buccal epithelial cells), the resulting respirometry trace has low pre-injection OCR and significantly improved responses to our mitochondrial substrates and inhibitors (Figure 3E).

While the reasons that bacterial contamination impacts Seahorse respirometry in this cell type is not fully understood, our evidence suggests that decreasing the bacterial content within the sample reduces the respirometry artifacts preventing reliable data acquisition. While these processing steps (among others) vastly improved our respirometry results with whole

saliva, this sample material still had two fundamental problems: low reproducibility and a long and complex sample processing to prepare the samples for respirometry.

Incomplete Homogenization of Buccal Epithelial Cells Impacts Seahorse Reproducibility

Though the removal of bacterial contamination greatly improved injection sensitivity, its presence was not the sole cause of high variability in respirometry traces; figures 4A and 4B showcase some of these reproducibility concerns in bacteria-depleted samples. Multiple technical replicates of a whole saliva isolation (Figure 4A-left) are run alongside technical replicates of our mouse liver mitochondria control (Figure 4A-right). While the control exhibits minimal variation between technical replicates, we observe much more variance in our whole saliva cells, a phenomenon quantified in Figure 4B comparing the %CV of the Complex I OCR and Complex IV OCR values obtained from each set of technical replicates. While inconsistency between technical replicates in respirometry can be explained in many ways, one of the most common sources of variation is inconsistent cell plating across the sample plate. This is a phenomenon especially prevalent on the Seahorse respirometry platform which is extremely sensitive to uneven sample dispersion across the sample plate (Yépez et al. 2018). We observed that even the most intense sample homogenization failed to ensure consistent distribution of cellular components between technical replicates. As a result, loading wells with identical volumes of sample would yield vastly different quantities of unbroken buccal epithelial cells, likely contributing to the observed respirometry differences. The buccal epithelial cells take up considerable surface area along the bottom of the Seahorse plate, often overlap and fold over each other within the well, and ultimately create prohibitively inconsistent respirometry results.

Figures 4C-D showcase the resilience of buccal epithelial cells to traditional methods of homogenization used in Seahorse respirometry sample processing. In Figure 3C we compare a control epithelial cell line (VeroE6 kidney epithelial cells) to buccal epithelial cells under freezing

conditions. Pap staining is used to highlight intact epithelial cells, as the stain will only color cells with an intact cytoplasm. While the control cells exhibit significant cell breakage and loss of morphology after a -80°C freeze-thaw cycle and liquid nitrogen snap freeze, the buccal epithelial cells show almost no change when undergoing the same freezing conditions. The buccal epithelial cells show minimal change in their integrity or morphology even after bead homogenization, highlighting the immense resilience of this cell type (Figure 4D). While at this stage in development our assay was largely free of artifacts and responded to compounds, the resulting sample material was not sufficiently reproducible even after a much more complex and involved sample processing procedure than those most commonly used for respirometry.

When compared to our technical control of mouse liver mitochondria run on the same experiment, we see much worse consistency across technical replicates. While across one or two experiments and sample pools this could be due to inconsistencies of the Seahorse platform, observing this repeatedly indicates that this is likely something inherent to the sample material and the processing it has undergone.

Isolation and Characterization of Salivary Leukocytes from Saliva for Respirometry

While respirometry using all of the cells from whole saliva did not prove to be successful due to the presence of buccal epithelial cells which could not be adequately processed, we turned to the other cell types within the mouth. While buccal epithelial cells represent the majority population of cells within the mouth, salivary leukocytes, the minority cell population, could still represent a viable sample type for respirometry. This population is made up of the different immune cells like leukocytes, lymphocytes, and segmented cells which slowly leak into the saliva to give it its immune properties. While this cell population is not as commonly used for research, some protocols have been established to isolate this cell population though these methods had little regard for the integrity of the cells post-isolation (Yamamoto, Saeki, and Utsumi 1991; Fernández-Bertólez et al. 2021; Vidović et al. 2012; Valdiglesias et al. 2021). With

this in mind, we developed our own protocol for the isolation of salivary leukocytes which would provide a population of cells which could be used for the downstream application of respirometry.

Figure 5 depicts our protocol for the isolation of salivary leukocytes in a graphical form. In short, sample collection begins with repeated mouthwashes using a saline solution. The resulting solution is filtered to remove any possible food or large particulate, spun down into a cell pellet, and resuspending in media with antibiotics. Separation of salivary leukocytes from the whole saliva solution occurs by layering the sample over a Histopaque density gradient solution and performing a low–speed centrifugation. This results in the formation of a floating "buffy layer" containing salivary leukocytes and a cell pellet at the bottom of the tube containing mostly buccal epithelial cells. These two cell pellets can be pelleted and frozen to be stored for a later respirometry experiment. On the day of the respirometry experiment cells are thawed, homogenized using a needle and syringe, then snap frozen in liquid nitrogen additional times before they are ready for a standard RIFS respirometry protocol. Identically to the RIFS protocol, a BCA assay is performed to calculate and load samples according to total protein, then loaded on the Seahorse platform to measure ETC Complex I and Complex IV.

Figure 6A compares Pap staining images of our density gradient isolation of salivary leukocytes (right) with the most commonly cited salivary leukocyte isolation utilizing 20μm cell filtration (left). While both methods appear to enrich for salivary leukocytes, the density gradient isolation technique results in the appearance of far fewer epithelial cells in the final cell product. These differences are quantified Figures 6B-D revealing that while the number of salivary leukocytes obtained between the two isolation methods is similar, the number of buccal epithelial cells contaminating the salivary leukocyte population using the filter isolation method is much greater. This culminates in a significantly higher salivary leukocyte to epithelial cell ratio

when isolating via our density gradient procedure, a factor which we have shown should have much better respirometry results when compared to our whole saliva cell isolations.

The final cell population obtained via this novel isolation procedure has a significant number of salivary leukocytes with minimal buccal epithelial cell contamination, as noted by a lack of blue, pink, or orange colorization when Pap stained (Figure 7A). These two cell populations obtained during isolation (salivary leukocyte- top and buccal epithelial cell- bottom) can be stained and imaged to reveal typical leukocyte and epithelial cell morphology and the presence of mitochondria and mitochondrial membrane potential via MitoTracker Green and TMRE staining respectively (Figure 7B). We know from our work with whole saliva that bacterial contamination is a major source of respirometry artifacts, and we observe via 16S rRNA RT-qPCR that our separation of leukocytes from epithelial cells results in an enrichment of bacteria in the epithelial cells with a decrease in bacteria in our salivary leukocyte population (Figure 7C). Additionally in Figure 7D we observe that across multiple sample pools the ratio between 18S rRNA (human rRNA) and 16S rRNA (bacterial rRNA) increases in our salivary leukocyte fraction indicating that our ratio of human matter to bacterial matter is increasing in our salivary leukocyte population compared to our buccal epithelial cell population. Finally, we compared in a single individual their immune cell composition in whole blood, PBMCs isolated from whole blood, and salivary leukocytes using a CBC cell analysis instrument. Though our salivary leukocyte isolation procedure closely matches that done to isolate PBMCs from whole blood, we observe that for lymphocyte, granulocyte, and monocyte percentages salivary leukocytes compare more closely to whole blood than PBMCs from whole blood compare to whole blood. With our novel salivary leukocyte isolation procedure, we have a cell population which has low bacteria levels, is relatively simple to process, and is mostly free of un-processable epithelial cells.

Respirometry of Salivary Leukocytes

Now capable of reliably isolating a population of salivary leukocytes ready for respirometry, we assessed their performance on the Seahorse platform. Performing respirometry on this cell population produces reproducible results with a response to all of our substrates and inhibitors (Figure 8A). Additionally, we observe that upon further isolation with CD45+ magnetic beads (a highly-conserved marker found on all nucleated cells of the hematopoietic system) we observe a nearly identical respirometry trace but with slightly increased activity per µg of protein. This suggests that not only is our salivary leukocyte population mostly composed of CD45+ cells, but that these cells are the primary contributor to our respiratory activity. With additional bead homogenization steps, we performed a magnetic bead isolation using a Tomm20 antibody (an outer mitochondrial membrane marker). While the activity is low (near the signal-to-noise threshold of the instrument) and the traces are not very consistent, we observe some responses to our mitochondrial substrates and inhibitors, providing evidence that the respiration in these cells is mitochondrial in nature and not background or artifact (Figure 8B). While mitochondrial isolation is possible, it must be noted that mitochondrial isolation using this magbead isolation protocol has very low yield and would not be sufficient for individual samples (it would only work for large pools of sample).

While Figures 8A-B were performed with samples pooled from multiple individuals, Figure 8C-8D assess our isolation procedure and respirometry protocol for samples from single individuals. In Figure 8C we compare the respirometry samples from two individuals, revealing that our assay is sensitive enough that the sample material obtained from a single individual is sufficient for multiple technical replicates (N=3) in a respirometry experiment. Additionally, we observe varying activity per µg of protein, an early indication that this assay will be capable of measuring differences between two individuals, and could be used on larger populations to assess the differences due to biological factors like age, BMI, etc. In Figures 8D-8F we assess both the reproducibility of our assay across multiple isolations from the same individual and the

stability of mitochondrial measurements across short periods of time. In Figure 8D we sampled an individual at one time point and isolated their salivary leukocytes for respirometry, then asked them to refrain from food or drinks (other than water) for 60 minutes, at which point they were sampled again and their salivary leukocytes were isolated. We expect that across such a short time period, there would be minimal change in the salivary leukocyte mitochondria and therefore any changes observed would be a result of inconsistency across either the sampling, isolation, or respirometry procedures. When performing respirometry on both of these samples we observed no significant difference in the traces of these two samples and the respective Complex I and Complex IV readouts which would be obtained from these respirometry traces. Expanding this experiment from one individual to three individuals we observe that on an individual by individual basis we see no change in Complex IV values across a 60 minute time course (Figure 8E), and assessing these three individuals as a population we also observe no change in their Complex IV values across this time period. These data together indicate that our assay is reproducibly assessing respirometry in our salivary leukocyte population. Additionally, our data provides early evidence that this assay is sensitive enough to detect differences between different individuals, making it a potential diagnostic or monitoring solution with larger human validation cohorts.

Discussion

In this paper we have discussed the development and troubleshooting involved in creating our methodology for a non-invasive assay measuring respirometry from human salivary leukocytes. This process included the assessment of whole saliva in respirometry, the development of a novel isolation procedure for salivary leukocytes, and the characterization and optimization of this new cell population. While the final assay is consistent and reproducible, the cell type obtained by our isolation process is still not fully understood.

While the RIFS assay can measure ETC Complexes I, II, and IV, we have observed far lower Complex II activities in this cell compared to Complex I. We observe via western blot that Complex II protein is very limited in cells from whole saliva making it possible that salivary leukocytes have fewer Complex II supercomplexes or that they have low Complex II activity. This could be explained by the oral environment in which these cells reside, as micro-organisms typically prefer oxidation via glycolytic pathways which generate NADH, the substrate of Complex I, thereby creating a preference of the salivary leukocytes to Complex I substrates. We have also observed that despite injecting NADH in excess for the Seahorse assay, after initial response to the NADH injection the OCR begins to decrease in subsequent measurements rather than staying stable. While this phenomenon is less prevalent when adding even higher concentrations of NADH (not shown), this decrease can diminish the apparent response to our Complex I/Complex III inhibitory compound injection (Antimycin A/Rotenone), though when doing fewer measurement cycles we still observe sensitivity to our inhibitory compounds.

We believe that salivary leukocyte respirometry has multiple advantages over primary tissue respirometry and/or PBMC respirometry (one of the most viable alternatives to systemic respirometry measurements. Compared to drawing blood for PBMC respirometry, not only is mouthwash collection less invasive, it can be sampled with far greater frequency for time-course studies, and is far more likely to be adopted by under-represented communities or used by individuals which cannot have their blood drawn. Methodologically there are also advantages to PBMC respirometry, as while salivary leukocyte isolation is approximately as complex and time-intensive as PBMC isolation, the final population is free of platelets which may contaminate respirometry results. Additionally, our data suggests that salivary leukocytes may even be a better representation of the immune cell ratios circulating throughout the body.

While we have developed this assay with mitochondrial monitoring and diagnostics in mind for the future, it must be noted that due to the difficulties associated with primary tissue respirometry and the limited adoption of alternative respirometry tissues like PBMCs or fibroblasts, there is not really a “golden standard” for measurements of mitochondrial respiration. It will take a significant effort to develop and run clinical studies which can begin to assess how mitochondrial respiration is altered in response to both biological factors like age, sex, and race but also disease factors like neurodegeneration, cancer, and diabetes. Additionally, understanding just the normal variance of mitochondria over shorter time periods like before and after meals or day/night cycles is a vital part of this assessment. Respirometry in salivary leukocytes represents a much more viable method of methodology to perform these types of studies when compared to the current techniques in use. We hope that in making human respirometry much feasible with our assay that future studies may begin to assess how mitochondria change in humans under these varied conditions.

Figures

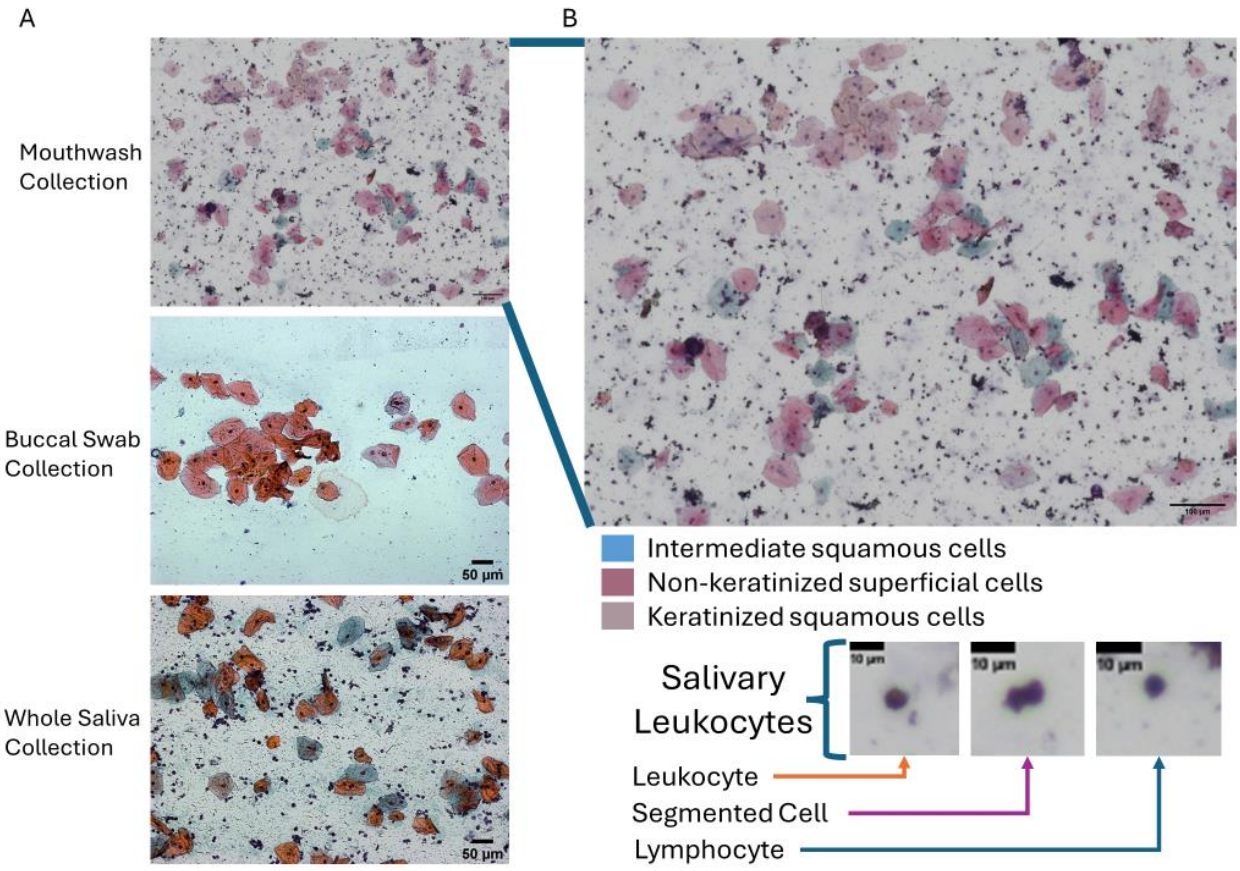

Figure 1: The Cellular Content in Saliva is Primarily Made Up of Two Cell Types: Buccal Epithelial Cells and Salivary Leukocytes

(a) Cells are collected via mouthwash collection (top), buccal swab collection (middle), or whole saliva collection (bottom). The cells are resuspended in PBS, streaked across a microscopy slide, and fixed with 95% EtOH. Staining was done using a Pap staining kit where epithelial cell cytoplasms will be colored pink, orange, or blue based on their keratinization status and nuclei will be stained as purple puncta. Collection via these three methods yields greatly varied proportions of buccal epithelial cells and salivary leukocytes.

(b) An enlarged version of the mouthwash collection image in (a). Pap smear colors are indicative of the keratinization status of buccal epithelial cells present in the sample. Inset

images (taken from the above image) show examples of the different types of immune cells found within salivary leukocytes found in the oral sample population.

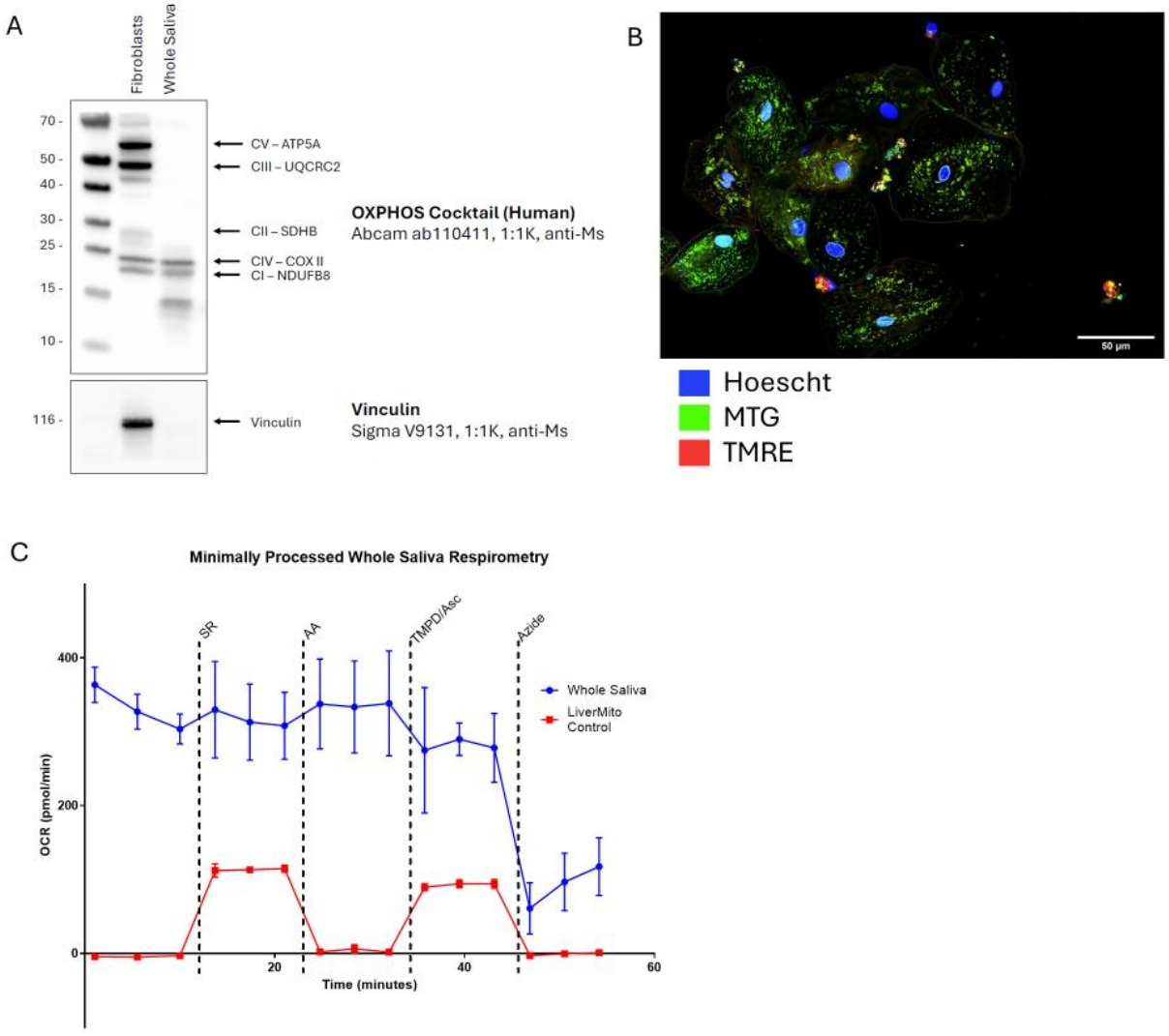

Figure 2: Mitochondria and their ETC Components are Present in Cells from the Oral Cavity

(a) Western blotting of protein isolates from whole saliva cell pellets for all human ETC complexes. Samples from left to right: Ladder, primary human fibroblast control, whole saliva cell pellet.

(b) Confocal microscopy of a whole saliva cell pellet. Cells are stained with Hoescht (blue), MitoTracker Green (green), and TMRE (red/yellow).

(c) Seahorse respirometry experimental trace comparing cells isolated from whole saliva (with no additional processing) (blue) and a respirometry control of mouse liver mitochondria (red). Whole saliva exhibits higher pre-injection OCR and an insensitivity to mitochondrial substrates and inhibitors with the exception of azide.

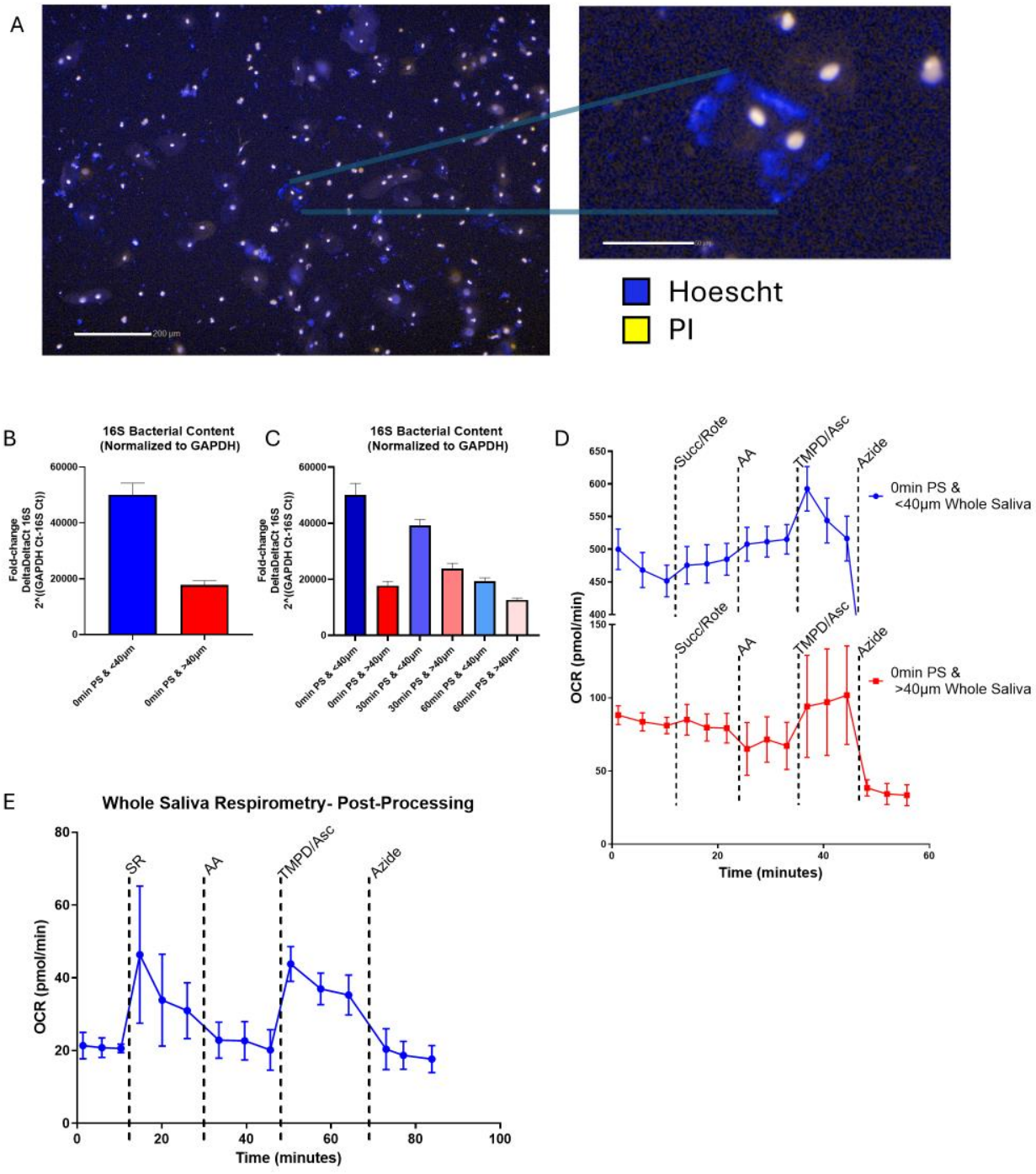

Figure 3: Oral Microbiome is a Major Source of Respirometry Artifacts for Cells Isolated from Whole Saliva

(a) Fluorescence microscopy of cells isolated from whole saliva stained with PI/DAPI (Yellow) and Hoescht (Blue). The inlet highlights a subsection of the image with a set of buccal epithelial cells with bacterial staining surrounding their exteriors. As per Rudney and Chen (2006), we observe the anomalous phenomenon that buccal epithelial cells are permeable to the DNA stain PI (propidium iodide) which should only stain intact/alive cells (Rudney and Chen 2006).

(b) & (c) 16S rRNA content (bacterial content) of cells isolated from whole saliva as measured by fold-change of 16S normalized to GAPDH. (b) measures 16S content before and after 40μm filtration. (c) measures 16S content before and after 40μm filtration with the addition of a time course of exposure to media containing PenStrep antibiotics.

(d) Seahorse respirometry comparing cells isolated from whole saliva before and after 40μm filtration. Seahorse samples were loaded at equivalent protein concentrations as measured by BCA total protein.

(e) Seahorse respirometry of cells isolated from whole saliva after undergoing 40μm filtration, 60min antibiotic treatment using AntiAnti and Gentamycin, bead homogenization, and endotoxin removal via magbead isolation.

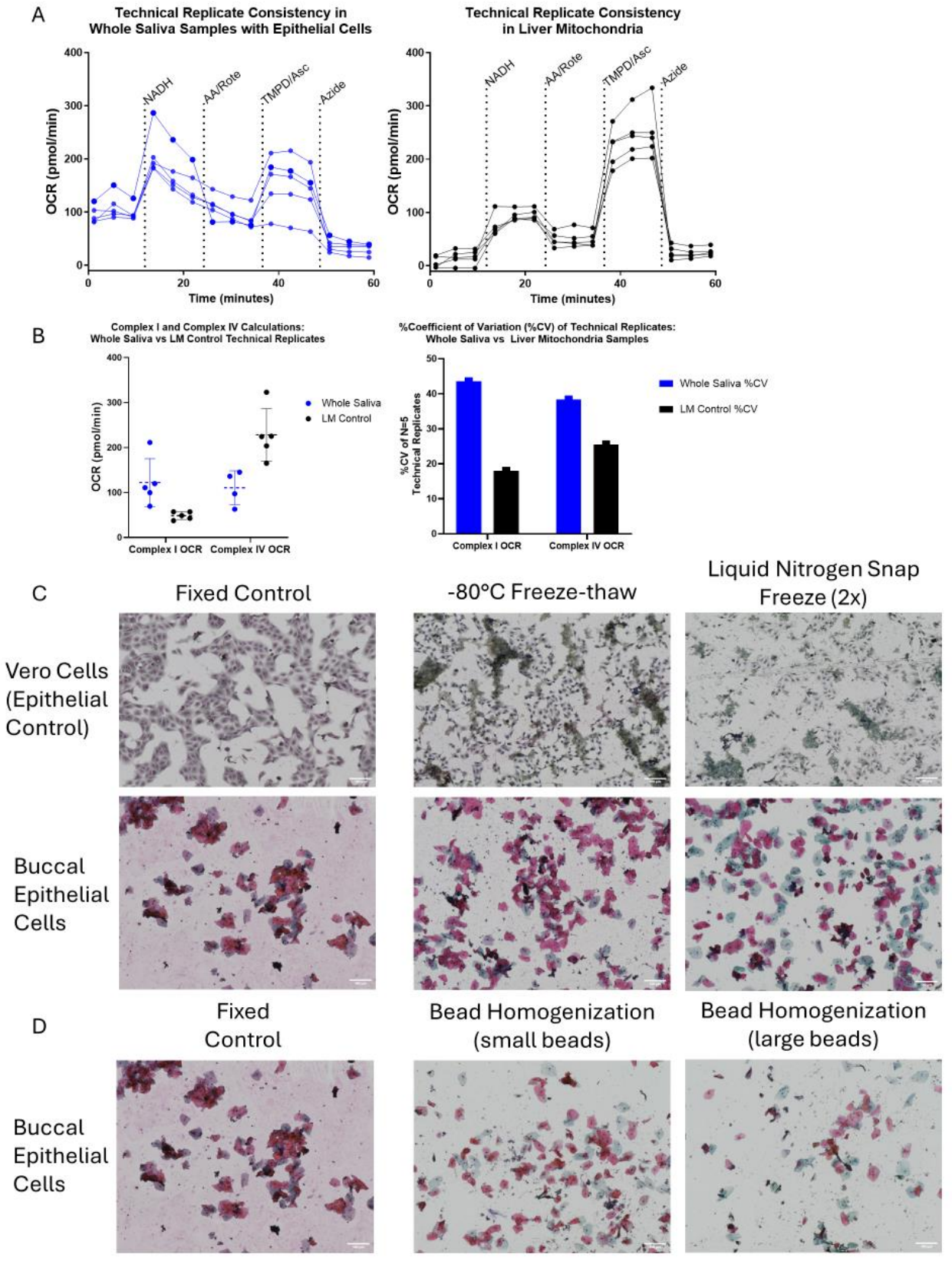
A
Technical Replicate Consistency in Whole Saliva Samples with Epithelial Cells
Technical Replicate Consistency in Liver Mitochondria
OCR (pmol/min)
Time (minutes)
NADH
AA/Rote
TMPD/Asc
Azide
B
Complex I and Complex IV Calculations: Whole Saliva vs LM Control Technical Replicates
Whole Saliva
LM Control
Complex I OCR
Complex IV OCR
%Coefficient of Variation (%CV) of Technical Replicates: Whole Saliva vs Liver Mitochondria Samples
%CV of N=5 Technical Replicates
Whole Saliva %CV
LM Control %CV
C
Fixed Control
-80°C Freeze-thaw
Liquid Nitrogen Snap Freeze (2x)
Vero Cells (Epithelial Control)
Buccal Epithelial Cells
D
Fixed Control
Bead Homogenization (small beads)
Bead Homogenization (large beads)
Buccal Epithelial Cells

Figure 4: Buccal Epithelial Cells Impact the Reproducibility of Respirometry Results due to an Inability to be Broken Down

(a) Seahorse respirometry of cells isolated from whole saliva with inconsistency across technical replicates of the same sample (blue-left). This is compared to the expected variation of technical replicates of liver mitochondria controls (black-right).

(b) (left) compares the Complex I OCR calculation (NADH-stimulated OCR – Antimycin A-stimulated OCR) and Complex IV OCR calculation (TMPD/Asc-stimulated OCR- Azide-stimulated OCR) for the traces in (a). (right) assesses the %CV of these two sample groups indicating a much larger variance in technical replication in our whole saliva samples when compared to that of liver mitochondria controls.

(c) Control epithelial cells (VeroE6 cell line-top row) and buccal epithelial cells (bottom row) which have been smeared along a microscope slide, fixed in 95% EtOH, stained with a Pap staining kit to stain intact cytoplasm and nuclei, and imaged using a Keyance BZ-X800 color microscope. Left column shows control samples undergoing no additional processing. Middle column the samples were placed at -80°C for 2 hours before fixation. Right column the samples were snap frozen in liquid nitrogen for 2 cycles before fixation. While the freezing procedures left our buccal epithelial cells mostly intact, these same protocols resulted in significant cell death and changes in morphology in our control epithelial cell line.

(d) This repeats the protocol in (c) but processes the cellular material with either (left) nothing, (middle) bead homogenization using small beads (3.0mm diameter), or (right) bead homogenization using larger beads (6.0mm diameter). The presence of Pap staining within the samples indicates that the cytoplasms of these cells are still intact.

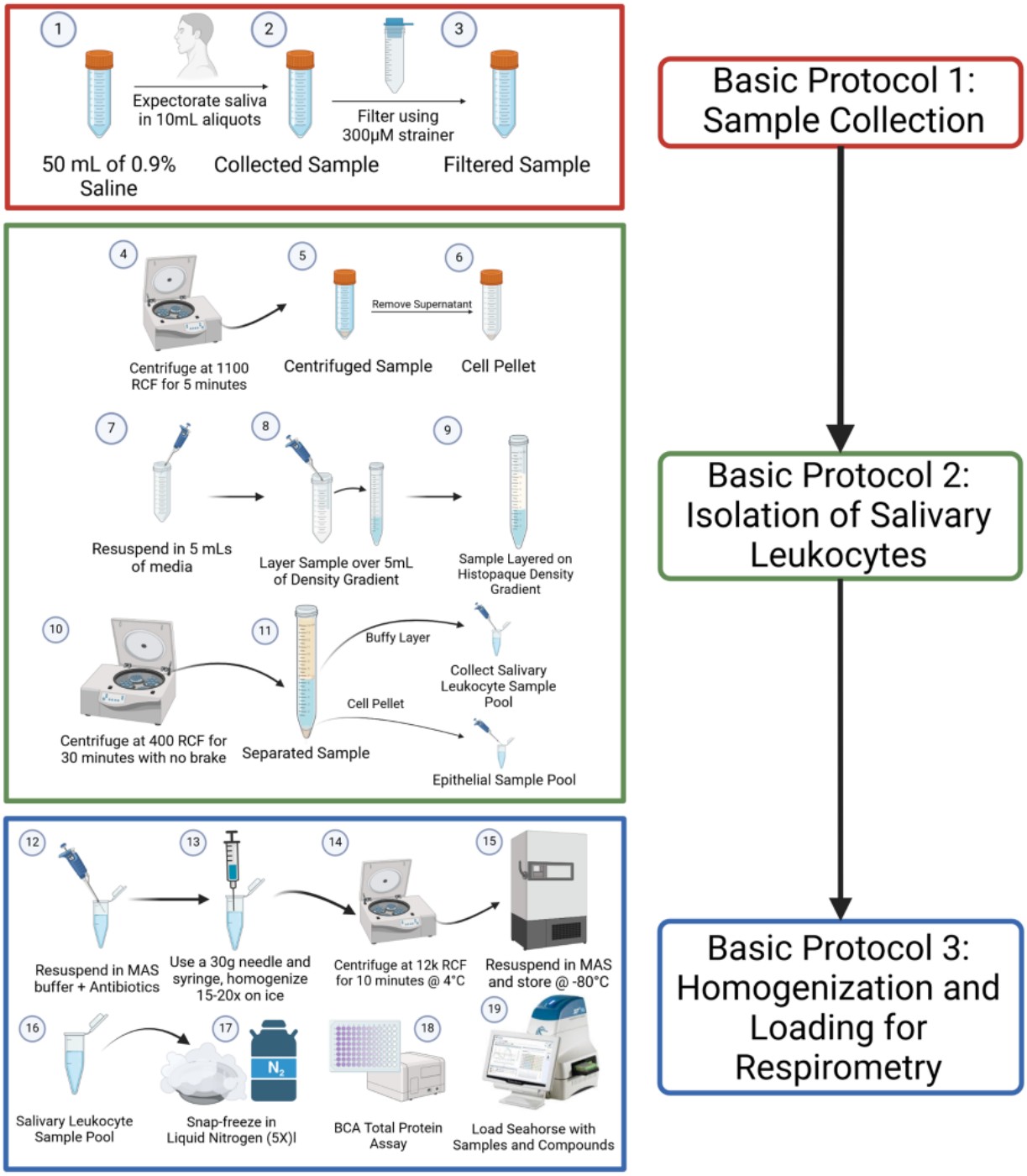

Figure 5: Graphical Protocol for the Isolation of Salivary Leukocytes for Respirometry

This figure outlines the protocol developed for the isolation of salivary leukocytes for the purpose of respirometry. It is divided into three sections: sample collection, isolation of salivary leukocytes, and homogenization and loading for respirometry. We will summarize each section

here. In section one, mouthwash samples are collected in 0.9% saline and these samples are filtered to remove any food or debris, then centrifuged to pellet the cellular material. In section two, these samples are gently layered upon a density gradient solution of Histopaque-1077 and slowly centrifuged for 30min. The resulting sample contains a cell pellet containing buccal epithelial cells, and a layer of floating cells above the density gradient solution which contains the salivary leukocytes such that these layers may be collected separately. In section three, after freezing the cells for storage the salivary leukocytes must be snap frozen in liquid nitrogen multiple times and must be homogenized using a needle and syringe. After this is completed, samples may be loaded via total protein using the RIFS assay protocol for assessment of Complex I and Complex IV as outlined in Osto et al. 2020 (Osto et al. 2020).

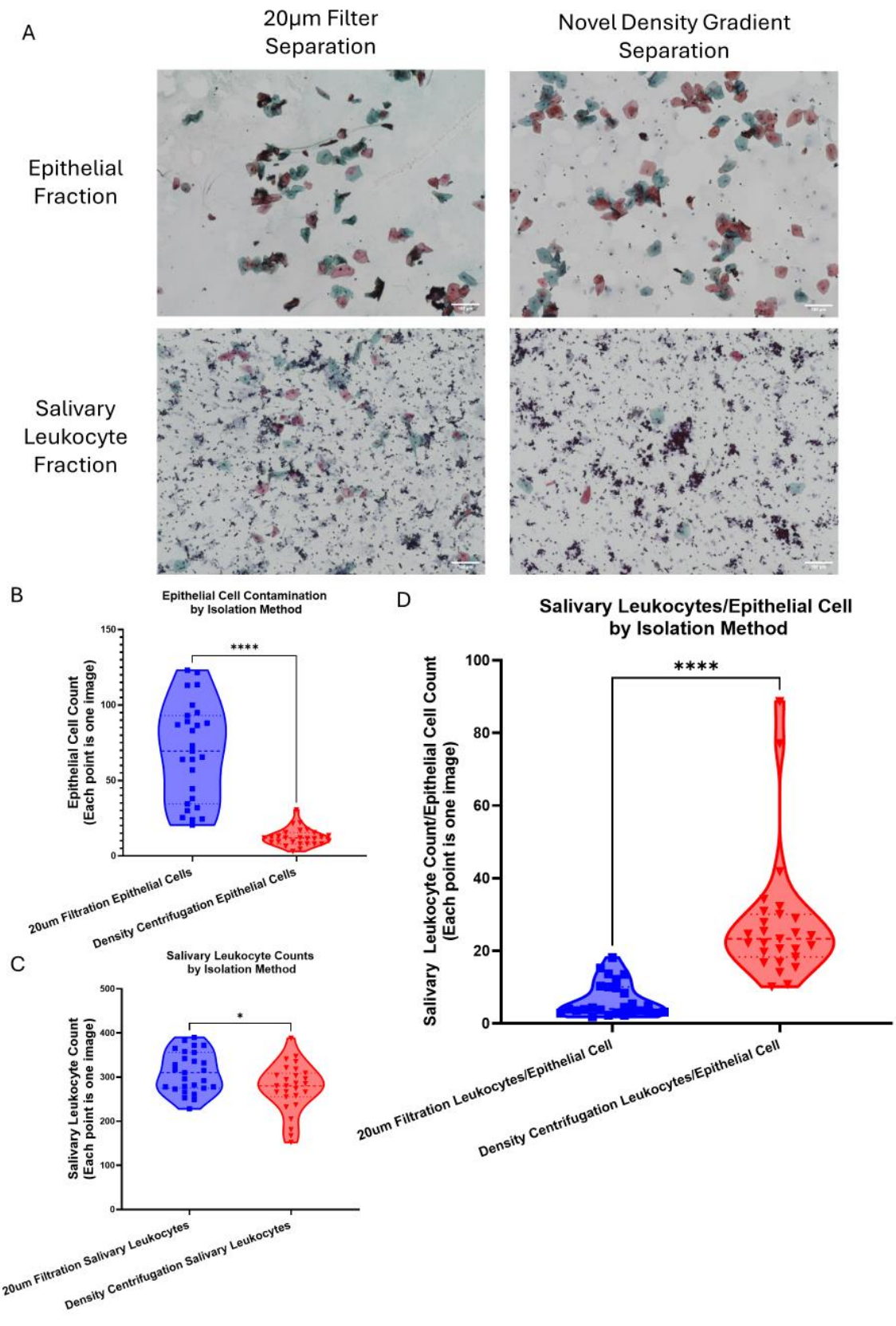
A
20µm Filter Separation
Novel Density Gradient Separation
Epithelial Fraction
Salivary Leukocyte Fraction
B
Epithelial Cell Contamination by Isolation Method
Epithelial Cell Count (Each point is one image)
****
20um Filtration Epithelial Cells
Density Centrifugation Epithelial Cells
C
Salivary Leukocyte Counts by Isolation Method
Salivary Leukocyte Count (Each point is one image)
*
20um Filtration Salivary Leukocytes
Density Centrifugation Salivary Leukocytes
D
Salivary Leukocytes/Epithelial Cell by Isolation Method
Salivary Leukocyte Count/Epithelial Cell Count (Each point is one image)
****
20um Filtration Leukocytes/Epithelial Cell
Density Centrifugation Leukocytes/Epithelial Cell

Figure 6: Isolation of Salivary Leukocytes via Density Gradient Centrifugation Reduces Buccal Epithelial Cell Contamination

(a) Comparing the cellular contents of salivary leukocytes isolated via 20μm filtration and density gradient separation. Cell fractions for the epithelial fractions and salivary leukocyte fractions were plated on a microscopy slide, fixed with 95% EtOH, and stained with a Pap staining kit to color epithelial cells and nuclei. For the 20μm filter separation, the salivary leukocyte fraction is that which passed through the filter and the epithelial fraction is that which remained above the filter. For the density gradient separation, the epithelial fraction is that which formed a cell pellet at the bottom of the tube after centrifugation over a density gradient solution and the salivary leukocyte fraction is that which stayed in a buffy layer above the density gradient after centrifugation.

(b) Epithelial cell counts of cells in the salivary leukocyte fraction for each isolation method. Each point represents the average epithelial cell count of two operators counting one of 27 images taken for each slide.

(c) Salivary leukocyte cells counts of cells in the salivary leukocyte fraction for each isolation method. Counts were generated by automated image analysis of the 27 images taken for each slide, counting based on cell size (between an area of 0.008 and 0.020).

(d) The ratio of salivary leukocytes per epithelial cell for the two isolation methods using the counts shown in sections (b) and (c).

A

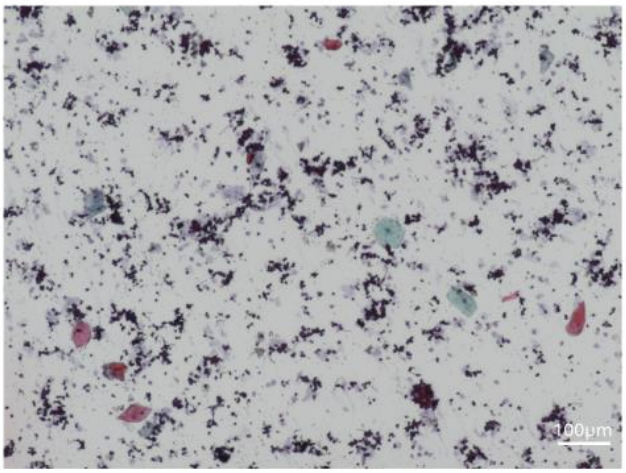
100µm

B

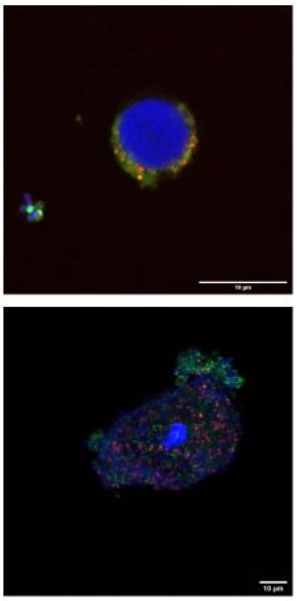

C

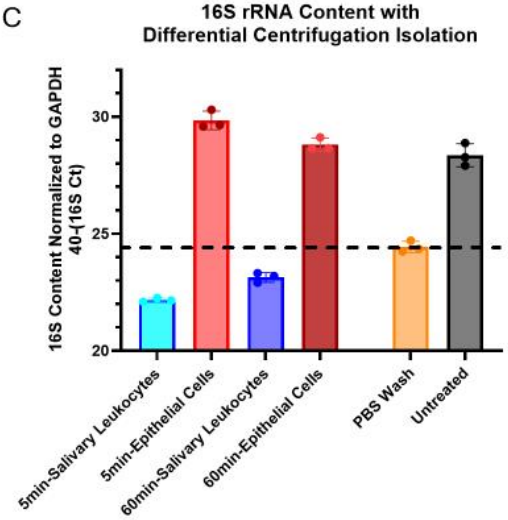
16S rRNA Content with
Differential Centrifugation Isolation
16S Content Normalized to GAPDH
40-(16S Ct)
30
25
20
5min-Salivary Leukocytes
5min-Epithelial Cells
60min-Salivary Leukocytes
60min-Epithelial Cells
PBS Wash
Untreated

D

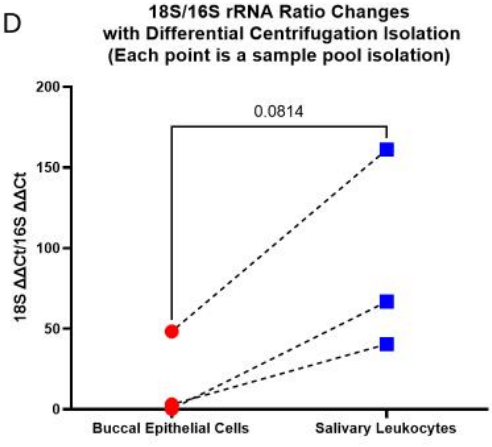
18S/16S rRNA Ratio Changes
with Differential Centrifugation Isolation
(Each point is a sample pool isolation)
18S ΔΔCt/16S ΔΔCt
200
150
100
50
0
0.0814
Buccal Epithelial Cells
Salivary Leukocytes

E

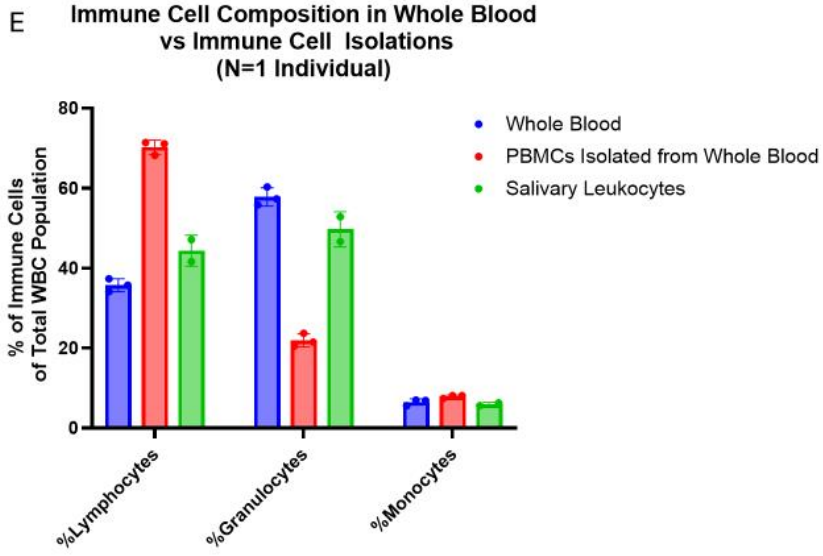
Immune Cell Composition in Whole Blood
vs Immune Cell Isolations
(N=1 Individual)
% of Immune Cells
of Total WBC Population
80
60
40
20
0
%Lymphocytes
%Granulocytes
%Monocytes
Whole Blood
PBMCs Isolated from Whole Blood
Salivary Leukocytes

Figure 7: Characterization of Salivary Leukocytes Isolated via Density Gradient Centrifugation for Respirometry

(a) Pap staining image of salivary leukocytes isolated using our isolation procedure.

(b) Confocal microscopy of live cells after isolation stained with Hoescht (blue), MitoTracker Green (green), and TMRE (yellow/red). (top) a salivary leukocyte imaged from the salivary leukocyte fraction of the isolation. (bottom) a buccal epithelial cell imaged from the epithelial cell fraction of the isolation.

(c) 16S rRNA content measured via RT-qPCR comparing the salivary leukocyte and epithelial cell fractions obtained in the isolation process. The data is presented as the inverse of the 16S rRNA Ct value (40-Ct) such that higher values are indicative of higher 16S bacterial rRNA quantity. RNA values are normalized to GAPDH RNA.

(d) 18S rRNA to 16S rRNA ΔΔCt ratios (normalized to GAPDH) for 3 sample pools on 3 separate days comparing the salivary leukocyte fraction and the epithelial cell fraction.

(e) Comparison of the immune cell compositions of different cell populations from 1 individual taken within a 30 minute period using a CBC analyzer. Values measured are the percent of lymphocytes, granulocytes, and monocytes from the total number of cells counted by the instrument. PBMCs were isolated from whole blood following a standard CPT tube isolation protocol. Salivary leukocytes were isolated via our protocol described in this paper.

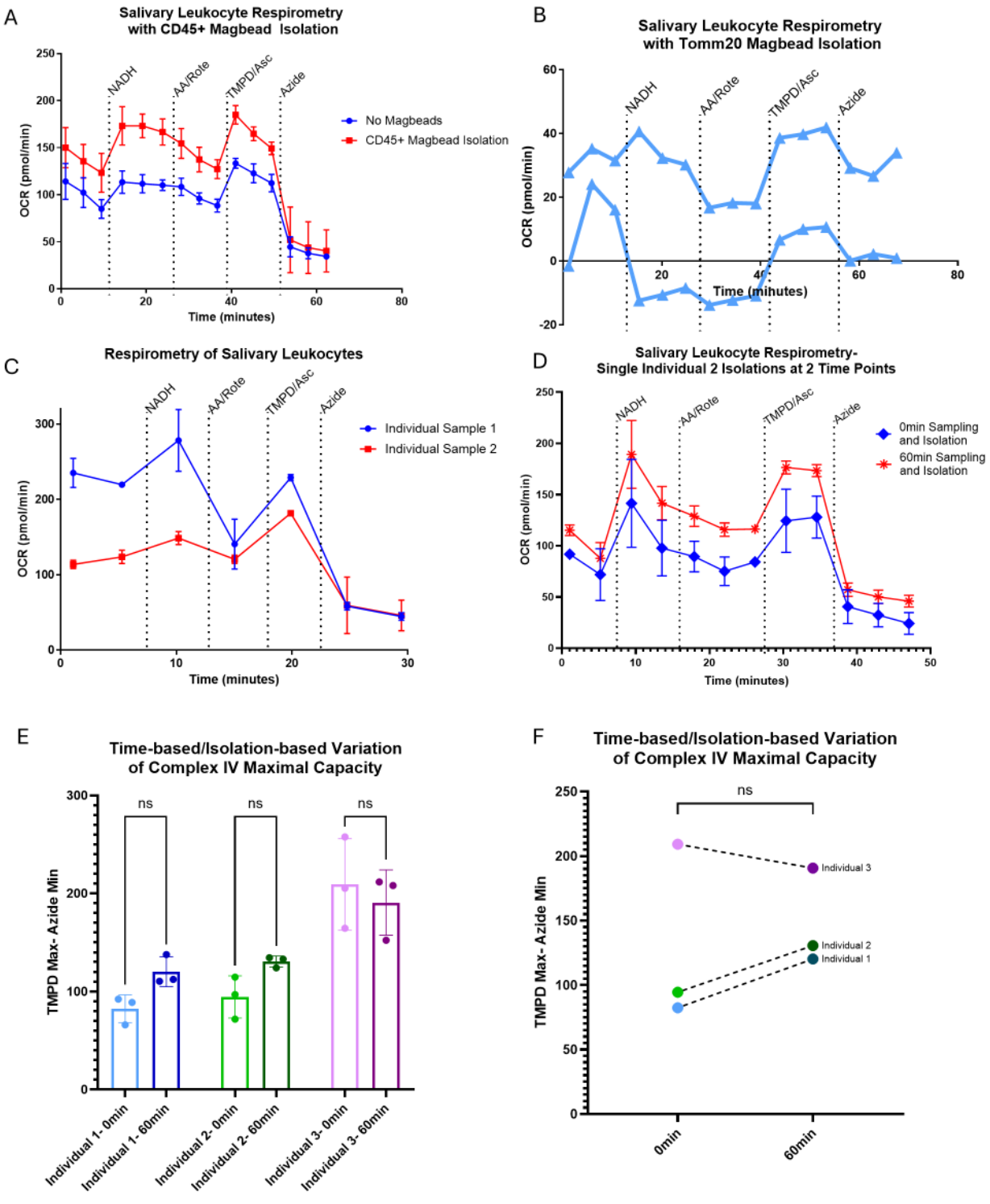

Figure 8: Respirometry of Salivary Leukocytes

(a) Respirometry traces comparing salivary leukocytes with and without additional isolation using CD45+ specific magbeads. Samples were loaded at equivalent total protein concentration.

(b) Respirometry traces from a salivary leukocyte population which was bead homogenized then isolation using TOMM20+ specific magbeads. These traces represent the two technical replicates obtained from the sample pool of 8 individuals.

(c) Salivary leukocyte respirometry which were isolated from a single individual rather than a pooled collection of sample from multiple individuals. Sample 1 and Sample 2 represent two separate individuals whose samples were taken at the same time and isolated in the same isolation procedure.

(d) An individual was sampled at time 0min and this sample their salivary leukocytes were isolated. The individual was asked to refrain from eating or drinking fo 60min and then were sampled again and their salivary leukocytes were isolated in a second isolation. The respirometry traces from these two experiments are displayed here.

(e) & (f) The experiment described in (d) was completed on three more individuals assessed at time 0min and 60min in two separate isolations. (e) compares the Complex IV OCR values on an individual basis. (f) represents these Complex IV OCR values with the three individuals forming a sample population together.

Methods

Oral Sampling Collection:

Where possible, participants for sample sample collections were asked to refrain from food or drink for at least 30 minutes prior to sampling.

Buccal swab samples were obtained by firm but appropriate swabbing of a buccal swab (Isohelix SK-1 or equivalent) back and forth for 10-15 strokes across all four quadrants of the mouth and cheek. The swab is added to 2mL of 1X PBS and moved back and forth within the

solution for 20-30 seconds to remove all cellular material from the swab into the solution. This cellular material may then be placed into sterile tubes for further experiments.

Whole saliva samples were obtained by expectorating (spitting) into a clean 15mL conical tube until approximately 2-3mL of saliva is obtained. Samples may be diluted in 1X PBS as necessary.

Mouthwash samples are obtained by sipping approximately 10mL of 0.9% saline solution (food-grade sea salt in water) and moving this liquid around all areas of the mouth firmly but appropriately (so as not to create too many bubbles) for 30-60 seconds. Repeat this process until 50-100mL of mouthwash solution is collected.

All sample types once collected may be pelleted via centrifugation at 1,100 x g for 10 minutes and resuspended in either 1X RPMI or 1X PBS depending on the experiment.

Pap Staining:

Cells were smeared onto microscopy slides and left to lightly dry for 5-10min. After slightly drying, cells were soaked in 95% ethanol for fixation and left overnight to dry. Pap staining of these slides was done using the manufacturer's recommended protocol (CP Lab Chemicals Ref: PAP-2). Imaging was done using a Keyance BZ-X800 color microscope with mild edge correction applied to the final images.

Western Blots:

Samples were separated via electrophoresis on a 4-12% Bis-Tris gel for 1.25 hours at 120 V. Proteins were then transferred to a methanol activated PVDF membrane for 1.25 hours at 115 V. Membranes were blocked with 3% BSA in PBS-T for 1 hour and were incubated with primary antibody diluted in blocking solution overnight at 4°C. Following incubation, the membranes were washed 3 x 10 minutes with PBS-T. Membranes were incubated for 1 hour with HRP conjugated secondary antibodies diluted in blocking solution, then were washed again

3 x 10 minutes with PBS-T. Chemiluminescent detection was completed on the ChemiDoc Molecular Imager (BioRad) and images were processed with Image Lab software (BioRad).

Antibodies used:

OXPHOS Cocktail (Human): Abcam ab110411, 1:1000, anti-mouse

Vinculin: Sigma V9131, 1:1000, anti-mouse

Confocal Imaging:

Super-resolution confocal microscopy was performed on live cells on microscopy slides using a Zeiss LSM880 using a 63× Plan-Apochromat oil-immersion lens and AiryScan super-resolution detector with humidified 5% CO2 chamber on a temperature-controlled stage (37°C). Mitochondria were stained with 15 nM Tetramethylrhodamine Ethyl Ester Perchlorate (TMRE) (Invitrogen, Eugene, OR.) or with 200 nM MitoTracker green (MTG) (Thermo Fisher Scientific, Roskilde, Denmark) for 45 min prior to imaging. MTG was excited with 488 nm laser and TMRE was excited with a 561-nm laser.

RT-qPCR Experiments:

Samples from either the salivary leukocyte or epithelial cell pools underwent RNA extraction using the Qiagen RNeasy RNA Extraction Mini kit following the manufacturer's recommended protocol. The resulting RNA concentration was measured using a Nanodrop assay.

Reverse transcription of the resulting RNA products were done using the Thermofisher Reverse-Transcriptase assay kit following the manufacturer's recommended guidelines. Reverse transcription temperature cycling was as follows:: 25°C for 10 minutes, 37°C for 120 minutes, 85°C for 5 minutes, and a hold temperature of 4°C

PCR reactions were done using (1X) ThermoFisher *Power*SYBR Green PCR Mastermix combined with 100nM of forward and reverse primers. Cycling parameters were: 1 cycle of:

(50°C for 2min, 95°C for 10min); then 40 cycles of: (95°C for 15sec, 60°C for 60sec with acquisition). Data analysis was done using traditional DeltaCt and DeltaDeltaCt normalization calculations (normalized to GAPDH).

Primer Information:

16S rRNA Fwd- 5′ CGGCAACGAGCGCAACCC 3′

16S rRNA Rev- 5′ CCATTGTAGCACGTGTGTAGCC 3′

18S rRNA Fwd 5’- TGACTCAACACGGGAAAC-3’

18S rRNA Rev: 5’ - TCGCTCCACCAACTAAGAAC-3’

hGAPDH Fwd: 5'- *CCACCTTTGACGCTGGG*

hGAPDH Rev: 5'- CATACCAGGAAATGAGCTTGACA

CBC Experiments:

CBC cell analyses were done using a Heska HemaTrue Hematology Analyzer using the manufacturer recommended instructions. Samples were assessed as an average of triplicate measurements from the instrument.

Magnetic Bead Isolations:

Magnetic bead isolations were done using Miltenyi Biotec products using their recommended protocols. All separations were done using a OctoMACS platform with MS columns (Ref: 130-042-201). Beads used for isolations include CD45 human (Ref: 130-045-801), Endotoxin removal beads (130-093-659), and the TOMM20 magbeads from the Mitochondrial Isolation Kit, Human (Ref: 130-094-532).

Isolation of Salivary Leukocytes:

Human subjects are asked to refrain from food or drink approximately 30 minutes prior to sampling. They are given 50-100mL of 0.9% saline solution and asked to sip approximately 10-15mL at a time and move this liquid thoroughly but appropriately all throughout their mouth for

approximately 45-60sec, then to spit this liquid out of their mouths into a clean collection tube with as minimal bubble production as possible. This process is repeated with 30sec breaks in between repetitions until the saline solution is finished. The resulting mouthwash sample is filtered through a 300µm strainer to remove any food particles or debris, then centrifuged at 1,100 x g for 10min. The supernatant is discarded and the cell pellet formed is resuspended in RPMI-1640 with Glutamine, 1X FBS, 1X Anti-Anti, and 50µg/mL of Gentamycin.

In a 15mL conical tube, layer 5mL of resulting cell solution over 5mL of Histopaque-1077, taking care to create distinct layering of the two liquids. Centrifuge the 15mL density gradient sample tubes at 400 x g for 30min with a slow acceleration speed (approximately 60-90sec to reach 400 x g) and no centrifugation brake. The resulting solution will have a cell pellet at the bottom of the tube and a floating layer or “buffy layer” of cells which are resting above the clear density gradient solution. Collect the buffy layer of cells and add it to a new 15mL conical collection tube with fresh media, this collection will contain your salivary leukocytes. The cell pellet at the bottom can be collected in a fresh 15mL conical with media to assess the buccal epithelial cells, or can be discarded if they will not be used. Centrifuge the resulting salivary leukocytes at 1,100 x g to collect them. Resuspend in 1X MAS solution containing 1X Anti-Anti and 50µg/mL of Gentamycin and store at -80°C until the day of the respirometry experiment.

On the day of the respirometry experiment, thaw your salivary leukocyte samples by hand or on ice. Two steps must be performed prior to respirometry and we have found that they can be done in either order:

Snap freeze the samples in liquid nitrogen for approximately 30sec then let them thaw. Repeat this process 5 times. Keep the samples on ice one completed.

Using a 30G needle and 1mL syringe, slowly vacuum up the sample into the syringe, then slowly expel the liquid from the syringe. Repeat this process 10-20 times. Keep the samples on ice as much as possible during this procedure.

Once both the snap freezing and needle homogenization has been completed, centrifuge the samples at 12,000 x g for 10min at 4°C. Remove the supernatant and resuspend in 1X MAS with Anti-Anti and Gentamycin (as described above). Perform a BCA assay on the samples to determine total protein quantification and load your salivary leukocytes onto a Seahorse sample plate between 10-30µg of total protein. For the Seahorse protocol, follow the RIFS assay for Complex I and Complex IV assessment as described in Osto et al. 2020.

CONCLUSION

Many studies have revealed how important mitochondrial respirometry is as a measurement of mitochondrial function and its myriad of roles in disease progression. Despite this importance, many studies choose to exclude this measurement because the methodologies associated with respirometry are prohibitively difficult, expensive, and time intensive. These methodological difficulties have resulted in limitations in the type and amount of sample which can undergo respirometry, ultimately limiting the scientific questions that we as a field can ask and answer using this technique. As discussed in Chapter 1 of this thesis, the RIFS assay, allowing for the measurement of respirometry in tissues which have been previously frozen, overcomes many of the hurdles associated with sampling for respirometry. In this thesis, we assess how we can use the RIFS assay to overcome the limitations of the current mitochondrial respirometry techniques so that we may answer new research and clinical questions.

In Chapter 2 of this thesis, we describe a study assessing mitochondrial function of the human brain in high-resolution. In a first-of-its-kind study, we CNC milled a slice of a human brain hemisphere into 703 voxels or cubes, measuring mitochondrial function in these cubes using the RIFS assay. In performing this study, we made many novel discoveries about mitochondrial function within the brain including a trend associating the evolution of the brain with a preference for increased mitochondrial energetic capacity. Additionally, using this study set in combination with machine learning and advanced MRI parameters, we were able to predict mitochondrial respiratory capacity of the whole brain using this single slice. While this study presents intriguing biological conclusions, it also represents a novel methodological challenge as many of the current respirometry methods are not suitable for sample sets which are hundreds of samples large.

In Chapter 3 of this thesis, we describe the methodological techniques developed specifically to handle a high-throughput study with hundreds of samples (as was needed for the

brain study discussed in Chapter 2). These adaptations included volumetric loading of respirometry samples, the development of automated calculation sheets for high-throughput analysis of respirometry results, and the development of quality control parameters which can automatically assess respirometry data without having to manually assess the data for outliers. Together, these novel techniques allowed for the successful processing of the largest respirometry sample cohort ever assembled which not only provided novel data, but allowed for the assembly of mitochondrial function data which could not be obtained using the current standard methodologies to assess mitochondrial function in high-throughput (colorimetry).

In Chapter 4 of this thesis, we shift away from research specimens and begin to address the challenges associated with performing respirometry in human subjects. While we know that mitochondrial function changes with factors like age and BMI, the current methodologies to measure mitochondrial respiration clinically require invasive sample collection methods like muscle biopsies. This ultimately results in mitochondrial function not being measured clinically. We identified that the cellular content of saliva is a tissue type which can be collected non-invasively and (using the RIFS assay) would not be difficult to process for the purpose of respirometry. We found that by separating the salivary leukocytes from the buccal epithelial cells, we obtain a sample type which can reproducibly measure mitochondrial function in single individuals. Respirometry in salivary leukocytes is an assay which makes the assessment of mitochondrial function more accessible than ever before. In the future we intend to assess changes in mitochondrial respiratory capacity as they relate to biological factors like sex, age, and BMI, but also chronological factors like time of day, day and night cycles, and before and after events like exercise or eating.

While respirometry was previously reserved for small scale assessments, especially in humans, in this thesis we have developed methodologies which make the assessment of mitochondrial function via respirometry more accessible and approachable than ever before.

Whether it is in the form of large-scale data sets as discussed in Chapters 2 and 3 or with clinical assessment in mind as discussed in Chapter 4, these techniques address the hurdles which have prevented widespread adoption of respirometry. In the future we hope to expand upon these technologies, assessing tissue heterogeneity in even higher resolution and understanding the human factors which alter mitochondrial activity in clinical cohorts. We believe that these efforts will eliminate the many research and clinical hurdles which exist to make the assessment of mitochondrial function a universal parameter.

BIBLIOGRAPHY

Acin-Perez, Rebeca, Ilan Y Benador, Anton Petcherski, Michaela Veliova, Gloria A Benavides, Sylviane Lagarrigue, Arianne Caudal, et al. 2020. “A Novel Approach to Measure Mitochondrial Respiration in Frozen Biological Samples.” *The EMBO Journal* 39 (13): e104073. https://doi.org/10.15252/embj.2019104073.

Acin-Perez, Rebeca, Cristiane Benincá, Byourak Shabane, Orian S. Shirihai, and Linsey Stiles. 2021. “Utilization of Human Samples for Assessment of Mitochondrial Bioenergetics: Gold Standards, Limitations, and Future Perspectives.” *Life* 11 (9): 949. https://doi.org/10.3390/life11090949.

Alkemade, Anneke, Pierre-Louis Bazin, Rawien Balesar, Kerrin Pine, Evgeniya Kirilina, Harald E. Möller, Robert Trampel, et al. 2022. “A Unified 3D Map of Microscopic Architecture and MRI of the Human Brain.” *Science Advances* 8 (17): eabj7892. https://doi.org/10.1126/sciadv.abj7892.

Amunts, Katrin, Claude Lepage, Louis Borgeat, Hartmut Mohlberg, Timo Dickscheid, Marc-Étienne Rousseau, Sebastian Bludau, et al. 2013. “BigBrain: An Ultrahigh-Resolution 3D Human Brain Model.” *Science* 340 (6139): 1472–75. https://doi.org/10.1126/science.1235381.

Bakken, Trygve E., Nikolas L. Jorstad, Qiwen Hu, Blue B. Lake, Wei Tian, Brian E. Kalmbach, Megan Crow, et al. 2021. “Comparative Cellular Analysis of Motor Cortex in Human, Marmoset and Mouse.” *Nature* 598 (7879): 111–19. https://doi.org/10.1038/s41586-021-03465-8.

Becht, Etienne, Leland McInnes, John Healy, Charles-Antoine Dutertre, Immanuel W. H. Kwok, Lai Guan Ng, Florent Ginhoux, and Evan W. Newell. 2019. “Dimensionality Reduction for Visualizing Single-Cell Data Using UMAP.” *Nature Biotechnology* 37 (1): 38–44. https://doi.org/10.1038/nbt.4314.

Billingham, Leah K., Joshua S. Stoolman, Karthik Vasan, Arianne E. Rodriguez, Taylor A. Poor, Marten Szibor, Howard T. Jacobs, et al. 2022. “Mitochondrial Electron Transport Chain Is Necessary for NLRP3 Inflammasome Activation.” *Nature Immunology* 23 (5): 692–704. https://doi.org/10.1038/s41590-022-01185-3.

Blazey, Tyler, Abraham Z Snyder, Yi Su, Manu S Goyal, John J Lee, Andrei G Vlassenko, Ana Maria Arbeláez, and Marcus E Raichle. 2019. “Quantitative Positron Emission Tomography Reveals Regional Differences in Aerobic Glycolysis within the Human Brain.” *Journal of Cerebral Blood Flow & Metabolism* 39 (10): 2096–2102. https://doi.org/10.1177/0271678X18767005.

Bolam, J. Paul, and Eleftheria K. Pissadaki. 2012. “Living on the Edge with Too Many Mouths to Feed: Why Dopamine Neurons Die.” *Movement Disorders* 27 (12): 1478–83. https://doi.org/10.1002/mds.25135.

Boldrini, Maura, Hanga Galfalvy, Andrew J. Dwork, Gorazd B. Rosoklija, Iskra Trencevska-Ivanovska, Goran Pavlovski, René Hen, Victoria Arango, and J. John Mann. 2019. “Resilience Is Associated With Larger Dentate Gyrus, While Suicide Decedents With

Major Depressive Disorder Have Fewer Granule Neurons." *Biological Psychiatry*, Longitudinal Perspectives on Stress and Depression, 85 (10): 850–62. https://doi.org/10.1016/j.biopsych.2018.12.022.

Borsche, Max, Sandro L. Pereira, Christine Klein, and Anne Grünewald. 2021. "Mitochondria and Parkinson's Disease: Clinical, Molecular, and Translational Aspects." *Journal of Parkinson's Disease* 11 (1): 45–60. https://doi.org/10.3233/JPD-201981.

Bose, Anindita, and M. Flint Beal. 2016. "Mitochondrial Dysfunction in Parkinson's Disease." *Journal of Neurochemistry* 139 (S1): 216–31. https://doi.org/10.1111/jnc.13731.

Castrillon, Gabriel, Samira Epp, Antonia Bose, Laura Fraticelli, André Hechler, Roman Belenya, Andreas Ranft, et al. 2023. "An Energy Costly Architecture of Neuromodulators for Human Brain Evolution and Cognition." *Science Advances* 9 (50): eadi7632. https://doi.org/10.1126/sciadv.adi7632.

Catani, Marco, Flavio Dell'Acqua, Francesco Vergani, Farah Malik, Harry Hodge, Prasun Roy, Romain Valabregue, and Michel Thiebaut de Schotten. 2012. "Short Frontal Lobe Connections of the Human Brain." *Cortex*, Frontal lobes, 48 (2): 273–91. https://doi.org/10.1016/j.cortex.2011.12.001.

Cheng, Weiqin, Yuting Zhang, and Ling He. 2022. "MRI Features of Stroke-Like Episodes in Mitochondrial Encephalomyopathy With Lactic Acidosis and Stroke-Like Episodes." *Frontiers in Neurology* 13 (February). https://doi.org/10.3389/fneur.2022.843386.

Croxson, Paula L, Stephanie J Forkel, Leonardo Cerliani, and Michel Thiebaut de Schotten. 2018. "Structural Variability Across the Primate Brain: A Cross-Species Comparison." *Cerebral Cortex* 28 (11): 3829–41. https://doi.org/10.1093/cercor/bhx244.

Cui, Zaixu, Jennifer Stiso, Graham L Baum, Jason Z Kim, David R Roalf, Richard F Betzel, Shi Gu, et al. 2020. "Optimization of Energy State Transition Trajectory Supports the Development of Executive Function during Youth." Edited by Thomas Yeo and Timothy E Behrens. *eLife* 9 (March):e53060. https://doi.org/10.7554/eLife.53060.

Darwin, Charles. 1912. *The Origin of Species by Means of Natural Selection, or, The Preservation of Favored Races in the Struggle for Life v. 1-2*. D. Appleton and Company.

Deo, Priya Nimish, and Revati Deshmukh. 2019. "Oral Microbiome: Unveiling the Fundamentals." *Journal of Oral and Maxillofacial Pathology : JOMFP* 23 (1): 122–28. https://doi.org/10.4103/jomfp.JOMFP_304_18.

Divakaruni, Ajit S., and Martin Jastroch. 2022. "A Practical Guide for the Analysis, Standardization and Interpretation of Oxygen Consumption Measurements." *Nature Metabolism* 4 (8): 978–94. https://doi.org/10.1038/s42255-022-00619-4.

Donovan, John, and Patricia Brown. 2006. "Euthanasia." *Current Protocols in Immunology* 73 (1): 1.8.1-1.8.4. https://doi.org/10.1002/0471142735.im0108s73.

Düking, Tim, Lena Spieth, Stefan A. Berghoff, Lars Piepkorn, Annika M. Schmidke, Miso Mitkovski, Nirmal Kannaiyan, et al. 2022. "Ketogenic Diet Uncovers Differential

Metabolic Plasticity of Brain Cells." *Science Advances* 8 (37): eabo7639. https://doi.org/10.1126/sciadv.abo7639.

Dunn, Anne K. 2023. "Alternative Oxidase in Bacteria." *Biochimica et Biophysica Acta (BBA) - Bioenergetics* 1864 (1): 148929. https://doi.org/10.1016/j.bbabio.2022.148929.

Essen, David C. Van, and Donna L. Dierker. 2007. "Surface-Based and Probabilistic Atlases of Primate Cerebral Cortex." *Neuron* 56 (2): 209–25. https://doi.org/10.1016/j.neuron.2007.10.015.

Fecher, Caroline, Laura Trovò, Stephan A. Müller, Nicolas Snaidero, Jennifer Wettmarshausen, Sylvia Heink, Oskar Ortiz, et al. 2019. "Cell-Type-Specific Profiling of Brain Mitochondria Reveals Functional and Molecular Diversity." *Nature Neuroscience* 22 (10): 1731–42. https://doi.org/10.1038/s41593-019-0479-z.

Fernández-Bertólez, Natalia, Amaya Azqueta, Eduardo Pásaro, Blanca Laffon, and Vanessa Valdiglesias. 2021. "Salivary Leucocytes as Suitable Biomatrix for the Comet Assay in Human Biomonitoring Studies." *Archives of Toxicology* 95 (6): 2179–87. https://doi.org/10.1007/s00204-021-03038-8.

Finnegan, Jennifer M., Karin Pihel, Paula S. Cahill, Lan Huang, Susan E. Zerby, Andrew G. Ewing, Robert T. Kennedy, and R. Mark Wightman. 1996. "Vesicular Quantal Size Measured by Amperometry at Chromaffin, Mast, Pheochromocytoma, and Pancreatic β-Cells." *Journal of Neurochemistry* 66 (5): 1914–23. https://doi.org/10.1046/j.1471-4159.1996.66051914.x.

Fleming, Stephen J., Mark D. Chaffin, Alessandro Arduini, Amer-Denis Akkad, Eric Banks, John C. Marioni, Anthony A. Philippakis, Patrick T. Ellinor, and Mehrtash Babadi. 2023. "Unsupervised Removal of Systematic Background Noise from Droplet-Based Single-Cell Experiments Using CellBender." *Nature Methods* 20 (9): 1323–35. https://doi.org/10.1038/s41592-023-01943-7.

Forkel, Stephanie J., Michel Thiebaut de Schotten, Flavio Dell'Acqua, Lalit Kalra, Declan G. M. Murphy, Steven C. R. Williams, and Marco Catani. 2014. "Anatomical Predictors of Aphasia Recovery: A Tractography Study of Bilateral Perisylvian Language Networks." *Brain* 137 (7): 2027–39. https://doi.org/10.1093/brain/awu113.

Fox, Emily. n.d. "Micrograph Human Cheek Epithelial Cells Methylene Blue 1000X P000018." OER Commons. Accessed July 11, 2024. https://oercommons.org/courseware/lesson/89980/overview.

Frederiksen, A L, P H Andersen, K O Kyvik, T D Jeppesen, J Vissing, and M Schwartz. 2006. "Tissue Specific Distribution of the 3243A→G mtDNA Mutation." *Journal of Medical Genetics* 43 (8): 671–77. https://doi.org/10.1136/jmg.2005.039339.

Friedrich, Patrick, Stephanie J. Forkel, Céline Amiez, Joshua H. Balsters, Olivier Coulon, Lingzhong Fan, Alexandros Goulas, et al. 2021. "Imaging Evolution of the Primate Brain: The next Frontier?" *NeuroImage* 228 (March):117685. https://doi.org/10.1016/j.neuroimage.2020.117685.

Fuchs, Hanna, Arleta Malecka, Adrianna Budzinska, Wieslawa Jarmuszkiewicz, Liliana Ciszewska, Aleksandra M. Staszak, Joanna Kijowska-Oberc, and Ewelina Ratajczak. 2023. “High-Throughput Method for Oxygen Consumption Rate Measurement (OCR) in Plant Mitochondria.” *BMC Plant Biology* 23 (1): 496. https://doi.org/10.1186/s12870-023-04516-0.

Gebara, Elias, Olivia Zanoletti, Sriparna Ghosal, Jocelyn Grosse, Bernard L. Schneider, Graham Knott, Simone Astori, and Carmen Sandi. 2021. “Mitofusin-2 in the Nucleus Accumbens Regulates Anxiety and Depression-like Behaviors Through Mitochondrial and Neuronal Actions.” *Biological Psychiatry*, Glutamate-Dopamine Interactions in Antidepressant Efficacy, 89 (11): 1033–44. https://doi.org/10.1016/j.biopsych.2020.12.003.

Gordon, Evan M., Timothy O. Laumann, Adrian W. Gilmore, Dillan J. Newbold, Deanna J. Greene, Jeffrey J. Berg, Mario Ortega, et al. 2017. “Precision Functional Mapping of Individual Human Brains.” *Neuron* 95 (4): 791-807.e7. https://doi.org/10.1016/j.neuron.2017.07.011.

Griessl, Tim, Silke Zechel-Gran, Stefan Olejniczak, Markus Weigel, Torsten Hain, and Eugen Domann. 2021. “High-Resolution Taxonomic Examination of the Oral Microbiome after Oil Pulling with Standardized Sunflower Seed Oil and Healthy Participants: A Pilot Study.” *Clinical Oral Investigations* 25 (5): 2689–2703. https://doi.org/10.1007/s00784-020-03582-0.

Grillner, Sten, and Brita Robertson. 2016. “The Basal Ganglia Over 500 Million Years.” *Current Biology* 26 (20): R1088–1100. https://doi.org/10.1016/j.cub.2016.06.041.

Haber, S N. 1986. “Neurotransmitters in the Human and Nonhuman Primate Basal Ganglia.” *Human Neurobiology* 5 (3): 159–68.

Hara, Yuko, Frank Yuk, Rishi Puri, William G. M. Janssen, Peter R. Rapp, and John H. Morrison. 2014. “Presynaptic Mitochondrial Morphology in Monkey Prefrontal Cortex Correlates with Working Memory and Is Improved with Estrogen Treatment.” *Proceedings of the National Academy of Sciences* 111 (1): 486–91. https://doi.org/10.1073/pnas.1311310110.

He, Xiaosong, Lorenzo Caciagli, Linden Parkes, Jennifer Stiso, Teresa M. Karrer, Jason Z. Kim, Zhixin Lu, et al. 2022. “Uncovering the Biological Basis of Control Energy: Structural and Metabolic Correlates of Energy Inefficiency in Temporal Lobe Epilepsy.” *Science Advances* 8 (45): eabn2293. https://doi.org/10.1126/sciadv.abn2293.

Hill, Bradford G., Sruti Shiva, Scott Ballinger, Jianhua Zhang, and Victor M. Darley-Usmar. 2019. “Bioenergetics and Translational Metabolism: Implications for Genetics, Physiology and Precision Medicine.” *Biological Chemistry* 401 (1): 3–29. https://doi.org/10.1515/hsz-2019-0268.

Hill, Jason, Terrie Inder, Jeffrey Neil, Donna Dierker, John Harwell, and David Van Essen. 2010. “Similar Patterns of Cortical Expansion during Human Development and Evolution.” *Proceedings of the National Academy of Sciences* 107 (29): 13135–40. https://doi.org/10.1073/pnas.1001229107.

Hocking, R. R. 1976. “A Biometrics Invited Paper. The Analysis and Selection of Variables in Linear Regression.” *Biometrics* 32 (1): 1–49. https://doi.org/10.2307/2529336.

Hollis, Fiona, Michael A. van der Kooij, Olivia Zanoletti, Laura Lozano, Carles Cantó, and Carmen Sandi. 2015. “Mitochondrial Function in the Brain Links Anxiety with Social Subordination.” *Proceedings of the National Academy of Sciences* 112 (50): 15486–91. https://doi.org/10.1073/pnas.1512653112.

Howard, Amy F. D., Istvan N. Huszar, Adele Smart, Michiel Cottaar, Greg Daubney, Taylor Hanayik, Alexandre A. Khrapitchev, et al. 2023. “An Open Resource Combining Multi-Contrast MRI and Microscopy in the Macaque Brain.” *Nature Communications* 14 (1): 4320. https://doi.org/10.1038/s41467-023-39916-1.

Jiang, Wei-Wen, Brett Masayesva, Marianna Zahurak, Andre Lopes Carvalho, Eli Rosenbaum, Elizabeth Mambo, Shaoyu Zhou, et al. 2005. “Increased Mitochondrial DNA Content in Saliva Associated with Head and Neck Cancer.” *Clinical Cancer Research* 11 (7): 2486–91. https://doi.org/10.1158/1078-0432.CCR-04-2147.

Joshi, Amit U., Paras S. Minhas, Shane A. Liddelow, Bereketeab Haileselassie, Katrin I. Andreasson, Gerald W. Dorn, and Daria Mochly-Rosen. 2019. “Fragmented Mitochondria Released from Microglia Trigger A1 Astrocytic Response and Propagate Inflammatory Neurodegeneration.” *Nature Neuroscience* 22 (10): 1635–48. https://doi.org/10.1038/s41593-019-0486-0.

Kelly, T. M., and J. J. Mann. 1996. “Validity of DSM-III-R Diagnosis by Psychological Autopsy: A Comparison with Clinician Ante-Mortem Diagnosis.” *Acta Psychiatrica Scandinavica* 94 (5): 337–43. https://doi.org/10.1111/j.1600-0447.1996.tb09869.x.

Klein, Hans-Ulrich, Caroline Trumpff, Hyun-Sik Yang, Annie J. Lee, Martin Picard, David A. Bennett, and Philip L. De Jager. 2021. “Characterization of Mitochondrial DNA Quantity and Quality in the Human Aged and Alzheimer’s Disease Brain.” *Molecular Neurodegeneration* 16 (1): 75. https://doi.org/10.1186/s13024-021-00495-8.

Korsunsky, Ilya, Nghia Millard, Jean Fan, Kamil Slowikowski, Fan Zhang, Kevin Wei, Yuriy Baglaenko, Michael Brenner, Po-ru Loh, and Soumya Raychaudhuri. 2019. “Fast, Sensitive and Accurate Integration of Single-Cell Data with Harmony.” *Nature Methods* 16 (12): 1289–96. https://doi.org/10.1038/s41592-019-0619-0.

Kwon, Seok-Kyu, Richard Sando Iii, Tommy L. Lewis, Yusuke Hirabayashi, Anton Maximov, and Franck Polleux. 2016. “LKB1 Regulates Mitochondria-Dependent Presynaptic Calcium Clearance and Neurotransmitter Release Properties at Excitatory Synapses along Cortical Axons.” *PLOS Biology* 14 (7): e1002516. https://doi.org/10.1371/journal.pbio.1002516.

Liesa, Marc, Manuel Palacín, and Antonio Zorzano. 2009. “Mitochondrial Dynamics in Mammalian Health and Disease.” *Physiological Reviews* 89 (3): 799–845. https://doi.org/10.1152/physrev.00030.2008.

Lin, Miao-miao, Na Liu, Zheng-hong Qin, and Yan Wang. 2022. “Mitochondrial-Derived Damage-Associated Molecular Patterns Amplify Neuroinflammation in

Neurodegenerative Diseases." *Acta Pharmacologica Sinica* 43 (10): 2439–47. https://doi.org/10.1038/s41401-022-00879-6.

Lopes, Carla, I. Luísa Ferreira, Carina Maranga, Margarida Beatriz, Sandra I. Mota, José Sereno, João Castelhano, et al. 2022. "Mitochondrial and Redox Modifications in Early Stages of Huntington's Disease." *Redox Biology* 56 (October):102424. https://doi.org/10.1016/j.redox.2022.102424.

Mai, Juergen K., Milan Majtanik, and George Paxinos. 2015. *Atlas of the Human Brain*. Academic Press.

Margulies, Daniel S., Satrajit S. Ghosh, Alexandros Goulas, Marcel Falkiewicz, Julia M. Huntenburg, Georg Langs, Gleb Bezgin, et al. 2016. "Situating the Default-Mode Network along a Principal Gradient of Macroscale Cortical Organization." *Proceedings of the National Academy of Sciences* 113 (44): 12574–79. https://doi.org/10.1073/pnas.1608282113.

Monzel, Anna S., José Antonio Enríquez, and Martin Picard. 2023. "Multifaceted Mitochondria: Moving Mitochondrial Science beyond Function and Dysfunction." *Nature Metabolism* 5 (4): 546–62. https://doi.org/10.1038/s42255-023-00783-1.

Moore, H. L., A. P. Blain, D. M. Turnbull, and G. S. Gorman. 2020. "Systematic Review of Cognitive Deficits in Adult Mitochondrial Disease." *European Journal of Neurology* 27 (1): 3–17. https://doi.org/10.1111/ene.14068.

Mosharov, Eugene V., Ayelet M. Rosenberg, Anna S. Monzel, Corey A. Osto, Linsey Stiles, Gorazd B. Rosoklija, Andrew J. Dwork, et al. 2024. "A Human Brain Map of Mitochondrial Respiratory Capacity and Diversity." bioRxiv. https://doi.org/10.1101/2024.03.05.583623.

Osto, Corey, Ilan Y Benador, Jennifer Ngo, Marc Liesa, Linsey Stiles, Rebeca Acin-Perez, and Orian S. Shirihai. 2020. "Measuring Mitochondrial Respiration in Previously Frozen Biological Samples." Current Protocols in Cell Biology.

Padamsey, Zahid, and Nathalie L. Rochefort. 2023. "Paying the Brain's Energy Bill." *Current Opinion in Neurobiology* 78 (February):102668. https://doi.org/10.1016/j.conb.2022.102668.

Pandya, Deepak, Michael Petrides, and Patsy Benny Cipolloni. 2015. *Cerebral Cortex: Architecture, Connections, and the Dual Origin Concept*. Oxford University Press.

Pekkurnaz, Gulcin, and Xinnan Wang. 2022. "Mitochondrial Heterogeneity and Homeostasis through the Lens of a Neuron." *Nature Metabolism* 4 (7): 802–12. https://doi.org/10.1038/s42255-022-00594-w.

Picard, Martin, Aric A. Prather, Eli Puterman, Alexanne Cuillerier, Michael Coccia, Kirstin Aschbacher, Yan Burelle, and Elissa S. Epel. 2018. "A Mitochondrial Health Index Sensitive to Mood and Caregiving Stress." *Biological Psychiatry* 84 (1): 9–17. https://doi.org/10.1016/j.biopsych.2018.01.012.

Picard, Martin, and Orian S. Shirihai. 2022. “Mitochondrial Signal Transduction.” *Cell Metabolism* 34 (11): 1620–53. https://doi.org/10.1016/j.cmet.2022.10.008.

Pinotsis, Dimitris A., Gene Fridman, and Earl K. Miller. 2023. “Cytoelectric Coupling: Electric Fields Sculpt Neural Activity and ‘Tune’ the Brain’s Infrastructure.” *Progress in Neurobiology* 226 (July):102465. https://doi.org/10.1016/j.pneurobio.2023.102465.

Pontzer, Herman, Mary H. Brown, David A. Raichlen, Holly Dunsworth, Brian Hare, Kara Walker, Amy Luke, et al. 2016. “Metabolic Acceleration and the Evolution of Human Brain Size and Life History.” *Nature* 533 (7603): 390–92. https://doi.org/10.1038/nature17654.

Poznyak, Anastasia V., Ekaterina A. Ivanova, Igor A. Sobenin, Shaw-Fang Yet, and Alexander N. Orekhov. 2020. “The Role of Mitochondria in Cardiovascular Diseases.” *Biology* 9 (6): 137. https://doi.org/10.3390/biology9060137.

Ramachandran, S., and D. Gottlieb. 1961. “Mode of Action of Antibiotics II. Specificity of Action of Antimycin a and Ascosin.” *Biochimica et Biophysica Acta* 53 (2): 396–402. https://doi.org/10.1016/0006-3002(61)90451-6.

Rath, Sneha, Rohit Sharma, Rahul Gupta, Tslil Ast, Connie Chan, Timothy J Durham, Russell P Goodman, et al. 2021. “MitoCarta3.0: An Updated Mitochondrial Proteome Now with Sub-Organelle Localization and Pathway Annotations.” *Nucleic Acids Research* 49 (D1): D1541–47. https://doi.org/10.1093/nar/gkaa1011.

Rogers, George W., Martin D. Brand, Susanna Petrosyan, Deepthi Ashok, Alvaro A. Elorza, David A. Ferrick, and Anne N. Murphy. 2011. “High Throughput Microplate Respiratory Measurements Using Minimal Quantities Of Isolated Mitochondria.” Edited by Alicia J. Kowaltowski. *PLoS ONE* 6 (7): e21746. https://doi.org/10.1371/journal.pone.0021746.

Rosenberg, Ayelet M., Manish Saggar, Anna S. Monzel, Jack Devine, Peter Rogu, Aaron Limoges, Alex Junker, et al. 2023. “Brain Mitochondrial Diversity and Network Organization Predict Anxiety-like Behavior in Male Mice.” *Nature Communications* 14 (1): 4726. https://doi.org/10.1038/s41467-023-39941-0.

Rudney, J. D., and R. Chen. 2006. “The Vital Status of Human Buccal Epithelial Cells and the Bacteria Associated with Them.” *Archives of Oral Biology* 51 (4): 291–98. https://doi.org/10.1016/j.archoralbio.2005.09.003.

Sharpley, Mark S., Christine Marciniak, Kristin Eckel-Mahan, Meagan McManus, Marco Crimi, Katrina Waymire, Chun Shi Lin, et al. 2012. “Heteroplasmy of Mouse mtDNA Is Genetically Unstable and Results in Altered Behavior and Cognition.” *Cell* 151 (2): 333–43. https://doi.org/10.1016/j.cell.2012.09.004.

Slyper, Michal, Caroline B. M. Porter, Orr Ashenberg, Julia Waldman, Eugene Drokhlyansky, Isaac Wakiro, Christopher Smillie, et al. 2020. “A Single-Cell and Single-Nucleus RNA-Seq Toolbox for Fresh and Frozen Human Tumors.” *Nature Medicine* 26 (5): 792–802. https://doi.org/10.1038/s41591-020-0844-1.

Smith, Stephen M., Peter T. Fox, Karla L. Miller, David C. Glahn, P. Mickle Fox, Clare E. Mackay, Nicola Filippini, et al. 2009. “Correspondence of the Brain’s Functional

Architecture during Activation and Rest." *Proceedings of the National Academy of Sciences* 106 (31): 13040–45. https://doi.org/10.1073/pnas.0905267106.

Song, Mengyuan, Hao Bai, Ping Zhang, Xuedong Zhou, and Binwu Ying. 2023. "Promising Applications of Human-Derived Saliva Biomarker Testing in Clinical Diagnostics." *International Journal of Oral Science* 15 (1): 1–17. https://doi.org/10.1038/s41368-022-00209-w.

Sousa, Alexandra A. de, Amélie Beaudet, Tanya Calvey, Ameline Bardo, Julien Benoit, Christine J. Charvet, Colette Dehay, et al. 2023. "From Fossils to Mind." *Communications Biology* 6 (1): 1–21. https://doi.org/10.1038/s42003-023-04803-4.

Strasser, Alina, Gediminas Luksys, Lijing Xin, Mathias Pessiglione, Rolf Gruetter, and Carmen Sandi. 2020. "Glutamine-to-Glutamate Ratio in the Nucleus Accumbens Predicts Effort-Based Motivated Performance in Humans." *Neuropsychopharmacology* 45 (12): 2048–57. https://doi.org/10.1038/s41386-020-0760-6.

Styr, Boaz, Nir Gonen, Daniel Zarhin, Antonella Ruggiero, Refaela Atsmon, Neta Gazit, Gabriella Braun, et al. 2019. "Mitochondrial Regulation of the Hippocampal Firing Rate Set Point and Seizure Susceptibility." *Neuron* 102 (5): 1009-1024.e8. https://doi.org/10.1016/j.neuron.2019.03.045.

Tavor, I., O. Parker Jones, R. B. Mars, S. M. Smith, T. E. Behrens, and S. Jbabdi. 2016. "Task-Free MRI Predicts Individual Differences in Brain Activity during Task Performance." *Science* 352 (6282): 216–20. https://doi.org/10.1126/science.aad8127.

Theda, Christiane, Seo Hye Hwang, Anna Czajko, Yuk Jing Loke, Pamela Leong, and Jeffrey M. Craig. 2018. "Quantitation of the Cellular Content of Saliva and Buccal Swab Samples." *Scientific Reports* 8 (1): 6944. https://doi.org/10.1038/s41598-018-25311-0.

Tomasi, Dardo, Gene-Jack Wang, and Nora D. Volkow. 2013. "Energetic Cost of Brain Functional Connectivity." *Proceedings of the National Academy of Sciences* 110 (33): 13642–47. https://doi.org/10.1073/pnas.1303346110.

Trumpff, Caroline, Anna L. Marsland, Carla Basualto-Alarcón, James L. Martin, Judith E. Carroll, Gabriel Sturm, Amy E. Vincent, et al. 2019. "Acute Psychological Stress Increases Serum Circulating Cell-Free Mitochondrial DNA." *Psychoneuroendocrinology* 106 (August):268–76. https://doi.org/10.1016/j.psyneuen.2019.03.026.

Trumpff, Caroline, Shannon Rausser, Rachel Haahr, Kalpita R. Karan, Gilles Gouspillou, Eli Puterman, Clemens Kirschbaum, and Martin Picard. 2022. "Dynamic Behavior of Cell-Free Mitochondrial DNA in Human Saliva." *Psychoneuroendocrinology* 143 (September):105852. https://doi.org/10.1016/j.psyneuen.2022.105852.

Tsuchida, Ami, Alexandre Laurent, Fabrice Crivello, Laurent Petit, Marc Joliot, Antonietta Pepe, Naka Beguedou, et al. 2021. "The MRi-Share Database: Brain Imaging in a Cross-Sectional Cohort of 1870 University Students." *Brain Structure and Function* 226 (7): 2057–85. https://doi.org/10.1007/s00429-021-02334-4.

Tyrrell, Daniel J., Manish S. Bharadwaj, Matthew J. Jorgensen, Thomas C. Register, and Anthony J.A. Molina. 2016. "Blood Cell Respirometry Is Associated with Skeletal and

Cardiac Muscle Bioenergetics: Implications for a Minimally Invasive Biomarker of Mitochondrial Health." *Redox Biology* 10 (September):65–77. https://doi.org/10.1016/j.redox.2016.09.009.

Umarova, Roza M., Lena Beume, Marco Reisert, Christoph P. Kaller, Stefan Klöppel, Irina Mader, Volkmar Glauche, Valerij G. Kiselev, Marco Catani, and Cornelius Weiller. 2017. "Distinct White Matter Alterations Following Severe Stroke." *Neurology* 88 (16): 1546–55. https://doi.org/10.1212/WNL.0000000000003843.

Valdiglesias, Vanessa, Natalia Fernández-Bertólez, Carlota Lema-Arranz, Raquel Rodríguez-Fernández, Eduardo Pásaro, Ana Teresa Reis, João Paulo Teixeira, Carla Costa, and Blanca Laffon. 2021. "Salivary Leucocytes as In Vitro Model to Evaluate Nanoparticle-Induced DNA Damage." *Nanomaterials* 11 (8): 1930. https://doi.org/10.3390/nano11081930.

Van Essen, David C., Stephen M. Smith, Deanna M. Barch, Timothy E. J. Behrens, Essa Yacoub, and Kamil Ugurbil. 2013. "The WU-Minn Human Connectome Project: An Overview." *NeuroImage*, Mapping the Connectome, 80 (October):62–79. https://doi.org/10.1016/j.neuroimage.2013.05.041.

Vekaria, Hemendra J., Olivia J. Kalimon, Paresh Prajapati, Gopal V. Velmurugan, and Patrick G. Sullivan. 2024. "An Efficient and High-Throughput Method for the Evaluation of Mitochondrial Dysfunction in Frozen Brain Samples after Traumatic Brain Injury." *Frontiers in Molecular Biosciences* 11 (June). https://doi.org/10.3389/fmolb.2024.1378536.

Vidović, Anđelko, Danica Vidović Juras, Vanja Vučićević Boras, Josip Lukač, Mirjana Grubišić-Ilić, Davor Rak, and Ante Sabioncello. 2012. "Determination of Leucocyte Subsets in Human Saliva by Flow Cytometry." *Archives of Oral Biology* 57 (5): 577–83. https://doi.org/10.1016/j.archoralbio.2011.10.015.

Wallace, D. C. 2011. "Bioenergetic Origins of Complexity and Disease." *Cold Spring Harbor Symposia on Quantitative Biology* 76:1–16. https://doi.org/10.1101/sqb.2011.76.010462.

Yamamoto, Masazumi, Kiyomi Saeki, and Kozo Utsumi. 1991. "Isolation of Human Salivary Polymorphonuclear Leukocytes and Their Stimulation-Coupled Responses." *Archives of Biochemistry and Biophysics* 289 (1): 76–82. https://doi.org/10.1016/0003-9861(91)90444-N.

Yépez, Vicente A., Laura S. Kremer, Arcangela Iuso, Mirjana Gusic, Robert Kopajtich, Eliška Koňaříková, Agnieszka Nadel, Leonhard Wachutka, Holger Prokisch, and Julien Gagneur. 2018. "OCR-Stats: Robust Estimation and Statistical Testing of Mitochondrial Respiration Activities Using Seahorse XF Analyzer." *PLOS ONE* 13 (7): e0199938. https://doi.org/10.1371/journal.pone.0199938.

Yu, Yuguo, Adil Akif, Peter Herman, Miao Cao, Douglas L Rothman, Richard E Carson, Divyansh Agarwal, Alan C Evans, and Fahmeed Hyder. 2023. "A 3D Atlas of Functional Human Brain Energetic Connectome Based on Neuropil Distribution." *Cerebral Cortex* 33 (7): 3996–4012. https://doi.org/10.1093/cercor/bhac322.

Zhang, Hui, Torben Schneider, Claudia A. Wheeler-Kingshott, and Daniel C. Alexander. 2012. "NODDI: Practical *in Vivo* Neurite Orientation Dispersion and Density Imaging of the Human Brain." *NeuroImage* 61 (4): 1000–1016. https://doi.org/10.1016/j.neuroimage.2012.03.072.